TOWARDS THE VALIDATION OF THERMOACOUSTIC MODELLING IN AEROSPACE STRUCTURES

By

Christopher Sebastian

A THESIS

Submitted to
the University of Liverpool
in partial fulfillment of the requirements
for the degree of

Doctor of Philosophy

2015

ABSTRACT

TOWARDS THE VALIDATION OF THERMOACOUSTIC MODELLING IN AEROSPACE STRUCTURES

By

Christopher Sebastian

The research presented in this thesis has been performed over the course of three years under funding from the European Office of the United States Air Force (EAORD) as a part of a long-term project to collect high quality data for the validation of computational mechanics models of thermoacoustic loading. The focus is on the adaptation of stereoscopic (3D) Digital Image Correlation for use in a combined thermal and high temperature measurements. To that end, a background is provided which highlights the current state of the art in high temperature, vibration experiments and data acquisition.

A system is described in which a pulsed laser of duration 4 nanoseconds is used to capture high-quality displacement and strain data from vibrating components (PL-DIC). Based on this a novel method of capturing data from a component subjected to random excitation was developed. A laser vibrometer was used along with a custom LabVIEW program to trigger the pulsed laser relative to points of maximum velocity in the components vibration cycle.

A dynamic calibration procedure was performed of both a high speed DIC system and the Pulsed-Laser DIC system to assess and compare the measurement uncertainty from the respective systems. It is crucial to know the uncertainty in experimental data when using it for the validation of computational models.

A new way to validate computational models of vibration behavior using full-field DIC data and image decomposition is described. This is a phasic approach in which data from the entire cycle of vibration is used. The validation assessment is performed using the expanded uncertainty calculated and a concordance correlation coefficient. An

example is provided using an aerospace component to validate four different simulation conditions of a modal frequency response model.

An apparatus was designed and built which uses a 10 kW array of quartz lamps to reproduce some aspects of the heating provided by the Air Force test chambers. Experiments were performed in collaboration with the University of Illinois using induction heating and a small Hastelloy plate. A thermal buckling phenomena was observed using the PL-DIC system, the first full-field results of such.

To Kimberley and My Parents

ACKNOWLEDGMENTS

I am very grateful to my supervisor, Professor Eann Patterson for all of his guidance and feedback during my research. I think it is uncommon to have a supervisor who dedicates as much time and effort to his students as Eann does. He now also holds the distinction of 'person that I have worked for the longest' in my career (going on 5+ years!), which I think speaks to his leadership abilities.

I would also like to thank Professor John Lambros at the University of Illinois for the collaboration with this project; the countless Skype calls and email conversations were very helpful.

I must also gratefully acknowledge the help and support of those at the University that have helped me throughout: Derek Neary for his electronics expertise and general enthusiasm, Steve Pennington who I could always count on to make me something last minute in the machine shop, and Jiji Mathew for his CNC manufacturing skills. I would also like to thank Dr. Rob Birch for helping me to navigate the U.K. Health and Safety minefield.

I am thankful to the U.S. Air Force Office of Scientific Research for providing the funding to make this all possible. Particularly Dr. Ravi Chona at the Structural Sciences Center and Ty Pollak and Matt Snyder at the European office (EOARD).

Effort sponsored by the Air Force Office of Scientific Research, Air Force Material Command, USAF, under grant number FA8655-11-1-3083. The U.S. Government is authorized to reproduce and distribute reprints for Governmental purpose notwithstanding any copyright notation thereon.

TABLE OF CONTENTS

LIST OF TABLES

LIST OF FIGURES

Chapter 1

Introduction

1.1 Motivation

One of the most common failure modes in aircraft structures is material and structural fatigue. Despite a considerable improvement over the last several decades, the reliable prediction of fatigue life continues to be a challenge, especially for complex structures operating in extreme conditions such as those encountered during hypersonic flight. This combined high-temperature and vibration environment is not well understood. There is a considerable cost and complexity associated with performing experiments under these conditions, and so simulation is heavily relied upon. Better simulations are needed to meet strict weight and performance requirements, and to make them better they need to be validated with high-quality experimental data. Full-field optical measurement techniques such as Thermoelastic Stress Analysis (TSA) or Digital Image Correlation (DIC) are capable of producing maps of stress and strain which can be used for validation purposes. However, these techniques need further development to be suitable for use in a combined thermal and vibration environment.

The Air Force Research Laboratory Structural Sciences Center (AFRL SSC) has two chambers capable of combined thermal and acoustic loading in which they would like to be able to make full-field measurements on the front (heated) side of a panel. The design of these test facilities is described by Shimovetz and Wentz [2]. The smaller of the two chambers is designated the Sub-Element Facility (SEF). This chamber is capable of

testing specimens up to 300x450 mm in size with sound pressure levels of 180 dB and temperatures up to 1370 °C. The heating is provided by quartz lamps, which produce a heat flux of around 1125 kW/m^2. The second chamber is much larger and designated the Combined Environment Acoustic Chamber (CEAC). It is capable of testing specimens on the order of 2 meters square, at similar sound pressure levels and temperatures as the SEF. Currently in these facilities they are only able to make certain measurements during an experiment, usually limited to some strain gauge or other pointwise techniques on the back surface of the panel. Ideally, they desire to make full-field measurements on the front, heated side of the panel, with the aim of using the data for the validation of computational mechanics models.

1.2 Background

A large amount of the research in the area of thermoacoustic fatigue has been driven by the quest for hypersonic flight. The very high speeds encountered during sustained hypersonic flight generate aerothermal and aeroacoustic loading of the exterior of the vehicle. In addition, the engine generates heat and acoustic loading on parts of the structure. This creates a situation in which components can fail from either the acoustic and vibration loads, thermal cycle and mechanical loads, or excessive temperature [3].

Designing optimized vehicles to operate in this extreme environment is a challenge because of the cost and complexity of both simulation and testing. Often, worst-case loading scenarios are superimposed to create the design loads, which leads to over-designed structures. There is also a lack of full-field measurement data to validate what are already very challenging and complex computational models, which means that designs must be conservative. Designs created in this fashion tend to be inefficient and costly which for high performance hypersonic vehicle programs could even result in the program being

cancelled [4]. Therefore, there is a strong motivation to develop techniques that permit validation-quality data to be acquired in efficient and realistic experiments that address both the structural and temperature aspects.

The majority of structural level testing in this area has been performed using a progressive wave tube (PWT). A PWT is capable of simulating wideband random excitation up to sound pressure levels on the order of 160 dB and are typically sized to test components that are 1 meter by 0.5 meter [5]. Steinwolf *et al.* showed that with modern digital feedback control, it is possible to tailor the acoustic output of a PWT to closely match that of a jet engine [6].

Recently, an experiment was conducted using the AFRL SSC and the Propulsion Directorate's large scale supersonic combustion research facility by Beberniss *et al.* [4]. A high-speed continuous flow wind tunnel (designated RC-19) was used to subject a small, thin steel panel to a shock impingement. The response of the panel was measured using 3D digital image correlation with a pair of high speed cameras to get displacement and strain information.

All of the tests performed in a PWT so far have utilized point-wise measurement methods such as strain gauges and laser vibrometers. The test by Beberniss *et al.* using the high speed wind tunnel is one of the few examples of digital image correlation to measure the vibration response of a panel. For the purposes of validation of computational models for life prediction of a component, single measurements may not be sufficient. There is a need for high quality, full-field data from structural vibration experiments.

Using the full-field data for validation purposes presents its own set of challenges. Typically, experimental data and simulation results are collected on different coordinate systems with different spatial orientations and spacings. Therefore it is often necessary to remap data from one system to another. There is also a need to better understand the

uncertainty in experimental measurements made using full-field methods. All of these things will need to be considered in the development of a validation procedure that uses full-field experimental data.

The use of digital image correlation for high temperature measurements is relatively recent, and the process is still maturing. Most of the published results are 2-D measurements of static or quasi-static experiments. It is only recently that dynamic measurements have been attempted at high temperature. Abotula *et al.* used a pair of high speed cameras to capture the deformation of Hastelloy samples at various temperatures under shock wave loading [7]. As the ultimate goal is to use the validation procedure on thermoacoustic computational models, there is a need to develop the DIC technique to be suitable for use in a combined high temperature and vibration environment. It is not until this has been addressed that validation can be attempted.

1.3 Aims and objectives

The long-term aim of this project is to develop and implement a methodology to measure strain and stress fields in structural aerospace components at AFRL during thermoacoustic fatigue loading for the purposes of model validation. The research presented here was funded by the U.S. Air Force to take the first steps towards that ultimate goal. The specific objectives of this thesis are therefore to:

- develop a low-cost methodology to measure validation quality data during vibration loading.
- perform a validation of a computational solid mechanics model using full-field experimental data from an experiment with dynamic loading.
- demonstrate the capability to make high temperature measurements of a vibrating panel with digital image correlation.

Chapter 2

Literature Review

The desire to achieve hypersonic flight, or flight at speeds in excess of Mach 5, has presented many challenges to the materials and structural design community. One such challenge is thermoacoustic fatigue resulting from the hypersonic flow and acoustic pressure from the engine. There have been several major phases of research on thermoacoustic fatigue in relation to experimental project planes sponsored by the U.S. government. The first such program was for the X-15 plane, which lasted from 1954 to 1968. The X-15 vehicle was rocket-powered, which meant that it did not require oxygen from the atmosphere to produce thrust.

The next major hypersonic program was the X-30 National Aerospace Plane (NASP), which started around 1982 and lasted just over a decade until it was cancelled in 1993. The X-30 was a joint program between NASA, DARPA, and the USAF to create a hypersonic, single-stage to orbit vehicle. Unlike the X-15 program, the X-30 was intended to be powered by an air-breathing scramjet engine. This type of engine configuration presented some unique challenges in terms of high temperature acoustic loading on the inlet ramp and exhaust portions of the engine.

Whereas the X-15 had been rocket powered and therefore did not need an atmosphere containing oxygen for combustion, the scramjet engine on the X-30 would be air-breathing, which meant that it had to operate at a lower altitude and would therefore be subjected to thermal and structural loading generated by flying at speeds of Mach 25 in the atmosphere. It was observed by Leatherwood *et al* that the vehicle would therefore

encounter extreme conditions [8], including:

- Extremely hot surface temperatures
- Large temperature gradients
- Transient heating
- Very high acoustic pressures

The potential implications of these extreme conditions were extensive:

- Large static (thermal) stresses superimposed on dynamic stresses
- Changes in material properties that manifest as changes in strength and modulus of elasticity
- Accentuation of non-linear behavior
- Changes in fatigue behavior
- Complex thermal and structural boundary conditions that may be difficult to simulate experimentally
- Difficulty obtaining reliable experimental structural response measurements

Ultimately these challenges proved too costly to address at the time, and the program was cancelled in 1993. However, as a result of the program a great deal of research was performed in the areas of acoustic and thermal acoustic fatigue of various panel geometries. A series of programs were initiated to facilitate technology transfer and keep the research alive. The X-43A was an un-piloted, 3.7m long, 1300kg research vehicle of which three were built and flown. The vehicle was not designed to be reusable, so it had to transmit data during flight as it crashed into the ocean and was not recovered at the end of the flight. The first vehicle was terminated (blown-up) by the safety officer due to a loss of control. The second vehicle operated under scramjet power successfully for 11 seconds, reaching Mach 6.83 at 29,000m. The third and final vehicle attained a speed of Mach 9.68 at an altitude of 34,100m.

Research into scramjet engines currently continues in the X-51 Waverider program which was initiated in 2004 by the U.S. Air Force. Like the X-43 vehicles, the X-51's are not designed to be recovered after flight. A total of four vehicles have been built, with one successful test flight so far, which occurred in 2010. The vehicle was launched from a B-52 and under rocket power attained a speed of Mach 4.5, at which point it transitioned to scramjet power for 200 seconds, reaching Mach 5.

While there has undoubtedly been a wealth of experimental data collected from the flights of the X-43 and X-51 programs, it does not appear to have been publicly released at this point. Research in the acoustic and thermoacoustic area has continued in the public domain, but it has been more focused on modeling and simulation, with a few exceptions.

As the aim of this thesis is to increase the understanding of the coupled thermoacoustic fatigue failure of aircraft structures and materials through the development of novel, full-field experimental methods, this review will focus on the experimental aspect of the research in this area. Experimental and numerical methods have developed in tandem over the last several decades of research into thermoacoustic fatigue, but the experimental methods have been lagging behind until recently when there has been more widespread use of optical techniques, high speed imaging systems, and increased computational capabilities.

The first part of the review focuses on the various panel experiments that have been largely motivated by the aerospace industry. The section is therefore loosely structured into the three main time periods defined by the different experimental plane projects. The first major bit of research resulted from the X-15 program, with follow-on results generated well into the 1970's. The next significant research was generated by the X-30 program in the 1980's into the early 1990's. Most recently, research has been generated by

the X-43 program as well as other funding initiatives such as the US Air Force Structural Sciences Center.

The second part discusses different methods of acquiring full-field displacement and strain data with the aim applying the techniques to a vibrating component. This includes methods that cover a wide range of physical scales and types of data capture.

The third part gives a review of the recent developments in validation methodologies for full-field measurement techniques. Although the use of experimental data for the validation of computational models certainly is not a new topic, the use of full-field methods is relatively recent. This is due largely to the complexity of making a meaningful comparison with large amounts of data. An important aspect of validation is uncertainty quantification, so this part includes a section to review that.

The final part examines the state of the art in high temperature DIC and TSA experiments. Particular interest is the use of these techniques with vibration or other experiments that require high speed imaging.

2.1 Vibratory panel experiments

Work was performed by Clarkson at the University of Southampton with Air Force funding to summarize experimental data detailing the stresses induced in typical aircraft structure by jet noise at take off [9]. Data was examined from single flat and slightly curved plates with fully fixed edges of approximately A3 dimensions which were excited by jet engine noise on the order of 125-155 dB of overall sound pressure level. Some control surface areas of A5 size were examined with an overall sound pressure level (OASPL) of 140-160 dB. Strain gauges were placed in 1-3 different locations to calculate stress levels. The sound pressure level on a tail unit surface was measured during take-off and climb to 12,100 m, and was found to increase as the altitude increased. The frequency

spectrum broadened and the frequency peak shifted down. Some limited results for stress level as a function of the number of cycle were given for two of the panels. The analysis was focused only on the acoustic aspects and did not include any information on thermal effects.

Work was done by Schneider at the Lockheed-Georgia Company under Air Force funding to establish tolerance levels and design criteria for acoustic fatigue prevention in flight vehicles [10]. Experiments were performed on 7075-T6 aluminum and 6Al-4V titanium specimens at room temperature and at elevated temperature. The elevated temperature for the aluminum specimens was 150 °C and the elevated temperature for the titanium specimens was 315 °C. This was primarily an experimental program, but some initial analysis was performed to establish the parameters to be measured and also to correlate with the experimental results. The first set of experiments were of cantilever beam specimens approximately 50x150 mm. The specimens were clamped at one end and excited using random amplitude vibration on a shaker. Strain gauges were placed at the root of the cantilever near where the parts were clamped, but gauges were only used on the room temperature specimens. Periodic inspections using sine wave excitation were performed to determine the natural frequency of the specimen as the test progressed. The specimens were considered to have failed when the resonant frequency had decreased by 2%.

The next set of experiments were performed using acoustic excitation in a progressive wave tube. The panels were approximately 550 mm by 800 mm and were stiffened with ribs on one side. During the test, a panel was installed such that the stiffeners were located on the inside of the tube with the skin facing out. For the elevated temperature tests the skin was then heated by a bank of 2500 W quartz lamps. Excitation spectrum shaping was performed for each panel at the desired test temperature by determining the fundamental

response frequency. If the panel had a single-mode response, a narrow 100 Hz bandwidth excitation spectrum was used. If the panel had a multi-mode response, a bandwidth of approximately 300 Hz was used, which was shaped to obtain a flat response using 1/3 octave band spectrum shaper. The panels were inspected periodically during testing, at intervals ranging from 15 minutes to an hour, based on the amount of time that had elapsed since the start of the test. For the elevated temperature tests, this meant that the panel had to undergo a cooling and re-heating cycle every time it was inspected.

The gauges also had limited fatigue life due to the large amplitudes encountered during testing. The study produced a large amount of experimental data, however Schneider found that for the more complicated stiffened panels, the results didn't correlate very well with the analytical models. Particularly for the thermal buckling, as it was assumed in the analysis that the substructure was thermally isolated.

Leatherwood *et al* performed a series of tests on simulated aircraft panels made from carbon-carbon composite and also a system being developed which was called the Thermal Protection System [8]. The tests were performed using the Thermal Acoustic Fatigue Apparatus (TAFA) at the NASA Langley Research Center. The TAFA is a progressive wave tube type testing facility that provides acoustic energy using a pair of WAS 3000 electropneumatic modulators with 30 kW of power each. These modulators can produce an OASPL of 135-169 dB over a spectrum of 30-500 Hz. The facility can test a panel up to 1.5 m square, and can provide heating using a bank of 12 quartz lamps. The lamps produce 2500 W of power each, resulting in approximately 45.4 kW/m^2 of heat flux.

A total of four carbon-carbon panels were tested to failure using the TAFA. Two of the panels were simple flat plates sized 304x337 mm by 2 mm thick. The other two panels were the same size, but contained three 25 mm tall blade stiffeners on one side of the panel. All of the carbon-carbon panels were coated with silicon carbide and sealed

with sodium silicate. This made the installation of strain gauges onto the surface a very difficult process, requiring microblasting, baking, application of ceramic adhesives, curing, and plasma spray application of various coatings. The flat panels were installed into the chamber fully clamped around all four edges in a picture frame type of fixture. The blade-stiffened panels were only clamped on the two sides parallel to the stiffeners while the other two sides were left free.

Unlike the carbon-carbon panels, the TPS panels were not tested to failure. The composition of the panel consisted of a superalloy honeycomb made of Inconel, titanium, Dynaflex, and Q-fiber. Three different panels were tested, with three different skin thicknesses. The total panel thicknesses were approximately 60 mm. As the TPS panels had a metallic skin, traditional high temperature strain gauge adhesives and application methods could be used. The maximum measured strain was on the panel with the thinnest (64 micron) skin, which was 33 microstrain at 160 dB.

The panels were excited with broadband acoustic noise in the 30-500 Hz range at 160 dB. For the elevated temperature tests, the quartz lamps were used to achieve an initial test temperature of 540-650 °C on the surface of the panel. However, the high acoustic pressure caused lamp failures as the test progressed, with the final temperature falling to 177-316 °C depending on test duration. The change in the first mode frequency was monitored as a way to detect panel failure. For the flat, room temperature panel the first mode frequency dropped from 126 Hz to 100 Hz and failed after 38 minutes. The high temperature flat panel lasted 151 minutes, but all of the gauges had failed by this point so an accurate determination of the first mode frequency was not possible. It was found that the flat panel cracks were developing under the clamping bars, and were therefore not visible until they propagated into the viewable area. It was also found that both of the blade stiffened panels failed much sooner than their flat counterparts, probably due

to the boundary conditions imposed on them. As they were only clamped parallel to the stiffeners, it was conjectured that the stiffeners provided no benefit but rather added mass which contributed to the failure occurring sooner. Both the flat and the blade-stiffened panels did show increased fatigue performance at the elevated temperature test, which was encouraging.

The carbon-carbon panels had a high rate of gauge failure as compared to the TPS panels. Low indicated strains of only 5-20 microstrain were thought to be erroneous, but later analysis revealed that it might have been due to non-linear stiffening in the panels.

An extensive report was released by Blevins *et al.* which was the second phase of a three phase study sponsored by AFRL [11]. The aim of the study was to identify a typical trajectory into orbit and to use that to determine the aerothermal and acoustic loads that a vehicle would encounter. These loads were used to design forebody, ramp, stabilizer, and nozzle skin panels which were then analyzed to determine the temperatures as well as the mean and dynamic stresses in the panels. The report includes results from extensive analysis of the panels, but it was planned to do the testing and validation in the third phase, for which there was a detailed validation and verification plan. If the third phase of research has been completed, it does not appear to have been released publicly at this point.

As the previously described report was not released until several years after the research was completed, Blevins and his co-workers published a journal article based on the research that briefly described the flight trajectory and some of the results [3]. The paper presented analysis based on two ascent flight trajectories with different limiting dynamic pressures. For a limiting dynamic pressure of 50 kPa, the maximum temperature for the forebody panel is 1460 °C. At a dynamic pressure of 125 kPa, the maximum temperature of the same panel is 1790 °C. To meet these temperature requirements, two

main candidate materials were considered: carbon-carbon panels with a silicon-carbide coating, and titanium metal matrix composites (TMC). The blended wing body (BWB) concept that was analyzed has the engine placed amidships such that the forebody acts as a compression surface for the engine, and the aftbody acts as an expansion nozzle. As a consequence, the forebody, ramp, and nozzle panels are subjected to severe thermal and acoustic loading. Blevins *et al* estimated for the projected 100 flight life cycle for the BWB concept that these panels would encounter over 20 million vibration cycles.

Designs were proposed for the forebody and ramp panels that were carbon-carbon construction with blade stiffeners. The designs for the two panels were similar, but the ramp panel was not required to bear any structural loads, so it had a wider stiffener spacing and a thinner skin. It was determined that the peak heat flux in the panels could be as high as 600 kW/m^2 with temperatures ranging from 1140-1790 °C, depending on ascent trajectory and the laminar/turbulent flow. The aeroacoustic loading on the panels was found to be 130-145 dB, while emissions from the engine could be as high as 170 dB. The analysis showed that the lowest mode of vibration for the forebody panel was 524 Hz, and the lowest mode for the ramp panel was 258 Hz.

The operating conditions for the aftbody nozzle panel were more severe than those for the forebody and ramp panels, so it was proposed to use an actively cooled panel. The panel was to be constructed of a titanium core through which liquid hydrogen would flow through milled passages, and the panel would be faced with titanium matrix composites. The fundamental bending mode of the panel through analysis was found to be 82 Hz, due to the panel's low stiffness and relatively large (1.2 m by 1.2 m) dimensions. The average heat flux at the combustor exit was 2000 kW/m^2 and maximum acoustic loading occurred at take-off at 170-180 dB. The maximum stresses were found to be on the inner face sheet at the center of the panel, and occurred during take-off. Without additional

stiffening, the loads exceeded the fatigue capability of the panel.

Also as a result of the NASP, a large scale supersonic combustion research facility was created at Wright-Patterson AFB [12]. The combustion facility was designated as RC-19 and contains a primary test section that is 150 mm wide and 130 mm high, and contains viewing windows made from fused silica. While primarily designed to study combustion in flows up to Mach 2, Beberniss *et al* recently used the RC-19 facility along with high-speed 3D digital image correlation to capture the dynamic response of a panel subjected to shock impingement [4].

During this same time period there was some research into acoustic fatigue conducted at the Institute of Sound and Vibration Research at the University of Southampton. The research was primarily motivated by the commercial aircraft industry, and therefore only included temperatures which were moderately elevated above ambient. White performed analysis and experiments using carbon fiber specimens at room temperature and at 120 °C [13]. PWT testing was conducted on specimens made of XAS/914 carbon fiber that were 450 mm by 300 mm and 1.75 mm thick. It was noted that the response of panels tested in a PWT can vary from actual conditions because of a higher damping in the panel caused by acoustic interaction with the tunnel.

White had previously noted that for very thin (metallic) plates excited by high sound pressure levels the response was nonlinear [14]. Ng and White also found that if there was compressive in-plane loading, there were nonlinear effects immediately before buckling and post buckling, as well as modal coupling [15]. Ng then examined the snap through effects in the post-buckled regime [16].

Cunningham and White used the PWT to test doubly curved honeycomb sandwich panels [5, 17], which was a follow-on to a previous study in which Ansys was used to perform analysis and also some free-vibration experiments were performed on the panels

[18]. The panels were 912 mm by 525 mm and mounted into the PWT using four circular steel springs. Initial experiments were performed using a glass/fiber epoxy picture frame type clamping arrangement, but it induced extra stiffness in the panels and lowered the strain response. Using the steel springs, the measured natural frequencies were close to those calculated for the free response in Ansys. The panels were excited using broadband noise in the 60-600 Hz range at an overall sound pressure level of 164 dB. The maximum RMS strain recorded were on the order of 250 microstrain.

One of the few papers which discuss the use of full-field methods to measure a vibrating panel was performed by Beberniss *et al.* at the Air Force Research Laboratory [4]. They used stereoscopic digital image correlation to measure a 305 mm by 152 mm by 0.635 mm thick 4130 steel panel mounted in the RC-19 large scale combustion research apparatus. The design of the tunnel necessitated that the panel be viewed through a window, which consisted of a 19 mm thick quartz panel. The panel was clamped in a picture-frame fashion, and was subjected to a shock impingement with a nearly Mach 2 flow. Measurements were made using a pair of high speed cameras with 32GB of memory each and 5000 frames per second with a 640x352 pixel array size.

Beberniss *et al.* noted that sonic fatigue tends to occur in thin, lightly damped structures with modes below 500 Hz, due to the larger displacements and resulting stress at the lower frequencies. The design of the test specimen was constrained by the width of the tunnel, so the length and the thickness were adjusted to get three modes below 500 Hz. Some experiments were performed using different speckle patterns, and a coarse pattern was ultimately chosen that gave an approximate noise floor of 10 microns. The out-of-plane displacement and also strain measurements obtained from the DIC were used to compute PSD functions and then compared against data obtained from a laser vibrometer. It was found that if only 5000 frames were used (equivalent to 1 second)

that the resulting PSD was fairly noisy. The results for 10,000 frames were slightly better, and those from the entire 100,000 frame recording were the best. There was found to be good agreement between the DIC measurements and those made with the laser vibrometer and the strain gauge. In an effort to reduce processing time, the DIC measurements were calculated at 21 discrete points on the panel rather than computing the entire displacement field.

2.1.1 Conclusions

There has been a fair amount of panel testing with broadband excitation over the last 50-60 years. There are really only a few facilities available in which to perform such experiments, as a large acoustic test chamber capable of 160+ dB sound levels is undoubtedly expensive. Most of the data was collected using traditional measurement techniques such as strain gauges or accelerometers. The one exception is Beberniss *et al*, who used high speed DIC to measure the response of a steel plate to a Mach 2 airflow [4]. Unfortunately, due to the issues of processing the 200,000+ images resulting from the test, they did not calculate the full-field response of the panel but rather looked at 21 discrete points.

Most of the results were also captured at room temperature or with moderate heating. Schneider did use some quartz heating of the specimens, but only to a few hundred degrees (°C). The measured strains are not very high with this type of excitation, usually only a few hundred microstrain. Leatherwood *et al.* did obtain temperatures up to 650 °C in there experiments, but had several challenges involving the failure of the heating lamps and of the strain gauges. They also observed non-linear behavior due to the high acoustic loading used in their experiments [8].

The aim of many of the studies was to develop design guidelines, so there is a lot of information on the simple analytical models to attempt to predict stress in a plate

subjected to various loading conditions. However, these analyses are not valid for the non-linear behavior of plates, which tends to occur when there is very high loading [16], or combined effects [15].

2.2 Full-field experimental methods

There are many different optical techniques available that permit the measurement of various components of displacement and strain. Generally speaking, there are two main types: Interference methods which use coherent light and methods that use non-coherent light. Interference methods include such techniques as photoelasticity and holography and rely on the wave properties of light. Non-coherent light techniques include fringe projection, grid methods, and digital image correlation. Each method has its own advantages and disadvantages, and some are better suited to dynamic and high-speed measurements than others.

2.2.1 Interference methods

Interference methods use coherent light to measure the path length (or phase) difference between two beams of light. These methods can be further divided into techniques which use a common-path beam arrangement (photoelasticity, basic shearography, Newton's fringes) and those that use a separate-path (holography, speckle interferometry, moiré interferometry, Lloyd's mirror) [19]. Separate path methods use a separate reference and object beam, and so if there is any relative motion between the optical apparatus and the specimen it can cause decorrelation in the experimental results. Common-path methods do not have this limitation, and so they are more forgiving to real-world environments. However, separate path methods are capable of measuring both object contour and deformation, while common-path methods typically are only capable of measuring

deformation.

In speckle interferometry slightly different arrangements are used to measure in-plane and out-of-plane displacements [20]. To measure out-of-plane displacements, a single beam is split into a reference beam which is directed to the image plane, and a beam which is directed to the surface of the object. To measure in-plane displacements, two separate beams are directed at the surface. This provides the displacement component of the surface in the plane of the beams. If the beams are rotated 90 degrees, then the second component of displacement can be measured. Special measurement systems have been created which combine these components to be able to simultaneously measure the in-plane and out-of-plane displacements.

In shearography, a device is placed in front of the image plane to shear the reflected beam from the surface of the object. Leendertz and Butters proposed a device which used a Michelson interferometer to shear the beam [21]. Hung *et al.* used a plate with four apertures which was moved relative to the image plane to produce the shearing effect [22]. This method effectively performs the first step of differentiation of the surface displacement, producing fringes that are related to the slope of the surface (for out-of-plane measurements) or the in-plane strains (for in-plane measurements). This is useful to find the strain at the surface of an object in a particular direction. Similar to interferometry, the system must be rotated by 90 degrees to obtain the full strain field.

2.2.2 Other methods

There are a wide variety of other methods, typically which use non-coherent light, ranging from fringe projection to digital image correlation. Most of the methods require some sort of pattern or substrate to be applied to the surface of the object to be measured, with the exception of fringe projection. In this technique, fringes are projected on to the

surface of the object, permitting the measurement of the contour. However, the technique by itself is not suitable for measuring in-plane deformation.

The grid methods and DIC are somewhat similar in that they both operate on the intensities measured from the surface of an object that is covered with a pattern. In digital image correlation, a random pattern is necessary on the surface of the object. Sometimes, the natural texture is sufficient, but typically the best results are obtained by applying a high contrast, random speckle pattern to the surface. The grid method requires that a very precise, high resolution grid is created and then applied to the surface of the object [23]. In both methods the deformation of the pattern is tracked from one image to the next in order to create a map of displacements for the surface of the object. The displacement map can then be differentiated to obtain strains.

The advantage of using a grid over a random pattern is that a smaller subset of pixels is required to map the deformation from the reference image. For example, Pierron *et al.* used the grid method with a 6x6 pixel subset size for the measurement of strains in a composite open-hole specimen subjected to tensile loading [24]. A variation of the method was developed by Badulescu *et al.* to directly compute the strains from the intensity map without computing the displacements first [25]. This reduced the noise that is normally introduced in the differentiation process when computing strains from displacements. The technique has also been shown by Ri *et al.* to be able to measure relatively small displacements over a large field of view [26]. They obtained a noise level of less than 4 microns over a 1000 mm field of view. The primary disadvantage of the grid method (at this point) is that it is only suitable to measure in-plane displacements.

Another technique is deflectometry, which was used by Surrel and Grédiac *et al.* to measure the slope of bent plates [27, 28]. In this technique a reflective coating is applied to surface of the object, which is then illuminated with a coherent light source. The

reflected light is then passed through a grid which produces a phase map relating to the slope contours of the object. The technique has the advantages of directly measuring the slope and is relatively insensitive to vibrations because it measures the direction of light propagation and not a path length difference like interference methods. More recent measurements have simplified the technique and demonstrated that it is not necessary to use coherent light [29].

2.2.3 Application to vibration measurement

Recent advances in computers and camera sensor technology means that most techniques can be performed digitally, without the use of photographic films or other mediums. There are two primary types of imaging sensor: the charge-coupled device (CCD) and the complimentary metal-oxide-semiconductor (CMOS). Laboratory and machine vision cameras tend to have CCD sensors while high-speed cameras have CMOS sensors. This means that for the capture of vibration or other dynamic events, the limitation is usually in the imaging system. The interference methods are an exception, as they often require phase-stepping, in which multiple images would be acquired at the same object state. However, for steady-state vibration measurements, the interference methods permit the use of time-averaging to capture modal information. To accomplish this the measurement duration is set to be longer than the period of vibration. This works because the vibrating object spends most of its time at the extrema of vibration, so this is what is recorded by the imaging system. Moreau *et al.* used time-averaged electronic speckle pattern interferometry to measure the vibration of a 100x150x5.1 mm PVC plate [30].

For the other methods, there are really two primary approaches to capture digital images of dynamic events: stroboscopic illumination or a short exposure (integration) time. Stroboscopic illumination consists of using a light source with a short pulse duration

to freeze the motion of an object such that it can be recorded by a camera. There are many different types of light source which have varying intensity and pulse duration. This type of illumination has been used successfully in many types of measurement in the past and has recently been applied to digital image correlation [31, 32, 33]. Table 2.1 gives an overview of the different acquisition and illumination methods.

Table 2.1: Comparison of the different methods of image acquisition for fast-moving objects. In the case of the high-speed cameras, the exposure time refers to the minimum length of the exposure (or shutter time) that can typically be obtained. In the case of the illumination sources, it refers to the minimum time duration of each light pulse.

	Type	**Exposure Time**	**Frequency**
High-speed cameras	Continuous, bright light	1 μs	100,000+ Hz
Stroboscopic illum.	Arc lamp, LED, etc.	10 μs	10,000 Hz
Pulsed-Laser illum.	Nd:YAG laser	$4 * 10^{-3}$ μs	10-100 Hz

Patterson and Greene used stroboscopic illumination for the photoelastic analysis of compressor blades [34, 35]. The compressor blades were excited at a resonant frequency using a high speed air jet. Synchronization of the blade vibration and the stroboscopic illumination was performed by displaying signals from vibration and illumination sensors on an oscilloscope and adjusting the strobe pulse by use of a skew control. This allowed the point of maximum excursion of the blade to be captured by the camera sensor.

Han *et al* used a pulse modulated laser diode to make photoelastic modulated (PEM) ellipsometry measurements of thin films [36]. The laser was sent through a photoelastic modulator and then a beam expander, before it was reflected off of the surface of a specimen and read by a CCD camera.

Moneron *et al* used a xenon arc lamp with a 10 microsecond flash duration and a repetition rate of 15Hz for optical coherence tomography [37]. For the procedure, two CCD cameras are used to capture interferometric images which could not have any motion blurring.

While the typical method of providing pulsed illumination is arc discharge lamps

or even LEDs, it is also possible to get good results using pulsed laser illumination. This method has the advantage of having very short pulse duration as compared to more traditional methods, which allows the capture of very fast motion. To make measurements of a flywheel rotating at high speed, Schmidt *et al.* found that traditional arc-discharge light sources did not have a short enough pulse duration, so they used a pulsed laser with a single CCD camera [31]. They used a Nd:YAG laser with a 6 nanosecond pulse duration, which permitted measurements of the flywheel of speeds up to 35,000rpm.

There are even techniques which take advantage of the double-pulse capability of lasers to be able to capture two images separated by some fixed time. Pedrini *et al.* used double-pulse electronic speckle pattern interferometry to measure vibrating objects [38, 39]. The system they used was capable of firing the laser pulses with a delay of 5-1000 microseconds between them. Two different experimental arrangements were used; a single-beam system to measure out-of-plane displacement and a dual-beam system to measure in plane deformation in one plane. There have been commercial systems created that use three beams and three cameras to fully capture the deformation of the surface [40].

Another possible approach to capture images of a vibrating component is to use very bright, constant illumination and a short shutter time [41, 42]. With this method, the motion of the object is frozen by the very short shutter time. For example, the AVT Stingray firewire camera has a minimum acquisition time of 20 microseconds. Poncelet *et al* used this approach to make DIC measurements of a steel specimen during a biaxial fatigue test [41]. The illumination was provided by two 400W tungsten lights and two 3x3W LED arrays.

The other common approach is to use high-speed cameras. There are many manufacturers, but two well-known ones are Photron and Vision Research. These cameras

typically have minimum acquisition times of 1 microsecond and framerates that can approach 1 million frames per second. The trade off is that as the framerate is increased, resolution typically decreases. For a high speed camera to achieve its maximum framerate, the image array size may only be 64x12 pixels. This is a disadvantage for digital image correlation, as it will cause a decrease in the spatial resolution [43].

Reu published a survey of high and ultra-high speed cameras along with some practical considerations for DIC measurements [44]. To achieve their extreme framerates, ultra-high speed cameras employ various methods including rotating mirrors, beam-split optical paths, and memory on the chip. These cameras all have issues with DIC that have to be addressed to make quality measurements. High-speed cameras, on the other hand, are somewhat better suited to DIC measurements. The cameras typically use a large complementary metal-oxide-semiconductor (CMOS) sensor as opposed to the CCD more commonly used in machine vision cameras. One potential issue with both types of cameras is synchronization. If the cameras are not properly synchronized, large errors in the measurements could result.

2.2.4 Conclusions

Interferemetric methods like speckle interferometry and shearography are capable of producing accurate measurements with high resolution, but they tend to be sensitive to vibrations in the environment. Speckle interferometry is particularly susceptible to vibration, typically confining it to use on an optical bench. Shearography is more vibration resistant, but it still requires a somewhat complicated setup which might limit its use in an environment such as the CEAC.

Digital image correlation is a fairly robust technique, and is much less sensitive to vibration and rigid body motions than the interferometric techniques. The setup is

relatively simple, requiring only two cameras to capture both in-plane and out-of-plane deformations. The sensitivity of the technique is largely dependent on the quality and array size of the camera sensor, and so as improvements are made DIC will benefit directly. DIC is perhaps not as sensitive as the grid methods, but it is capable of measuring object contour and out-of-plane deformation. It also may be more adaptable to high temperature measurements, as there are commercially available high-temperature paints. Deflectometry appears promising for the direct measurement of strains in vibrating plates, but requires the application of a reflective coating that might not work well at high temperatures.

In order to capture transient events, high speed cameras are really the only option. However, for single frequency excitation there are other methods that are less expensive and can provide better results. With pulsed illumination, it is possible to use standard cameras that are much smaller and capable of recording at higher resolutions than their high speed counterparts. In addition, specialized sensors that are sensitive to other parts of the electromagnetic spectrum outside the visible range (UV and IR) are not available in high speed cameras.

2.3 Validation

Over the past 15 years, there have been several different guides, standards, and editorials published which addressed the need for verification and validation of computational models. In 1998, the American Institute for Aeronautics and Astronautics (AIAA) published a guide for the computational fluid dynamics community [45]. The Department of Defense has published several iterations of instructions regarding Modeling and Simulation Verification, Validation, and Accreditation activities, the latest of which was issued in 2009 [46]. In 2005, the *Clinical Biomechanics* journal issued an editorial statement

which defined minimal requirements for a numerical study for a paper to be considered for publication.

The most recent document published concerning the solid mechanics community is the 2006 ASME Guide for Verification and Validation in Computational Solid Mechanics (ASME V&V) [1], which incorporates material from a paper published a few years earlier by Oberkampf *et al.* [47]. An overview and summary of the guide was published by Schwer [48], who was the chair of the Performance and Test Codes (PTC) 60 committee that produced the guide. In the overview, Schwer states that one of the most common misconceptions about the ASME V&V guide was that it would provide a definitive verification and validation procedure for computational solid mechanics. Rather, it is a "foundational document" which provides a framework and defines terminology to create a standardized language. The flowchart in Figure 2.1 outlines the procedure that should be followed to compare simulation outcomes and experimental outcomes. The relevant terms defined in the ASME guide are included throughout this section, and are given in bold type.

The guide is broken up into four main sections: Introduction, Model development, Verification, and Validation. The primary concern of this thesis is the validation section, which deals with the comparison of the computational model and experimental results. Often, the terms verification and validation are used interchangeably, but there is a distinction between them:

verification: *the process of determining that a computational model accurately represents the underlying mathematical model and its solution;*

validation: *the process of determining the degree to which a model is an accurate representation of the real world from the perspective of the intended uses of the model.*

The main goal of the verification process is to ensure that mathematical models and

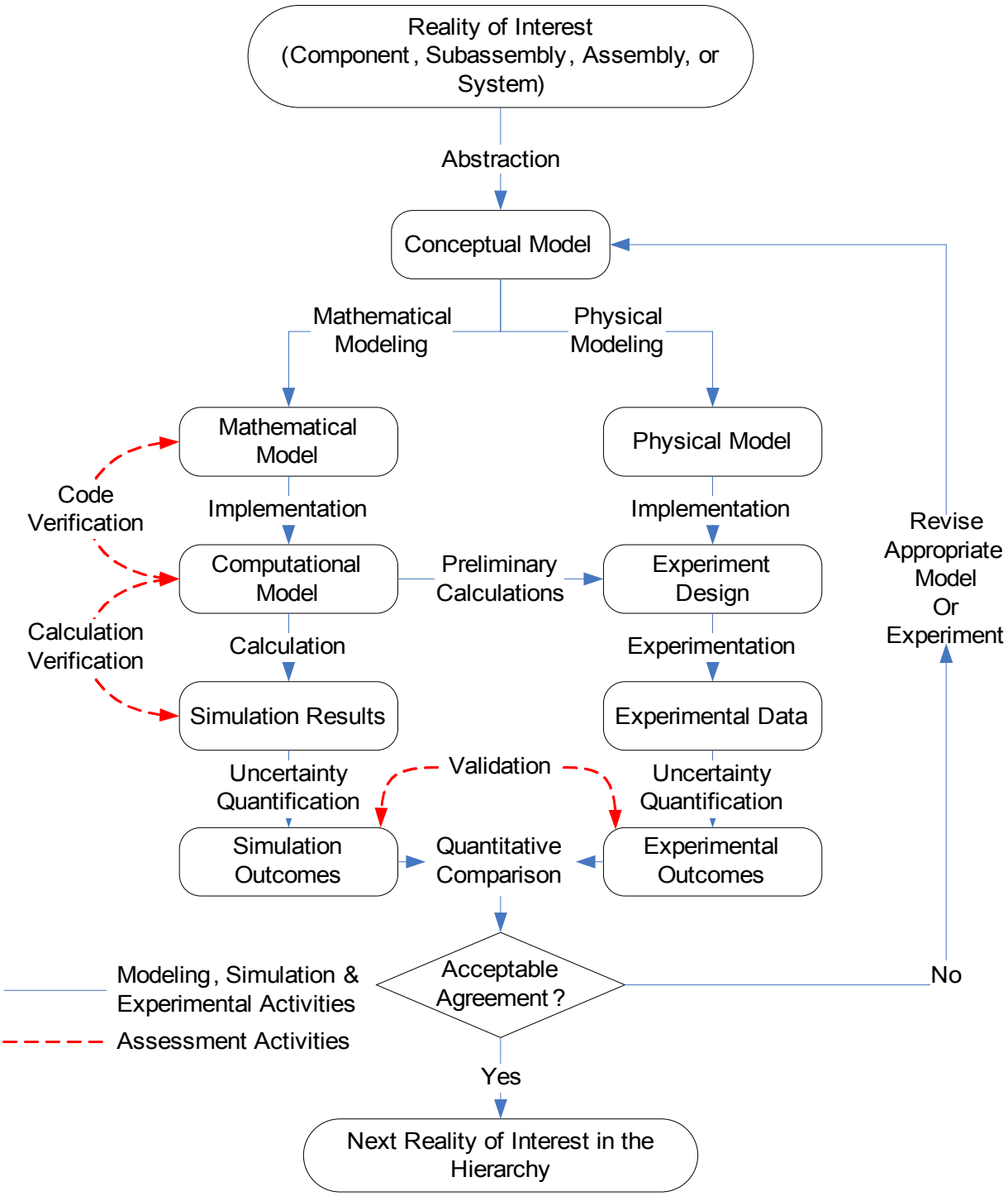

Figure 2.1: Flowchart for verification and validation activities for simulation and experimental methods [1].

algorithms used by the software are correct and that they produce accurate results, while the validation process ensures that physics of the model are correct by comparing the results to experimental data. There are also several different types of models, each representing a different concept or component.

model: *the conceptual, mathematical, and numerical representations of the physical phenomena needed to represent specific real-world conditions and scenarios. Thus, the model includes the geometrical representation, governing equations, boundary and initial conditions, loadings, constitutive models and related material parameters, spatial and temporal approximations, and numerical solution algorithms.*

Both the ASME guide [1] and Oberkampf *et al.* [47] discuss the use of metrics to make a quantitative comparison between the simulation outcomes and the experimental outcomes. The two sources differ slightly in the wording of the definition of "metric," but it is essentially a measure. The metric should quantify both errors and uncertainties, and "actively resolve assessment of confidence for relevant system response measures for the intended application of the code" [47]. In essence, the ideal metric would provide a number indicating the level of confidence in the agreement between the simulation outcomes and experimental outcomes, taking into account the error and respective uncertainties.

An examination of the literature published in the last ten years reveals that a common type of comparison is to plot the experimental data along with the computation data generated from the model together on the same plot [49, 50]. A metric is not used when performing this type of comparison. Instead, the extent of the agreement is qualitatively judged by how well the two lines match up with one another. To perform a simple quantitative assessment the relative error between the two sets of data can be calculated

according to the following equation [51]:

$$RelativeError = \frac{computation - measured}{measured} \tag{2.1}$$

The relative error metric can be effectively applied to point comparisons or lines of data, but is not very effective for more complex comparisons. For example, it is not a good choice to compare tensors, or data with time or spatial components. Also, as the measured value approaches zero, the quantity becomes undefined. This can be a problem for comparing things like waveforms, in which the signal can cross zero.

Full-field data presents similar challenges, and so the comparison is still often reduced to checking a few points rather than using the full data set. There are studies available which describe the collection of data using full-field methods, but do not explicitly describe the validation procedure, e.g. [34]. This gap was recently addressed by the author and his coauthors who proposed a quantitative procedure for validating computational solid mechanics models based on full-field measurements of strain and or displacement plus the measurement uncertainty [52].

It has been shown that shape descriptors are one potential solution to the problem of comparing the large amounts of data acquired from full-field experimental methods [53]. An orthogonal descriptor based on the Zernike polynomials was described by Teague [54]. The Zernike descriptor is continuous and valid over a circular domain. A discrete, orthogonal descriptor based on the Tchebichef polynomials was described by Mukundan *et al.* [55]. Unlike the Zernike descriptor, the Tchebichef is not invariant to rotation, however the fact that it is discrete and valid over a rectangular domain makes it well-suited to full-field experimental data. Wang and Mottershead provide an overview of the different shape descriptors as well as some other methods of image decomposition along with their respective advantages and disadvantages [56]. They noted that the Tchebichef

moments are better suited to detecting global features, while Krawtchouk moments are suited to detecting local features [57].

Wang *et al.* have used a variety of shape descriptors to tackle full-field data from various engineering problems. They used a modified Zernike descriptor to compare the strain around a hole of a plate loaded in tension to the results from a computational model [58]. They have applied the Tchebichef moments to examine mode shapes resulting from vibration measurements [59], and an adaptive geometric moment descriptor for the vibration of a car bonnet liner [60]. The adaptive geometric moment descriptor was also used to track the evolution of damage to the car bonnet liner subjected to an impact from a high speed projectile [61]. Sebastian *et al.* used Tchebichef descriptors to compare strain data from a composite protective panel to simulation under compressive loading [62]. Recently, Allemang *et al.* used Principal Component Analysis to compare two sets of experimental data from frequency testing of an automobile chassis [63].

2.3.1 Measurement Uncertainty

According to the International Vocabulary of Metrology (VIM) published by the BIPM, uncertainty [1] can be evaluated by two methods [64]:

Type A: *evaluation of a component of measurement uncertainty by a statistical analysis of a series of observations;*

Tybe B: *method of evaluation of uncertainty by means other than the statistical analysis of a series of observations.*

By itself, this is a little confusing, as it basically classifies the evaluation methods into statistical analysis and "everything else." Fortunately some examples of Type B evaluation

[1] **uncertainty (of measurement)** non-negative parameter characterizing the dispersion of the quantity values being attributed to a measurand, based on the information used [64].

are provided, including evaluation based on information: associated with authoritative published quantity values, obtained from a calibration certificate, and drift, (among others).

The majority of the literature deals with statistical analysis of measurement results, so Type A. There are many different components that contribute to the measurement uncertainty, and it is understood that it is not necessarily possible to capture them all. This is reflected in the definition of measurement uncertainty, which states "based on the information used." There are two types of error that contribute to the measurement uncertainty:

systematic measurement error *component of measurement error that in replicate measurements remains constant or varies in a predictable manner;*

random measurement error *component of measurement error that in replicate measurements varies in an unpredictable manner.*

where the measurement error is defined as a measured quantity value minus a reference quantity value. In the case of systematic error a correction can be applied to compensate, whereas this is not true for the random component.

Until recently, much of the analysis of errors and uncertainty in DIC has been performed using 2-D systems, often using simulated or numerically modified images. A survey by Pan *et al.* [65] discusses the basics of 2-D DIC including the different correlation algorithms and also displacement error analysis. Haddadi *et al.* [66] divide the sources of error into two main categories: those related to experimental setup and imaging, and those from the correlation algorithm. Haddadi *et al.* attempt to quantify these sources of error by performing rigid body translations of a specimen. Various other methods have involved synthetically deforming images, either by applying a sinusoidal displacement [67, 68] or applying the results of a finite element simulation to deform the

speckle images [69, 70, 71]. Further, Wang *et al.* examined the effects of noise on 1-D and 2-D motion measurements [71].

There has been some analysis of uncertainty for 3-D setups. Becker *et al.* examined the parameter calibration and resulting errors, including examining the lens distortions resulting from a short focal length [72]. Siebert *et al.* compared 3-D DIC to Electric Speckle Pattern Interferometry (ESPI) and strain gauges in a tensile test, as well as performing some limited dynamic experiments with a cantilever [73]. There has been some work on the effects of camera alignment and position error by Sutton *et al.* [74] and Lava *et al.* [75]. Recently, Reu examined the uncertainty resulting from parameter calibration by processing different subsets of a pool of several thousand images [76]. Zappa *et al.* performed some work relating to high-speed DIC, in which they examined the effect of movement during the measurement process [77].

This prior research has done much to expand the understanding of how 2-D and 3-D DIC performs under a variety of controlled conditions, but it does not necessarily give a researcher or engineer a clear idea of the level of uncertainty associated with a particular setup. The Standardisation Project for Optical Techniques of Strain measurement (SPOTS) sought to address this shortcoming, and developed procedures for the calibration and evaluation of optical measurement systems [78]. Following the SPOTS procedure, Whelan *et al.* published the results of performing a calibration of an ESPI system [79] and Sebastian and Patterson that of a 2-D DIC system [80]. More recently, the same procedure was used to quantify the uncertainty in a 3-D setup used for large deformation measurements by Tan *et al.* [81]. The aim of the calibrations was to provide a level of confidence in the measurement system by quantifying the uncertainty over the measured strain range.

2.3.2 Conclusions

The validation of computational mechanics models is an ongoing topic, with some recent work performed using image decomposition to make use of full-field experimental data. The use of image decomposition can compress the large amount of redundant data when comparing full-field experimental and simulation results. The Tchebichef descriptor has been successfully applied to modal analysis of rectangular plates by Wang *et al.*

There are some published guidelines for assessment of in-plane measurement uncertainty, and some examples of such. However, there are currently no examples for the assessment of measurement uncertainty in a dynamic, out-of-plane, full-field measurement system.

2.4 High temperature DIC

There are three main challenges associated with high temperature DIC measurements: increased blackbody radiation, temperature resistant coatings, and blurring due to refraction of the heated air. Traditional DIC methods without any special optical setup and commercial high temperature paints permit measurements up to about 650 °C before the first two issues become problematic. Turner and Russel were able to measure the coefficient of thermal expansion on different metals at temperatures up to 600 °C [82].

The third challenge is often neglected in the literature, perhaps because it is less obvious than the other two. Whereas the blackbody radiation and degradation of the coating can be easily observed by the naked eye, thermal refraction effects will manifest themselves as errors in the DIC images long before they can be observed. Lyons *et al.* examined this phenomena during the measurement of thermal expansion and tensile performance of nickel alloys at 650 °C [83]. The experiments were performed with the specimen in furnace, and they found that the temperature variation in front of the window

caused displacement components of a non-random character. To correct this, a small fan was placed in front of the window to mix the air and create a constant temperature.

In the last few years researches have been addressing these issues and so DIC has been successfully applied to a variety of measurement situations at even higher temperatures. Grant *et al.* presented the method of using blue light along with a $450 \pm 25nm$ bandpass filter to measure the coefficient of thermal expansion of RR1000 (a nickel based alloy) at temperatures up to 1000 °C with 2D DIC [84]. They do mention the refraction problem, or "heat haze" as a potential source of error although it was not observed to be an issue in their measurements.

Pan *et al.* and Chen *et al.* used a similar setup but with two cameras to make 3D measurements at temperatures up to 1200 °C and 1100 °C, respectively [85, 86]. Later, Pan *et al.* was able to measure the surface strains of a C/SiC composite at temperature up to 1550 °C [87]. However, they found that, using blue lights and filter, glowing of the specimen increased greatly in the images at temperatures above 1400 °C. To overcome this, Berke and Lambros used an Ultraviolet camera along with illumination and filter to measure Hastelloy-X (nickel based alloy) at up to 1260 °C [88]. They note that the limitation of their experiments was the melting point of the material, but that the shorter wavelength of UV light (compared to blue light) should permit the use of the technique at higher temperatures.

It is only recently that dynamic measurements have been attempted at high temperature. Abotula *et al.* used a pair of high speed cameras to capture the deformation of Hastelloy samples at various temperatures under shock wave loading [7]. Illumination is always a challenge with high speed measurements, and this is magnified when using a high temperature DIC setup which makes use of filters. Abotula *et al.* used a 450nm filter with a FWHM (Full-Width at Half Maximum) of 40nm and a transmission efficiency of

only 45% which dramatically decreased the amount of light reaching the camera sensors. To overcome this, they used a high energy flash lamp which was capable of delivering 220kW to the specimen for 5ms.

Standard paints which are well-suited to room temperature measurements typically are not designed to handle temperatures of several hundred degrees Celcius or more. For temperatures up to 1000 °C several companies manufacture off the shelf paints that are available in flat black and flat white that have been shown to work well for DIC [7, 89]. Other researchers have created their own high temperature coatings. Pan *et al.* combined cobalt oxide with a commercial high temperature inorganic adhesive to create a black liquid that could be splashed on the surface to create the speckle pattern [85]. Chen *et al.* created a coating using amorphous precipitated silica and titanium dioxide that they used in temperatures up to 1100 °C, and which they found to be more ductile than ceramic coatings [86]. Grant *et al.* used the natural variation in surface contrast that occurs from oxidation of a nickel based alloy at temperatures up to 1000 °C [84]. Guo *et al.* were able to make measurements up to 2600 °C on carbon-carbon composites sprayed with tungsten particles [90]. A combination of neutral density and bandpass filters were used to acquire the images at such high temperatures. However, with this arrangement all of the images were acquired with the specimen at elevated temperature.

2.4.1 Conclusions

The challenges associated with blackbody radiation and high temperature coatings have largely been addressed in the literature. Guo *et al.* showed that if all of the images for an experiment are captured at the same temperature, DIC can be used at 2600 °C , possibly higher [90]. However, if the experiment is to take place at different temperatures, such as when determining the coefficient of thermal expansion, then there is some limit imposed

by the glowing that results from increased blackbody radiation of the specimen. Lyons *et al.* performed measurements with a standard optical setup at 650 °C [83]. Pan *et al.* found that by using blue bandpass optical filters and blue light illumination that the practical limit was raised to around 1400 °C [87]. Berke and Lambros explored the use of UV filters and cameras to bypass this, but were ultimately limited to 1260 °C due to the melting point of the material [88].

Dynamic measurements at temperature are especially challenging, with the only published example at this time performed by Abotula *et al.* for shock wave loading [7]. At this time there are no published results of using DIC at high temperature for vibration measurement. Clearly, there is still room for exploration and improvement in the area of dynamic measurements at high temperatures.

The issue of refraction or "heat haze" has not been discussed much, so it may potentially not be an issue, although Lyons *et al.* found that it caused nonuniform displacements in their results [83]. The effects will certainly differ depending on the particular setup and heating method used, so it should be evaluated on a case by case basis.

2.5 Identification of knowledge gaps

There is a lack of full-field data for panels subjected to vibratory/acoustic loading. Most of the experiment were conducted with a few point-wise measurement transducers, so there is an opportunity to learn more about the response of panels to random excitation by using full-field measurement methods.

To capture images of a vibrating panel would either require high-speed cameras or some form of stroboscopic illumination. High speed cameras are expensive and are not available in the UV range, which could limit their usefulness for high temperature DIC measurements. There are no examples that capture full-field data from a panel subjected

to random vibration loading without the use of high speed cameras, so a system which could do this using standard cameras would be novel.

The validation of computational models is very much an ongoing research topic. As full-field methods of stress and strain analysis are being used more and more often, the issue of how to make a meaningful comparison with so much data becomes an issue. There is a lot of potential research and exploration to be done in this area.

While there has been a lot of research recently using digital image correlation at high temperatures, the limits of UV cameras and filters has not been thoroughly explored. There is a lack of information regarding the full-field response of panels to high temperature vibration excitation.

Chapter 3

Apparatus, Method and Specimens

This chapter provides a description of the experimental apparatus and methods used in this thesis. The first section provides a reference for the various experimental equipment and apparatus used. This includes the details and specifications of such things as the cameras, the pulsed laser, and the laser vibrometer.

The next section provides details of the specimens used in the experiments. The aerospace panel was used for the validation experiments described in Chapter 6 and the Hastelloy-X plates were used in the high temperature experiments in Chapter 7.

The final section describes the basic theory behind Digital Image Correlation, which is the primary full-field experimental technique used in this thesis.

3.1 Apparatus

3.1.1 Conventional DIC

Dantec Dynamics Q-400

This is a commercially available DIC system (Q-400 system and Istra 4D software, Dantec Dynamics GmbH, Ulm, Germany) that is based on a pair of FireWire cameras (Stingray F-201b, Allied Vision Technologies GmbH, Stradtroda, Germany). The cameras have a sensor array size of 1624x1234 pixels, and can acquire images at a maximum rate of 30 frames per second at this resolution.

The cameras are controlled by a timing box with inputs to acquire external analogue voltage signals. The image acquisition is triggered by a pulse sent from the timing box to ensure that both images are captured at the same time.

3.1.2 High Speed DIC (HS-DIC)

Dantec Dynamics Q-450

This is a commercially available high speed DIC system (Q-450 system and Istra 4D software, Dantec Dynamics GmbH, Ulm, Germany) that is based on a pair of high speed cameras (Phantom v711, Vision Research, Wayne, NJ USA). The cameras used in this system have a sensor array size of 1280x800 pixels, and can acquire images at a maximum rate of 7530 frames per second at this resolution. Each camera has 32 gigabytes of memory, which permits approximately 4.5 seconds of recording time at the full resolution and the maximum framerate. The resolution can be reduced in order to achieve higher framerates and longer recording times. As is the standard practice for digital image correlation, the cameras are monochromatic and have an ISO sensitivity rating of 13,000.

The cameras are controlled by a timing box with inputs to acquire external analogue voltage signals. The image acquisition is triggered by a pulse sent from the timing box to ensure that both images are captured at the same time.

3.1.3 Pulsed laser

Litron Nano

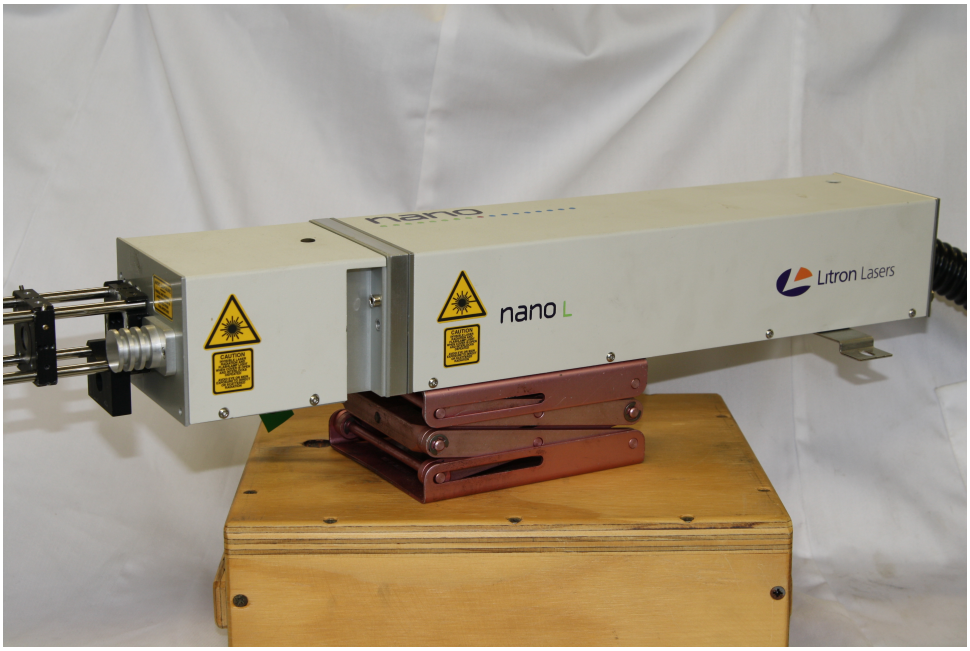

This is a commercially available laser (Nano L200-10, Litron, Rugby, England) that was modified by the manufacturer to produce an expanded beam with reduced speckle to be suitable for use with digital image correlation. The laser produces green light with a wavelength of 532 nm and a pulse duration of 4 nanoseconds. The laser is capable of a maximum power output of 200 millijoules at a repetition rate of 10 Hz. By using different lenses to expand the beam, it is possible to use the laser to illuminate an area up to 1 metre square.

3.1.4 Thermal camera

FLIR SC7650E

This is a commercially available thermal camera (SC7650E, FLIR, North Billerica, MA, USA) with sensitivity to wavelengths of 3-5 micrometers. The camera has a sensor array size of 640x512 pixels and is capable of recording images at a rate of 100 frames per second at this resolution. The resolution can be reduced to 320x256 pixels to achieve framerates over 300 fps. The typical sensitivity of the camera is 20 milliKelvin. To improve surface emissivity and reduce thermal reflections, it is desirable to coat the object of interest with a thin layer of flat black paint.

3.1.5 Laser Vibrometer

Polytec OFV-503 and OFV-2500

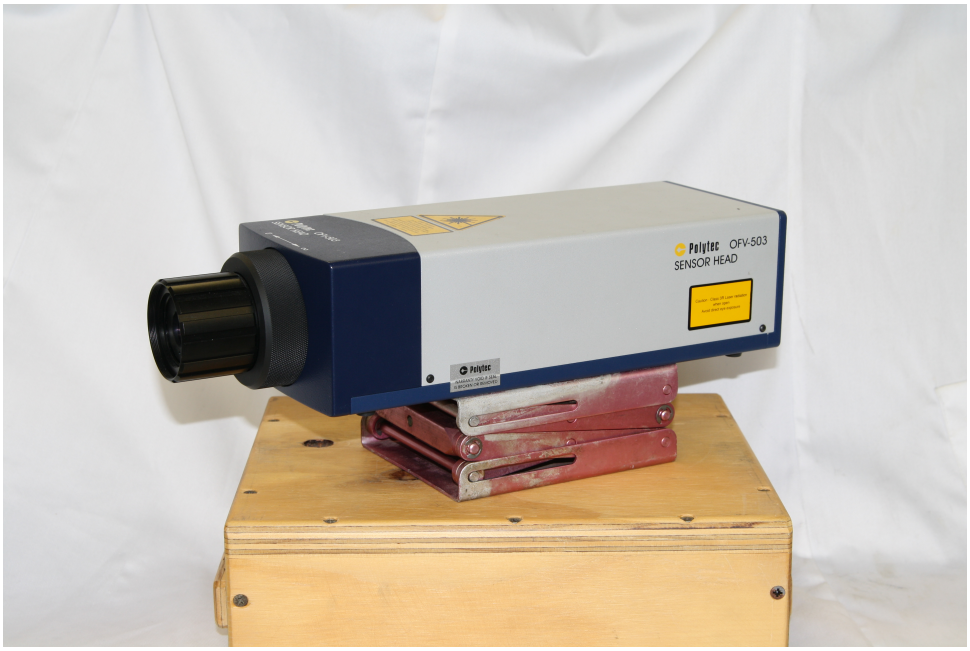

This is a commercially available laser Doppler vibrometer sensing head (OFV-503, Polytec GmbH, Waldbronn, Germany) and controller (OFV-2500, Polytec GmbH). The vibrometer uses the Doppler effect from a low-powered laser beam to calculate the surface velocity of a single point. As the vibrometer directly measures surface velocity, an integration card is used to output displacement. One of the major advantages of the laser vibrometer over other methods such as strain gauges and accelerometers is that it is non-contacting.

The setup of the laser vibrometer involves manually focusing the laser on the component to be measured. To achieve a high quality measurement, the surface should be fairly reflective. The vibrometer also has three different velocity measurement ranges, so the appropriate one must be selected based on the expected surface velocity to be encountered during the experiment.

3.1.6 Electrodynamic shaker and controller

DataPhysics V100/DSA1-1K

This is a commercially available shaker (V100, DataPhysics, San Jose, CA, USA) and 1 kW amplifier (DSA1-1K, DataPhysics) system. This system is capable of delivering a maximum sine force of 1,000 N and a random force of 533 N (RMS). Table 3.1 summarizes the capabilities of the shaker. For single frequency excitation, the shaker can be driven by a function generator. However, for more complex tests a vibration controller (ABAQUS, DataPhysics) is capable of applying random loading at a desired level by using feedback from force and acceleration transducers. The controller is also capable of playing back a previously recorded vibration trace, which allows experiments to be performed using real-life test data.

Table 3.1: Specifications of the shaker system.

	Maximum Force					
Shaker	**Sine**	**Random**	**Accel**	**Velocity**	**Travel**	**Mass**
V100/DSA1-1K	1000 N	533 N	100 g	1.65 m/s	12.7 mm	70 kg

3.2 Specimens

3.2.1 Aerospace panel

The panel was approximately 800 mm wide and 400 mm tall and milled from a solid piece of aluminium, resulting in a thin face sheet with some vertical stiffening ribs and mounting bosses on the back side. A detailed drawing of the panel can be found in Appendix A.1.

3.2.2 Hastelloy plates for high temperature

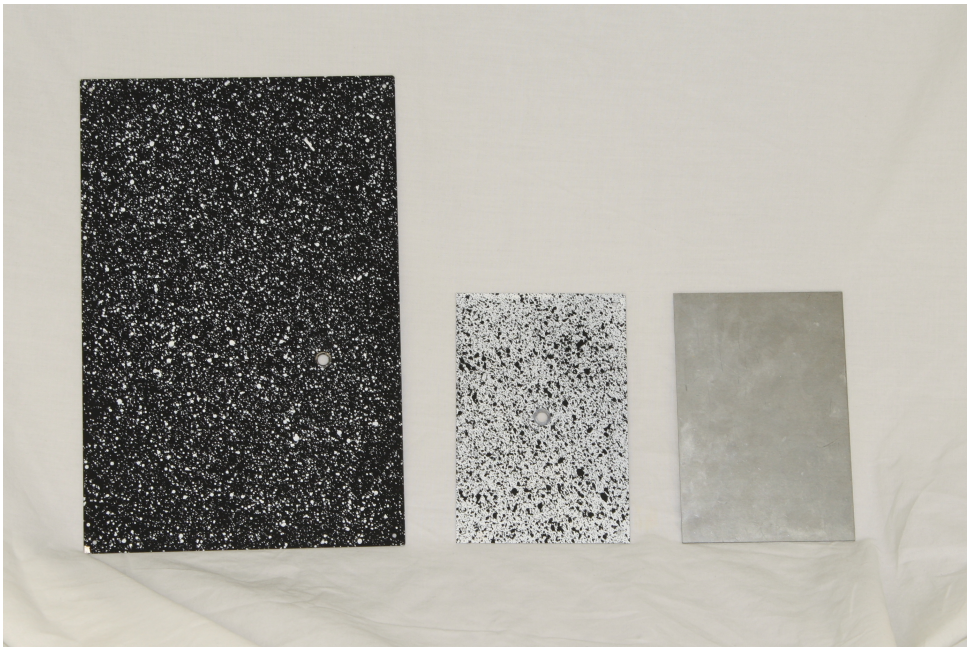

Figure 3.1: One of the large plates sprayed with a base coat of black paint and white speckle. The small plate in the middle has a base coat of white with a black speckle. The small plate on the right is un-painted.

Two different sizes of plate were used, both with a thickness of 0.040 in (1.016 mm) and a length to width ratio of 1.5:1. The smaller plate size was 120x80 mm, while the larger one was 219x146 mm. The plates were made from Hastelloy-X, a commercially available nickel-based alloy (Haynes International, Kokomo, IN USA).

3.3 Method

3.3.1 Digital Image Correlation

Digital image correlation is a non-contacting, full-field optical measurement technique. The method uses digital images of an object before and after deformation to calculate displacements. If a single camera is used in the measurement process, the in-plane displacements can be calculated. If a pair of cameras are used, it is possible to get both the in-plane and out-of-plane displacement of the surface of the object. The digital image is divided into subsets or facets, and these are compared from one image to the next. DIC is a multi-scale technique, with typical in plane accuracy on the order of 1/100 pixel.

Detailed information about the technique is provided by Sutton [91], Dally and Riley [92]. The following summarizes the basics of how digital image correlation works. An image is broken down into a series of subsets, usually square with a size of between 15x15 pixels and 50x50 pixels. A point from a subset in the reference image, $P(x, y)$, can be mapped to a point in a subset of the deformed image, $P^*(\tilde{x}, \tilde{y})$ using the following:

$$\begin{aligned} \tilde{x} &= x + u(x, y) \\ \tilde{y} &= y + v(x, y) \end{aligned} \tag{3.1}$$

where u and v are the displacement components that map $P^*(\tilde{x}, \tilde{y})$ to the reference point $P(x, y)$.

A shape function is used to approximate the deformation from equation 3.1 by using a Taylor series expansion about some point, $P(x_0, y_0)$. In the case of the software used in this thesis, the expansion is given by the following, which is a first order expansion

with an added second order term for distortion [93]:

$$\tilde{x} = x_0 + u_0 + \frac{\partial u}{\partial x}\Delta x + \frac{\partial u}{\partial y}\Delta y + \frac{\partial^2 u}{\partial x \partial y}\Delta x \Delta y$$
$$\tilde{y} = y_0 + v_0 + \frac{\partial v}{\partial x}\Delta x + \frac{\partial v}{\partial y}\Delta y + \frac{\partial^2 v}{\partial x \partial y}\Delta x \Delta y \tag{3.2}$$

These eight mapping parameters corresponding to displacements, slopes, and distortion are found by minimizing the differences in the subsets using a sum of squares deviation (SSD). Errors can occur in the matching process if the speckle pattern is not unique in the defined subset. Therefore subset size is important, as it must be large enough to capture a unique pattern, but small enough such that the shape function can accurately describe the deformation. This is known as the spatial resolution, which is the smallest physical size of the area that can be accurately measured and will represent an average of the deformation over that area, as approximated by equation 3.2.

In order to obtain sub-pixel accuracy in the subset matching process, interpolation of the discrete, grey level values measured by the camera is necessary. This was performed using a Bi-cubic spline, which involved the determination of 16 coefficients covering a 4x4 pixel area. According to Sutton, performing interpolation using less sophisticated filters, such as a cubic B-spline, can result in a bias of around 1/40 of a pixel, whereas an optimized 8 coefficient filter will have bias below 1/200 of a pixel [91]. The advantage of the less sophisticated filters is computational speed, however this comes at the price of increased bias.

In cases where it was desired to smooth the measured displacement data (for the calculation of strain, for example), a spline filter was applied. First, a reduced grid for the smoothing mesh was defined over the data set using a grid reduction factor. A higher grid reduction factor means a mesh with less points and the data will be smoothed over a larger gauge length. A 2D Bi-cubic spline function was then fitted to the data which

minimized a residual subjected to two constraints. The first constraint was to minimize the difference between the data and the mesh grid points. The second was to minimize the integral of the curvature of the spline. The integral was scaled by a smoothing parameter which determined the amount of smoothing.

Errors can also arise relating to the quality of the speckle pattern. As it can be seen that the measurement technique is reliant on the surface pattern, a high-quality pattern is necessary for good results. Reu has published some nice practical guides for producing a good speckle pattern [94, 95, 96, 97]. The speckle size is important, too small and there is a risk of aliasing, too large and a large subset is required which will reduce spatial resolution. The generally accepted optimal size is around 3-4 pixels in diameter.

An example of digital image correlation for a tensile test is shown in figure 3.2. The left side of the image shows a simple hole in a plate specimen painted with a random speckle pattern, before any loading has been applied. The right side is a mirror image of the specimen, after a tensile load has been applied. The red box defines an arbitrary subset of the surface, and shows how it has deformed from the original, unloaded condition. By tiling the surface with these subsets, it is possible to calculate a map of displacements over the entire field of view. The displacement map can then be differentiated to obtain strains.

3.3.2 Simulation capabilities

There were two primary analyses performed as a part of this thesis: real eigenvalue and frequency response [98]. An eigenvalue analysis without any damping or constraints applied was usually performed early in the development of an experiment to help determine the natural frequencies of vibration and mode shapes of the specimen. A commercial finite element software package was used both to mesh the geometry (HyperMesh 12.0,

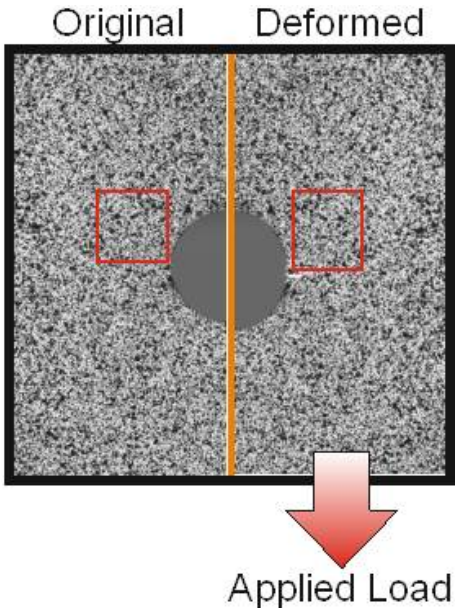

Figure 3.2: An example of how DIC calculates displacements by tracking the deformation of a subset of the pixels in an image.

Altair, Troy, MI USA) and perform the analysis (OptiStruct 12.0, Altair).

Real Eigenvalue Analysis

The natural frequencies and mode shapes are a function of the geometry, material properties, and boundary conditions of a structure. Therefore performing the analysis without any boundary conditions can be helpful in understanding how the structure will respond and determine excitation and measurement locations.

The eigenvalues were obtained using the Lanczos method (default for most solvers). The modes were normalised by the mass matrix.

Frequency Response Analysis

To calculate the structural response of the specimens to an applied excitation, a modal frequency response was performed. This type of analysis computes the overall response by summing the individual modal responses. The excitation can be applied in different ways, typically a force or a displacement is used. The output of the analysis is the displacements, velocities, and accelerations at each of the node locations.

Chapter 4

Assessment of Measurement Uncertainty

4.1 Introduction

As the use of Digital Image Correlation (DIC) has become more widespread, there has been much interest in recent years in determining the level of uncertainty in measurements made with a DIC system, as well as trying to identify sources of error which contribute to a measurement. This is especially critical for the acceptance of DIC in the industrial stress analysis community. The need for full-field optical techniques is greater than ever, as lighter-weight and more efficient structures are being developed, often based on computational models which may not be thoroughly validated.

Previous investigations of uncertainty in DIC have examined its limits from a theoretical or laboratory point of view and as such provide valuable insight into the capabilities of the technique in general. However, they do not provide information about the level of uncertainty obtained with a specific set-up used in a routine experiment. This chapter seeks to address this by providing a procedure to calibrate a DIC system by using a dynamic **Reference Material**[1] and assessing the overall measurement uncertainty, which could then be used in the validation of simulations of dynamic events such as projectile

[1]material, sufficiently homogeneous and stable with reference to specified properties, which has been established to be fit for its intended use in measurement or in examination of nominal properties [64]

impacts on vehicle panels [61].

First, it is appropriate to review the definition of **calibration** published in the International Vocabulary of Basic and General Terms in Metrology (VIM) [64]: *"operation that, under specified conditions, in a first step, establishes a relation between the quantity values with measurement uncertainties provided by measurement standards and corresponding indications with associated measurement uncertainties and, in a second step, uses this information to establish a relation for obtaining a measurement result from an indication."*

At this point a distinction should be made between the procedure performed during the setup of a DIC system in which the intrinsic and extrinsic parameters of the system are determined using a precision manufactured target, and procedures such as the ones developed by SPOTS, or the one presented here. The former procedure is typically referred to as 'calibration,' although it would be appropriate to give it a more specific name, such as intrinsic/extrinsic parameter calibration, or simply parameter calibration. Whereas the procedure presented here is a measurement calibration, i.e. calibration of the system regarding the measurement of displacement or strain.

Ultimately it is desired in the calibration process to relate the uncertainty of the system to some national standard through an unbroken chain of comparisons. This provides metrological **traceability.**[2] This chain of comparison is performed through the use of a specifically designed cantilever Reference Material.

A Reference Material has been designed based on a cantilever that produces a dynamic out-of-plane mode shape, $w(x, y)$, which can be predicted and is independent of the scale of the specimen. The cantilever design is simple, and the only critical dimension that must be measured during a dynamic calibration experiment is the amplitude

[2]the property of the result of a measurement whereby it can be related to appropriate measurement standards, generally international or national standards, through an unbroken chain of comparisons [64]

of the displacement of the tip. For the results presented here, the amplitude of vibration of the cantilever was measured using a calibrated displacement transducer (laser Doppler vibrometer). By using a calibrated displacement transducer, traceability has been established to the national standard for length, the meter.

The end result of performing the process is to produce a minimum measurement uncertainty for a particular experimental setup. As the underlying principle of digital image correlation is very complicated, with many potential error sources, this provides a way to assess a particular setup taking the entire procedure into account, from the setup, to the parameter calibration, to the actual measurement, to the post-processing. It should be noted that this is idealized process that may not capture the intricacies of the planned experiment, but that is why it is called a minimum measurement uncertainty. By definition it is impossible to capture all sources contributing to the uncertainty of a measurement, but the key is to capture what is believed to be the important ones.

The first three bending modes of the cantilever Reference Material were measured using a pair of high-speed cameras. This covered a frequency range of 126-2123 Hz and a measured peak-to-peak amplitude of displacement of 30-600 μm. Statistical analysis is used to evaluate both the random and systematic components of error contributing to the measurement uncertainty. In order to visualize the results of the calibration, a plot was produced at each frequency comparing the difference between the measured and predicted values of the out-of-plane displacement of the Reference Material and the uncertainty associated with the Reference Material.

4.2 RM Design and analytical description

4.2.1 Design and manufacture

The Reference Material used for this measurement calibration was a fixed-free cantilever. Some results have been recently published for the calibration of an ESPI system using a flat plate Reference Material by Davighi *et al.* [99]. However, the cantilever design was preferred over the flat plate design for several reasons, including ease of manufacture and the capability to be used for both static and dynamic measurements. The cantilever Reference Material was designed to be scalable, so all of the dimensions are expressed as a function of T, the cantilever thickness. These dimensions are given in figure 4.1.

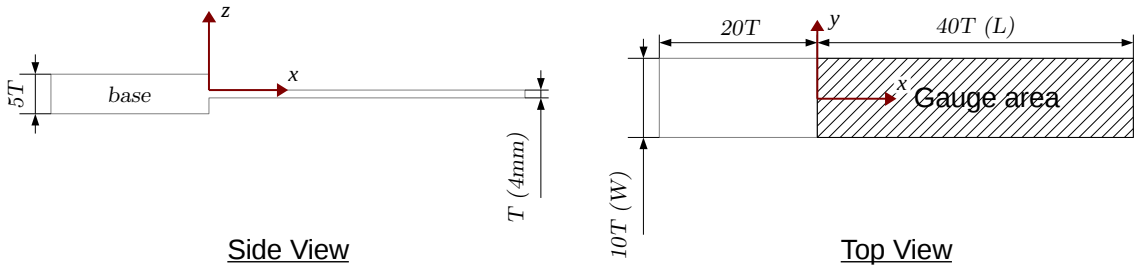

Figure 4.1: Drawing of the cantilever Reference Material showing the normalized dimensions of the specimen used as well as the gauge area that was imaged with the DIC system.

The Reference Material is designed with a thick base section, which is intended to be securely clamped while excitation is applied to the cantilever. The entire surface of one side of the cantilever was measured with the optical instrument. This is shown as the Gauge Area in figure 4.1. The cantilever was manufactured using a computer controlled milling machine from a single piece of 2024 aluminum. The manufacture of the cantilever was relatively straightforward; however, care was taken to ensure that the surfaces were parallel and that the cantilever was straight. The geometry of the Reference Material was measured using a series of independent observations in order to establish its uncertainty [100]. For the thickness (T) and width (W) parameters measurements were

made at three locations along the length of the beam. For the length (L) parameter, the measurement was made at the centerline. A total of six replications was performed for each measurement. The values for the dimensions of the specimen and their associated uncertainty are listed in table 4.1.

Table 4.1: The critical dimensions of the cantilever Reference Material and their associated uncertainties.

Parameter	Units	Value	Uncertainty, u
T	mm	3.98	0.008
L	mm	160.01	0.012
W	mm	40.00	0.014
M	g	251.6	0.01

4.2.2 Natural frequencies and deformation field equations

For the dynamic excitation, the theoretical natural frequencies of vibration of the cantilever were found from the following equation [101]

$$f_k^T = \frac{\lambda_k^2}{2\pi L^2}\left(\frac{EIL}{M}\right)^{1/2} \tag{4.1}$$

where E is the modulus of elasticity, I is the second moment of area, and M is the mass of the cantilever. The second moment of area is defined as $I = WT^3/12$ which for the Reference Material simplifies to $I = 5T^4/6$.

The first three dimensionless natural frequency parameters, λ_k are: $\lambda_1 = 1.875$, $\lambda_2 = 4.694$ and $\lambda_3 = 7.855$. For $k > 3$ they are given by the following relation

$$\lambda_k = (2k-1)\frac{\pi}{2} \tag{4.2}$$

The modal shape of the cantilever in bending mode k is given by [101]

$$w_k(\xi) = \frac{\delta}{2}[\cosh \lambda_k(1-\xi) + \cos \lambda_k(1-\xi) - \phi_k(\sinh \lambda_k(1-\xi) + \sin \lambda_k(1-\xi))] \quad (4.3)$$

where w is the out-of-plane displacement of the cantilever in the z-direction and is a function of $\xi = x/L$. The modal shape is proportional to the measured tip amplitude δ in the z-direction, and ϕ_k is given by

$$\phi_k = \frac{\sinh \lambda_k - \sin \lambda_k}{\cosh \lambda_k + \cos \lambda_k} \quad (4.4)$$

the first three values of which are $\phi_1 = 0.7340$, $\phi_2 = 1.0185$, and $\phi_3 = 0.9992$.

4.3 Experimental procedure

4.3.1 Apparatus

A commercial high-speed, 3-D DIC system (Q-450, Dantec Dynamics, Ulm, Germany) based on a pair of high-speed cameras (Phantom v711, Vision Research) was calibrated. These cameras have a maximum frame rate of 7500 frames per second (fps) at the full resolution of 1280x800 pixels. For the measurements presented here, the vertical resolution was reduced from 800 to 500 pixels to allow a higher frame rate. A matched pair of 100 mm focal length lenses were used (Makro Planar 2/100 ZF-I, Zeiss) with the aperture stop set to $f11.0$. This setup resulted in an image magnification of 7.2 pixels/mm.

A 1000 Watt light specifically designed for high-speed imaging was used for illumination (AT-Stautz Tecknik GmbH, Balingen, Germany). This permitted an exposure time of 40 microseconds to be used for all of the measurements. As a worst case scenario, the amount of movement that occurred during the 40 microsecond exposure was calculated

for the first mode of vibration of the cantilever (126 Hz). It was found to be 9.4 microns which translates into 0.06 pixels. Although this is higher than the desired 0.01 sub-pixel accuracy of the DIC technique, the actual measurements of the vibrating cantilever were performed at the point of maximum deflection in the vibration cycle. At this point the velocity would actually be zero, and so there would be no motion blurring in the images. The cameras were located 720 mm apart at a distance of 780 mm from the surface of the Reference Material. For the first natural frequency (127Hz) 100 pairs of images were captured at 5000fps. For each of the second and third natural frequencies (796Hz and 2123Hz), 100 pairs of images were captured at 11,000 fps.

To determine the intrinsic and extrinsic values of the experimental setup, a parameter calibration was performed by capturing a series of 15 images of a specially made target. The target was supplied with the 3-D DIC system and consisted of a 9 by 9 checkerboard-like pattern of light and dark squares. Each checkerboard square was 20 mm, so the total size of the target was 180 mm by 180 mm. The software produced an uncertainty for each measurement point based on the results of the calibration, which is described in more detail by Becker *et al.* [72]. This uncertainty was on the order of 0.5-1.0 microns for all of the measurements presented here.

4.3.2 Excitation and displacement measurement

A non-contacting method of excitation, such as a loudspeaker was thought to be preferable because it would not induce any rigid body displacements in the cantilever. The initial experiments were performed in this fashion with the cantilever clamped in a vice that was bolted to an optical table. The excitation was provided with a powered subwoofer (Yamaha YST-FSW050) which was placed behind the cantilever, so as to not obstruct the view from the cameras. The subwoofer was driven using the sinewave output from a

function generator (GW Instek GFG-8216A). The setup can be seen in figure 4.2.

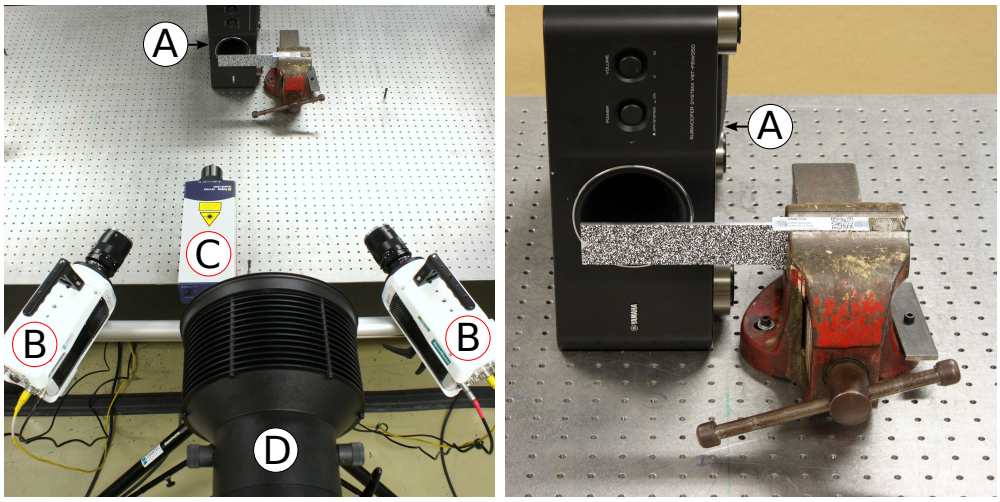

Figure 4.2: The experimental setup using the non-contacting loudspeaker for excitation (A). The image on the left gives an overall view of the setup showing the cameras (B), laser vibrometer (C) and light source (D). The image on the right is a close-up of the cantilever mounted in the vice.

A laser Doppler vibrometer (OFV-2500 controller and OFV-503 head, Polytec GmbH, Waldbronn, Germany) was used to measure the displacement of the tip, δ, of the cantilever at each of the first three natural frequencies. The acoustic excitation produced a maximum amplitude of vibration of the first mode of 600 μm, but only a few microns at the second and third modes. For the second and third modes the amplitude was not large enough to be measured with the experimental setup. This could have been due in part to the loudspeaker, which was designed for frequencies below 500Hz. So a mount was made to attach the cantilever directly to a shaker (GW-V100, DataPhysics, San Jose, CA USA), which is shown in figure 4.3. This produced much larger amplitudes of vibration but introduced a degree of freedom to the base that needed to be taken into account.

For the first mode, the amplitude of vibration of the base was of the order of 20% of the tip amplitude; whereas for the second and third modes it was less than 1 μm. So a hybrid approach was taken with the calibration, using acoustic excitation for the first mode, and the shaker for the second and third modes.

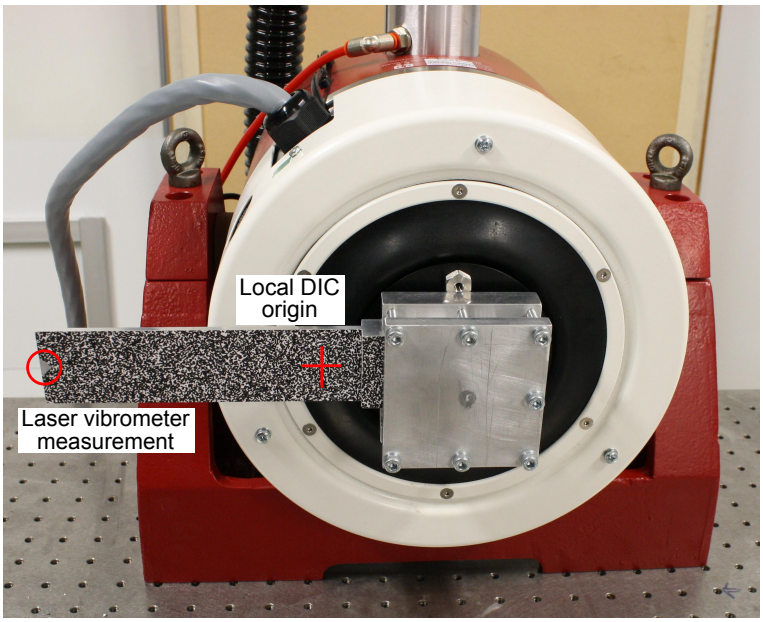

Figure 4.3: Close up showing the 160mm x 40mm area of the cantilever Reference Material mounted to the shaker. This excitation method was used for the second and third modes.

A synthetic speckle pattern was generated and printed on paper. Spray adhesive was then used to attach the paper to the cantilever. It was decided to print the pattern as opposed to using paint because the size of the speckle can be precisely controlled. Advice provided by Sutton *et al.* was used as a guide for the size of the speckle appropriate for the spatial resolution [102]. This resulted in a pattern with a speckle size of 0.5 mm (approximately 3-4 pixels).

It was necessary to have local coordinates for the measured DIC data and for the location of the measurement with the laser Doppler vibrometer. A small area of the speckle pattern was removed at the tip of the cantilever, revealing the reflective metal surface to enable a more reliable measurement with the laser vibrometer. A caliper was used to lightly score the surface of the cantilever along the centerline at a point 3 mm from the tip, to provide a target for the vibrometer. This meant that the location of the tip measurement could be related to the tip of Reference Material when post-processing the measurement data.

A similar procedure was used to provide an origin for the local coordinate system of

the DIC data. A faint mark was also made on the surface of the speckle pattern with a pencil along the centerline and at a 20 mm offset from the root of the cantilever. The reason the root of the cantilever was not used as the origin in the DIC is because the processed data did not contain information which went all of the way to the edges of Reference Material, so a point within the measured space had to be used. The location of the laser vibrometer measurement and the local origin for the DIC data can be seen in 4.3.

The cameras were set up so that section L of the Reference Material (see 4.1) occupied more than 80% of the longer dimension of the sensor of the camera. To accomplish this the cantilever was mounted in a horizontal position. The excitation signal for the measurement was produced by the function generator, and sent to either the loudspeaker (first mode), or the shaker (second and third modes). The amplitude of the vibration was set by examining the displacement output from the laser vibrometer directly on an oscilloscope.

Once the frequency and amplitude were set, a series of images was captured using the DIC software. The timing box of the system was used to record the displacement signal from the laser vibrometer during the image capture, thus providing the exact measurement from the vibrometer corresponding to the DIC measurements.

4.4 Results

After setting up the experiment but prior to applying vibration loading to the cantilever, a series of images was captured to assess the noise in the processed displacements. This was performed with the cantilever securely clamped in place such that no motion would occur during the acquisition process. The resulting images were processed using the commercial 3-D DIC code supplied with the system (Istra4D, Dantec Dynamics, Ulm, Germany). The

facet (or subset) size was set at 29 pixels, which was the smallest size containing enough information to allow correlation of the images, based on the recommendations provided by Sutton *et al.* [102]. The offset of the facets was set to 15 pixels which gave an overlap of approximately 50%. The coordinate system was defined by using the crosshair lightly drawn on the surface of the speckle as the origin.

Displacement smoothing was applied to the data using a spline with a grid reduction factor of 2 and a smoothness factor of -1. The full-field displacement results were imported into MATLAB using the hdf5 file format to calculate the standard deviation of the calculated displacements. This was found to be 0.8 microns (< 0.001 pixels) for the resultant (total) displacement component.

Data was captured for several periods of oscillation of the vibrating cantilever with the high-speed cameras. Images of the maximum and minimum deflection were obtained by plotting the signal from the laser vibrometer and selecting the images that corresponded to peak displacement. For visualization purposes, plots were produced to compare the calculated modal shape to the modal shape measure with the DIC system. These are shown in Figures 4.4, 4.6, and 4.8.

Statistical analysis of the data was performed to determine the measurement uncertainty, and assess the systematic and random error components [103]. A difference field, or field of deviations, (d_k) was calculated by comparing the measured values (w_k^E) from the experiment to the predicted values (w_k^T) from theory for each frequency, k, i.e.

$$d_k(i,j) = w_k^T(x_i, y_j) - w_k^E(x_i, y_j) \tag{4.5}$$

and represents the error (both bias and random) of the measurement.

The systematic component of the error can be expressed by two fit parameters, α and β. A linear least-squares fit was applied to the field of deviations to obtain the values for

the two fit parameters by minimizing the following residual

$$\sum_{i,j}\Big[d_k(i,j)-\alpha_k-\beta_k w_k^T(x_i,y_j)\Big]^2 \tag{4.6}$$

where

$$\alpha_k=\frac{\sum_{i,j}(w_k^T)^2(x_i,y_j)\sum_{i,j}d_k(i,j)-\sum_{i,j}w_k^T(x_i,y_j)\sum_{i,j}w_k^T(x_i,y_j)d_k(i,j)}{N\sum_{i,j}(w_k^T)^2(x_i,y_j)-\Big(\sum_{i,j}w_k^T(x_i,y_j)\Big)^2} \tag{4.7}$$

and

$$\beta_k=\frac{N\sum_{i,j}w_k^T(x_i,y_j)d_k(i,j)-\sum_{i,j}w_k^T(x_i,y_j)\sum_{i,j}d_k(i,j)}{N\sum_{i,j}(w_k^T)^2(x_i,y_j)-\Big(\sum_{i,j}w_k^T(x_i,y_j)\Big)^2} \tag{4.8}$$

The values of α and β along with their associated uncertainty are shown in table 4.2.

This residual is subject to w^T, so it is a function of the predicted values. Plotting these values over the same coordinate range of w^T and w^E will create a surface in which α describes the offset and β describes the slope. The field of deviations, $d_k(i,j)$, along with $\alpha_k+\beta_k w_k^T$ was plotted for each frequency, k and these are shown in figures 4.5, 4.7, and 4.9, which are all plotted on the same scale for comparison purposes.

The mean square residual deviation, $u^2(d_k)$ was found from

$$u^2(d_k)=\frac{1}{N}\sum_{i,j}[d_k(i,j)]^2-\alpha_k^2-2\alpha_k\beta_k\frac{1}{N}\sum_{i,j}w_k^T(x_i,y_j)-\beta_k^2\frac{1}{N}\sum_{i,j}(w_k^T)^2(x_i,y_j) \tag{4.9}$$

and used to calculate the uncertainties of the fit parameters $u(\alpha_k)$ and $u(\beta_k)$

$$u(\alpha_k)=u^2(d_k)\left[\frac{\sum_{i,j}(w^T)^2(x_i,y_j)}{N\sum_{i,j}(w_k^T)^2(x_i,y_j)-\Big(\sum_{i,j}w_k^T(x_i,y_j)\Big)^2}\right]^{1/2} \tag{4.10}$$

$$u(\beta_k) = u^2(d_k) \left[\frac{1}{N \sum_{i,j} (w_k^T)^2(x_i, y_j) - \left(\sum_{i,j} w_k^T(x_i, y_j) \right)^2} \right]^{1/2} \tag{4.11}$$

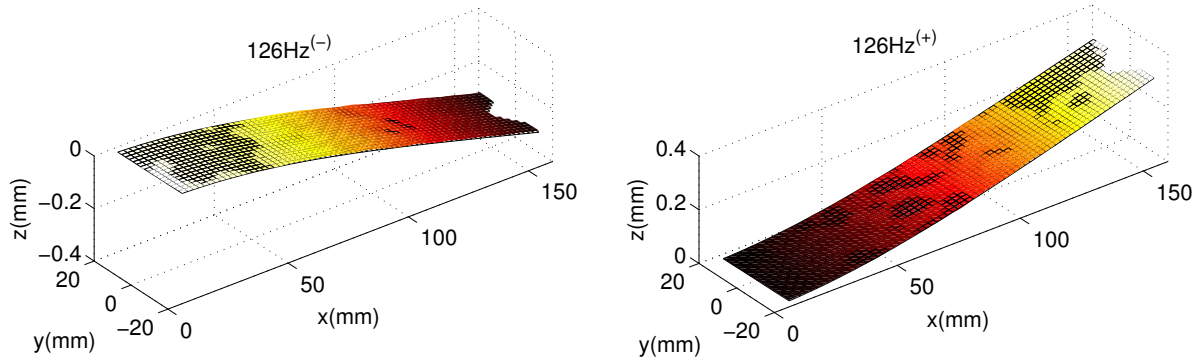

Figure 4.4: The predicted out-of-plane displacement from theory, $w^T(x_i, y_j)$, (mesh surface) and the measured values from experiment, $w^E(x_i, y_j)$, (solid surface) for the 1^{st} mode of the cantilever at the two extrema of deflection.

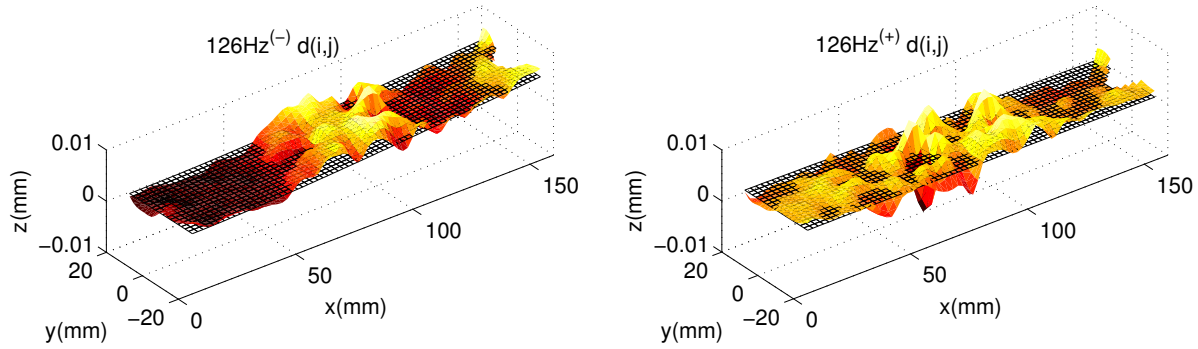

Figure 4.5: The solid surface is the field of deviations, $d(i, j)$, and the mesh surface is given by $\alpha + \beta w^T$ for the measurement shown in figure 4.4.

There were several sources of uncertainty in the dynamic calibration which have been identified and contribute to the uncertainty in the modal shape, $u(w_k)$. These uncertainties are all proportional to the tip deflection, δ and are expressed in reduced coordinates, $\xi = x/L$ for convenience.

First, there is the uncertainty in the geometry, which is a result of the manufacturing process and the capability of the tools used to measure the geometry, and will give un-

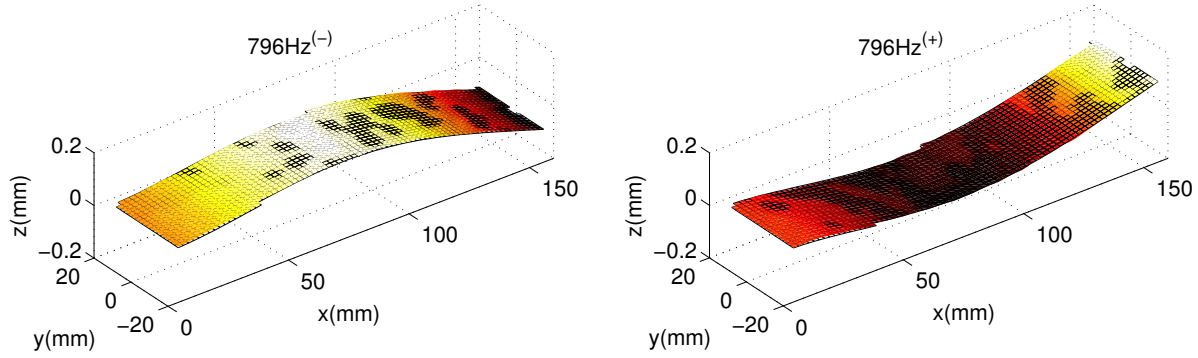

Figure 4.6: The predicted out-of-plane displacement from theory, $w^T(x_i, y_j)$, (mesh surface) and the measured values from experiment, $w^E(x_i, y_j)$, (solid surface) for the 2^{nd} mode of the cantilever at the two extrema of deflection.

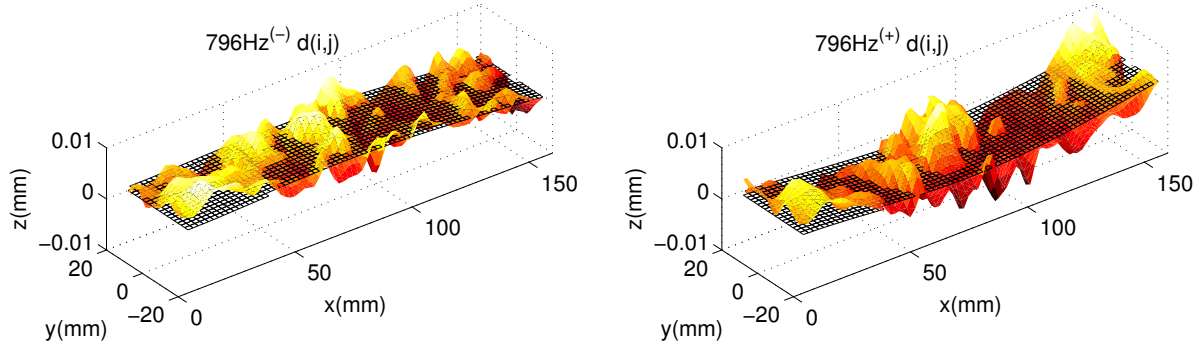

Figure 4.7: The solid surface is the field of deviations, $d(i, j)$, and the mesh surface is given by $\alpha + \beta w^T$ for the measurement shown in figure 4.6

certainty values for T and L. While these values would be critical for a static calibration, they do not appear in the expression for the modal shape of the cantilever equation (4.3) and so are not a factor in this case.

The second source is from the identification of homologous points from the Reference Material surface and the measurement grid. A reasonable estimate for this uncertainty was taken as one pixel on the sensor, or $u(\xi) = 1/K$, where K is the number of pixels that image the length L of the cantilever. For these measurements, $K = 1130$, meaning that 1130 of the sensor's 1280 pixels were used to image the length of the cantilever. This

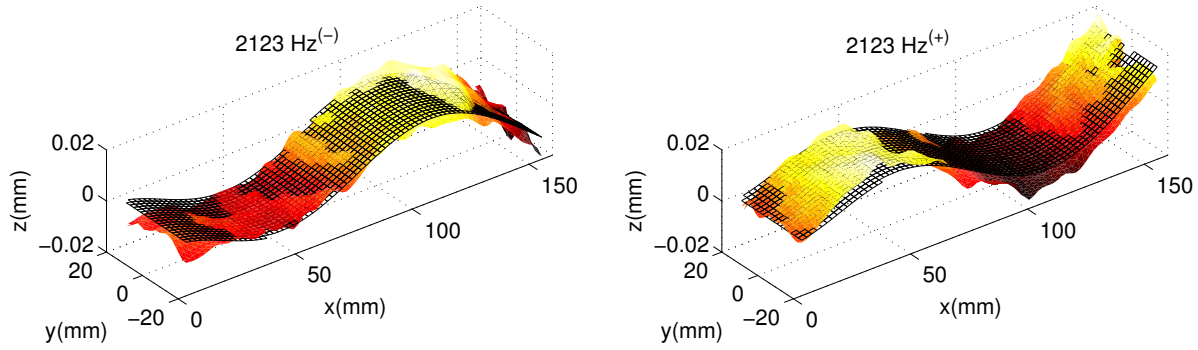

Figure 4.8: The predicted out-of-plane displacement from theory, $w^T(x_i, y_j)$, (mesh surface) and the measured values from experiment, $w^E(x_i, y_j)$, (solid surface) for the 3^{rd} mode of the cantilever at the two extrema of deflection.

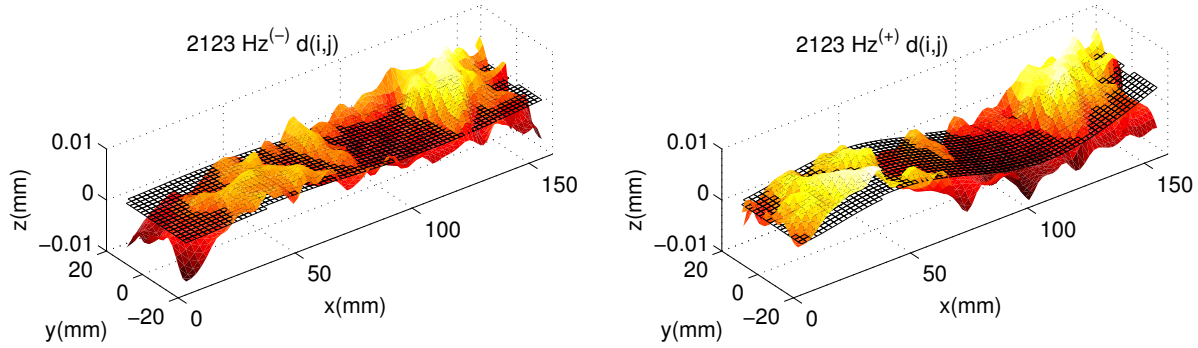

Figure 4.9: The solid surface is the field of deviations, $d(i, j)$, and the mesh surface is given by $\alpha + \beta w^T$ for the measurement shown in figure 4.8.

gives a value of $u(\xi)$ of approximately 1 micron.

The final source of uncertainty comes from the tip deflection measurement. This is a combination of the calibration uncertainty of the measurement transducer $u_{\text{cal}}(transducer)$ and the relative positioning uncertainty $u(\xi)$, i.e.

$$\frac{u^2(\delta)}{\delta^2} = \frac{u^2_{\text{cal}}(transducer)}{\delta^2} + (\lambda_k \phi_k)^2 u^2(\xi) \tag{4.12}$$

The calibration uncertainty of the laser vibrometer was provided by the manufacturer,

and was 1 micron over the measurement range investigated.

The combination of all of the above components of uncertainty can be combined to produce the total uncertainty in the modal shape, $u(w_k)$, as

$$\begin{aligned} u^2(w_k) &= \frac{u^2(\delta)}{\delta^2} w_k^2 + u^2(\xi) \left(\frac{\delta}{2}\lambda_k\right)^2 [\sinh \lambda_k(1-\xi) - \sinh \lambda_k(1-\xi) \\ &\quad -\phi_k(\cosh \lambda_k(1-\xi) + \cos \lambda_k(1-\xi))]^2 \end{aligned} \tag{4.13}$$

This is accomplished by employing the law of propagation of uncertainty based the Root Sum of Squares (RSS) method from equation (4.3) and using the procedure identified in [100].

To assess the calibration of the system, plots were produced which compared the field of deviations to the uncertainty in the modal shape as shown in figures 4.10, 4.11, and 4.12. A pair of dashed lines were plotted using the fit parameters (α_k and β_k) plus/minus their expanded uncertainty, i.e. $\alpha + \beta w_k^T \pm 2u(d_k)$. The uncertainty of the modal shape, $\pm 2u(w_k)$ was plotted with a pair of solid lines. In this case, the dashed lines plotted from the fit parameters form two parallel lines, while the uncertainty of the modal shape increases as a function of the applied displacement.

The uncertainty (vertical axis) of all three sets of plots is set to the same scale to allow comparison between the different frequencies. It was considered that when the scatter band on the measurements, represented by $\alpha + \beta w_k^T \pm 2u(d_k)$ did not overlap the area bounded by the uncertainty in the Reference Material mode shape, $\pm 2u(w_k)$, then there was a significant deviation and a satisfactory calibration had not been achieved. This does not occur in any of the cases shown in figures 4.10, 4.11, or 4.12, and so it was considered that the measurement values, w_k^E coincide with the predicted values, w_k^T and $d_k(i,j)$ contained only random errors or noise.

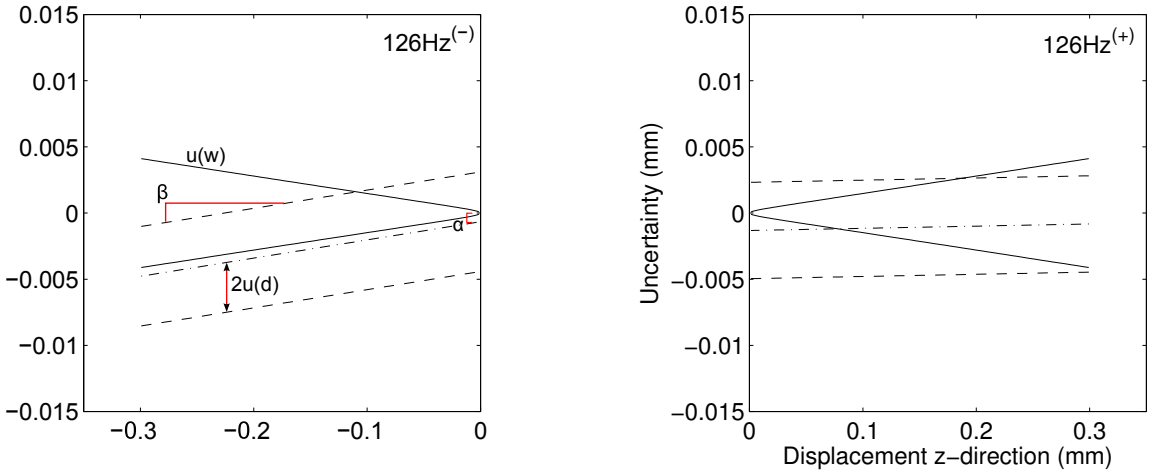

Figure 4.10: The assessment plots produced based on the measurement shown in figure 4.4. The solid line represents the uncertainty in the modal shape, $\pm 2u(w)$, and the dashed line represents the uncertainty in the field of deviations, $(\alpha + \beta w^T) \pm 2u(d)$.

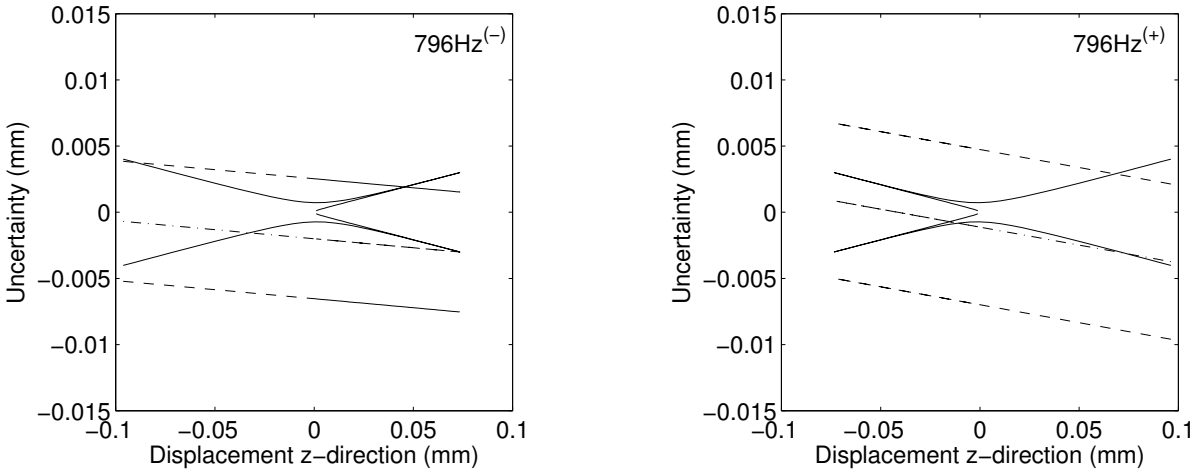

Figure 4.11: The assessment plots produced based on the measurement shown in figure 4.6. The solid line represents the uncertainty in the modal shape, $\pm 2u(w)$, and the dashed line represents the uncertainty in the field of deviations, $(\alpha + \beta w^T) \pm 2u(d)$.

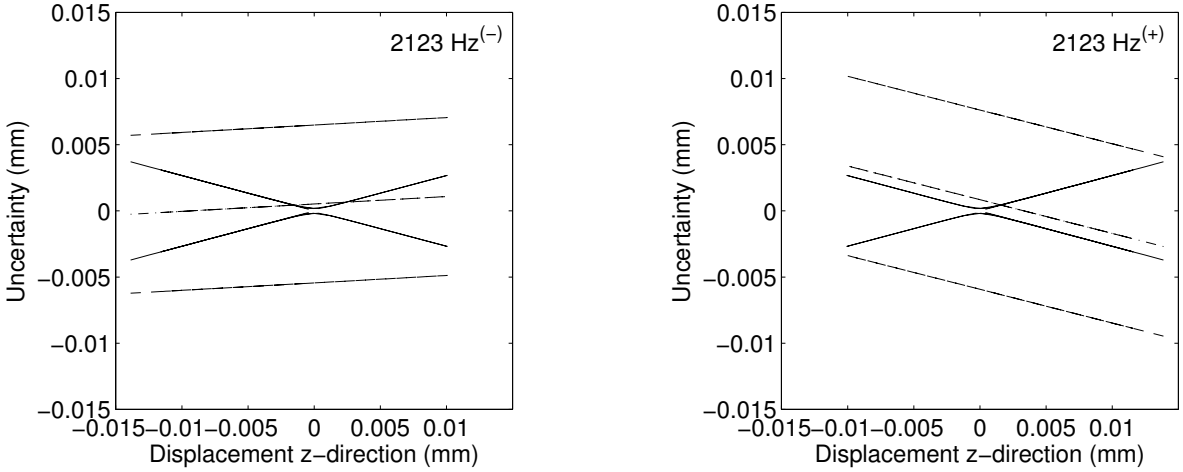

Figure 4.12: The assessment plots produced based on the measurement shown in figure 4.8. The solid line represents the uncertainty in the modal shape, $\pm 2u(w)$, and the dashed line represents the uncertainty in the field of deviations, $(\alpha + \beta w^T) \pm 2u(d)$.

4.5 Discussion

The objective of this chapter was to establish the level of uncertainty associated with this particular set-up for the purposes of dynamic measurements. The random measurement error was found from the field of deviations and is given by $u(d_k)$. The uncertainty from the modal shape, $u(w_k)$ is a combination of the uncertainty from the laser vibrometer and uncertainty arising from the identification of points on the surface of the Reference Material. These two quantities can be combined to determine the total uncertainty for the measurement, $u_{\text{cal}}(w_k)$ given by

$$u_{\text{cal}}(w_k) = \left[u^2(d_k) + \max(u^2(w_k))\right]^{1/2} \tag{4.14}$$

This can conveniently be expressed as a percentage of the amplitude of vibration, to produce a relative uncertainty. This data is summarized in table 4.3.

The values for $u(w_k)$ do not change much, from 2.1 microns at the first mode to 1.9 microns at the third. This is to be expected though, as equation (4.13) is primarily a function of the tip displacement. There is a more significant difference in $u(d_k)$, although

Table 4.2: The fit parameters α and β along with their uncertainty values calculated from the field of deviations for each load step.

	α_k μm	$u(\alpha_k)$ μm	β_k μm	$u(\beta_k)$ μm
$1^{st} : 126Hz^{(-)}$	-0.7	0.09	13.8	0.02
$1^{st} : 126Hz^{(+)}$	-1.3	0.09	1.7	0.02
$2^{nd} : 796Hz^{(-)}$	-2.0	0.07	-13.7	0.03
$2^{nd} : 796Hz^{(+)}$	-1.1	0.09	-27.1	0.05
$3^{rd} : 2123Hz^{(-)}$	0.5	0.08	56.1	0.28
$3^{rd} : 2123Hz^{(+)}$	0.8	0.09	-254.9	0.32

Table 4.3: Summary of the calibration uncertainty results for each of the three frequencies. N is the total number of experimental data points produced. $u(d_k)$ is the uncertainty from the residuals. $u(w_k)$ is the uncertainty from the cantilever reference material. $u_{\text{cal}}(w_k)$ is the combined uncertainty, and the last column on the right is the percent uncertainty relative to the amplitude of displacement for that frequency.

	N	$u(d_k)$ μm	$u(w_k)$ μm	$u_{\text{cal}}(w_k)$ μm	Amplitude μm	Relative %
$1^{st} : 126Hz^{(-)}$	1258	1.9	2.1	2.8	600	0.5%
$1^{st} : 126Hz^{(+)}$	1258	1.8	2.1	2.7	600	0.5%
$2^{nd} : 796Hz^{(-)}$	1422	2.3	2.0	3.0	200	1.5%
$2^{nd} : 796Hz^{(+)}$	1422	2.9	2.0	3.5	200	1.8%
$3^{rd} : 2123Hz^{(-)}$	1422	3.0	1.9	3.6	30	12.0%
$3^{rd} : 2123Hz^{(+)}$	1422	3.4	1.9	3.9	30	13.0%

it still only varies from 1.8-3.4 microns across all three modes. The values increase with the increase in the mode shape, which could be attributed to a couple of things. The first mode is a relatively simple bending shape, so displacement gradient is quite simple and smooth and so one could expect this to yield the best results. As the modal number is increased, the complexity of the shape increases resulting in steeper displacement gradients. The amplitude of the measurement (600 microns) was also much larger than the second (200 microns) or third (30 microns) modes.

The combined measurement uncertainty, u_{cal}, similarly varies from 2.7 microns to 3.9 microns, resulting in relative uncertainties ranging from 0.5% to 13.0%. As was

mentioned previously, the noise calculated from the static measurements was 0.8 microns, so the combined uncertainty is larger, which is to be expected from a realistic laboratory measurement. It can be seen that the amplitude of the measurement range will have a large impact on the relative uncertainty, which is why the first mode has such a low value and the third mode, with only 30 microns of displacement, had an uncertainty of 13.0%. Had it been possible to obtain a larger amplitude of vibration at the third mode, one would expect that the relative uncertainty would be on the order of a few percent.

Figures 4.10–4.12 provide a way to visualize the data from both tables 4.2 and 4.3. Figure 4.10 shows the results for the first natural frequency of vibration, along with labels on the plot to help relate it to the information in the tables. The uncertainty from the calculation of the modal shape, $u(w_k)$, is shown by the solid lines. The uncertainty is at a maximum at the maximum of measured z-displacement, and approaches zero as the measured displacement decreases. The random error is given by $u(d_k)$, which is indicated by the dashed lines. The offset of the dashed lines from the origin is described by α and the slope by β, and these components together represent the systematic error component. Ideally the dashed lines would be perfectly horizontal ($\beta = 0$) and symmetric about the origin ($\alpha = 0$), but in a real measurement system there will be deviations. These plots provide a way to visualize the measurement error components and determine if they are significant relative to the uncertainty from the modal shape calculation.

Figure 4.11 shows the results for the second natural frequency of vibration. The bands representing the fit parameters and their expanded uncertainty is slightly wider for this frequency than for the first frequency, indicating that there was more variation in the experimental data. A complete overlap is achieved between the two sets of lines, so a satisfactory calibration has also been achieved at the second natural frequency.

Figure 4.12 shows the results for the third natural frequency of vibration. The bands

representing the fit parameters and their expanded uncertainty are the widest for this step. This indicates a larger deviation between the measured values and the predicted values at this natural frequency as compared to the first two. However, there is still complete overlap between the two sets of lines, so a satisfactory calibration has been achieved at the third frequency as well.

These values give a minimum measurement uncertainty for a particular setup over the frequency and displacement range used in the measurement calibration. When measurements are to be made over a different frequency range or amplitude of displacement, then an appropriate Reference Material should be obtained and the calibration procedure repeated.

4.6 Conclusions

This chapter has presented the first results obtained from a dynamic calibration of a high-speed 3-D digital image correlation system. A simple cantilever Reference Material with a gauge area of 160mm x 40mm, manufactured from 2024 aluminium was used in the measurement calibration. The system was shown to achieve an acceptable calibration over a frequency range of 130-2100Hz and an out-of-plane displacement amplitude range of 30-600 microns. The calibration uncertainty was found to vary from 2 to 4 microns over the frequency range, however the amplitude of vibration decreased with increasing frequency so the relative uncertainty ranged from 0.5% at the first natural frequency through 1.8% at the second natural frequency to 13% at the third natural frequency.

Initially it was found that acoustic excitation was unable to provide enough energy to produce deflections that could be measured by the system at the second and third natural frequencies. A hybrid approach was taken in which acoustic excitation was used for the first mode and a shaker for the second and third modes. The scatter in the measured out-

of-plane displacement was compared to the uncertainty associated with the modal shape of the Reference Material in order to assess whether there were any significant deviations. In the three modes examined there were no such deviations and so the calibration was considered acceptable.

Chapter 5

Application of PL-DIC for Vibration Measurement

5.1 Introduction

This chapter describes the development of the Pulsed Laser Digital Image Correlation (PL-DIC) system. This is a novel system in which a pulsed laser is used along with a pair of standard machine vision cameras to capture the in-plane and out-of-plane components of displacement of a vibrating component. It was desired to develop a system which used standard machine vision cameras rather than high speed cameras due primarily to the lower cost and smaller size. In addition, high speed cameras are not currently available which operate in the UV spectrum, which has been identified as a potential solution to performing high temperature DIC. Table 5.1 summarizes the differences between a high-speed system and the PL-DIC system.

The capture of images without the use of high speed cameras is typically achieved through the use of stroboscopic illumination. The pulsed laser provides a very bright, uniform light with a short pulse duration, which is perfect for capturing moving objects. By synchronising the laser pulses with the vibration excitation it is possible to capture the vibration of an object excited at resonance at any point in the cycle of vibration.

The PL-DIC system has been further extended to capture data on a component excited by a random (unknown) signal by using a laser vibrometer. This new technique uses the

High Speed Cameras	Pulsed-Laser DIC
• Pros – Measure dynamic events – Frequency info from random or broadband excitation • Cons – Expensive – Synchronization errors – Resolution/speed compromise – Possible heat from (constant) illumination	• Pros – High resolution produces high quality data – Relatively inexpensive – No synchronization errors – Very short pulse duration – Little heating of specimen • Cons – Moderate speed (10s of hertz) – Laser safety issues (Class IV)

Table 5.1: Comparison of digital image correlation systems based on high speed cameras and the system with standard cameras and the pulsed laser.

fast measurement capability of the laser vibrometer to monitor the panel and trigger the image acquisition with the pulsed laser.

An assessment of the pulsed laser system was performed using the procedure described in Chapter 4, and the results are compared to those from the high speed system. It was found that the PL-DIC performed as well or better than the high speed system, with the potential for improvement through the use of higher resolution cameras.

Finally, some results are presented which demonstrate the capabilities of the PL-DIC system to measure the deformation of a panel subjected to resonant and random excitation.

5.2 Image acquisition at resonance

When considering stroboscopic illumination, the major factors influencing the measurement are the pulse duration and intensity. Typical arc discharge systems tend to become less intense as the frequency is increased. Newer systems utilizing LED illumination are limited by the power supplies and ultimately have minimum pulse widths on the order

of microseconds. However, with a pulsed laser it is possible to obtain very bright illumination with pulse durations on the order of nanoseconds. Hence, a prototype DIC system has been designed around a pulsed Nd:YAG laser (Nano L-200, Litron) with a wavelength of 532nm that produces a pulse with a duration of only 4 nanoseconds, and has an output power of 200mJ. The system is shown in operation in figure 5.1.

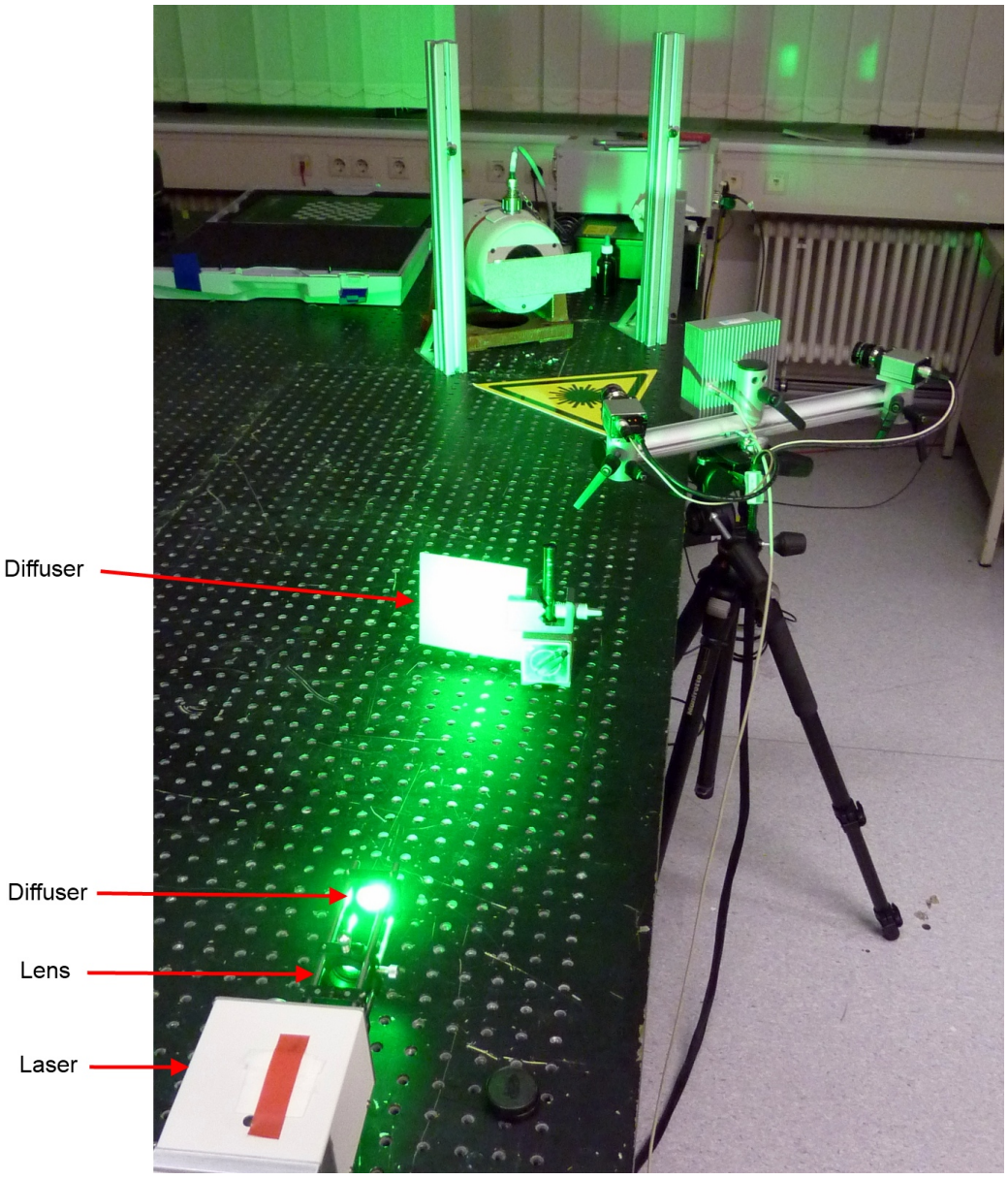

Figure 5.1: An image captured with a pulse from the laser illuminating the vibrating component. Note the lens and diffusers used to obtain uniform illumination from the laser.

The operation of this system is limited by the repetition rate of the laser rather than

the cameras. The laser is capable of operating at a repetition rate of 10Hz whereas the cameras can achieve 30+ fps. A schematic of the system is shown in the top of figure 5.3.

The PL-DIC system is able to capture the full motion of a vibrating component by phase shifting the image acquisition relative to the vibration. In order to do this the motion of the component should be periodic, and the excitation signal must be routed to the timing box of the DIC system. Figure 5.2 shows how the image acquisition is shifted relative to the vibration signal. Typically, for the experiments performed here, images were captured in 9 degree phase increments. This meant a total of 40 images would capture a full cycle of vibration.

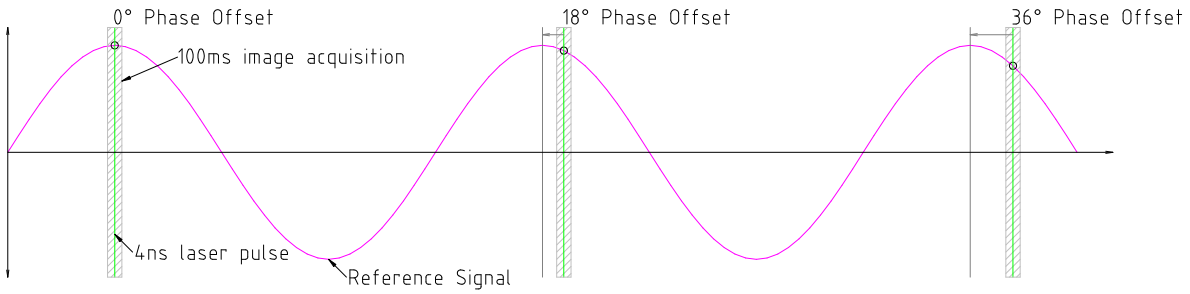

Figure 5.2: The phase stepping of the PL-DIC system. In this example the images are being captured at 18 degree phase increments relative to the excitation signal.

5.3 Image acquisition with random excitation

It is important to the Air Force to have a system which is capable of capturing data from a component test which is subjected to broadband random excitation, as this is the type of excitation that a real hypersonic structure would encounter. They are working to create simulations which capture the complex and non-linear behavior that occurs from the combination of thermal, fluid, and acoustic loading. In order to be meaningful for the prediction of component life, these simulations need to be validated, preferably with full-field experimental data. As it is not practical (or even possible without UV) to capture

the massive amount of data necessary with high-speed cameras, a simpler approach was desired which would capture only the relevant data.

The previous section described a setup in which the signal from the function generator was used to drive the shaker system and also to trigger the acquisition of images. This works perfectly for single frequency excitation, but it was necessary to separate the image acquisition from the excitation to address random excitation. For this reason a laser vibrometer was introduced into the experimental setup which is shown in the bottom of figure 5.3. The laser vibrometer only needs to be aimed at a reflective part on the vibrating component and it uses a low power laser beam to measure the surface velocity. It outputs a voltage signal proportional to velocity, which can then be used as the reference signal by the DIC software. In this fashion the PL-DIC system can be completely decoupled from the experiment.

The remaining challenge was to determine when to trigger the image acquisition with the cameras when the panel was excited with a random signal. It was decided to take an approach based on the energy in the vibrating panel. If the panel is considered as a system, it is storing and releasing energy as it is being forced by the shaker. The kinetic energy is given as

$$E_k = \frac{1}{2}mv^2 \tag{5.1}$$

The mass is assumed to remain constant, so kinetic energy will be dependent only on the velocity of the panel, which can be measured (at a point) using the laser vibrometer. The peaks of the measured signal will occur when the velocity is the highest, and therefore the kinetic energy at that point is at a maximum. When the velocity is zero, the kinetic energy will be zero and all of the energy will be stored in the panel. This should be the point of maximum deformation in the panel.

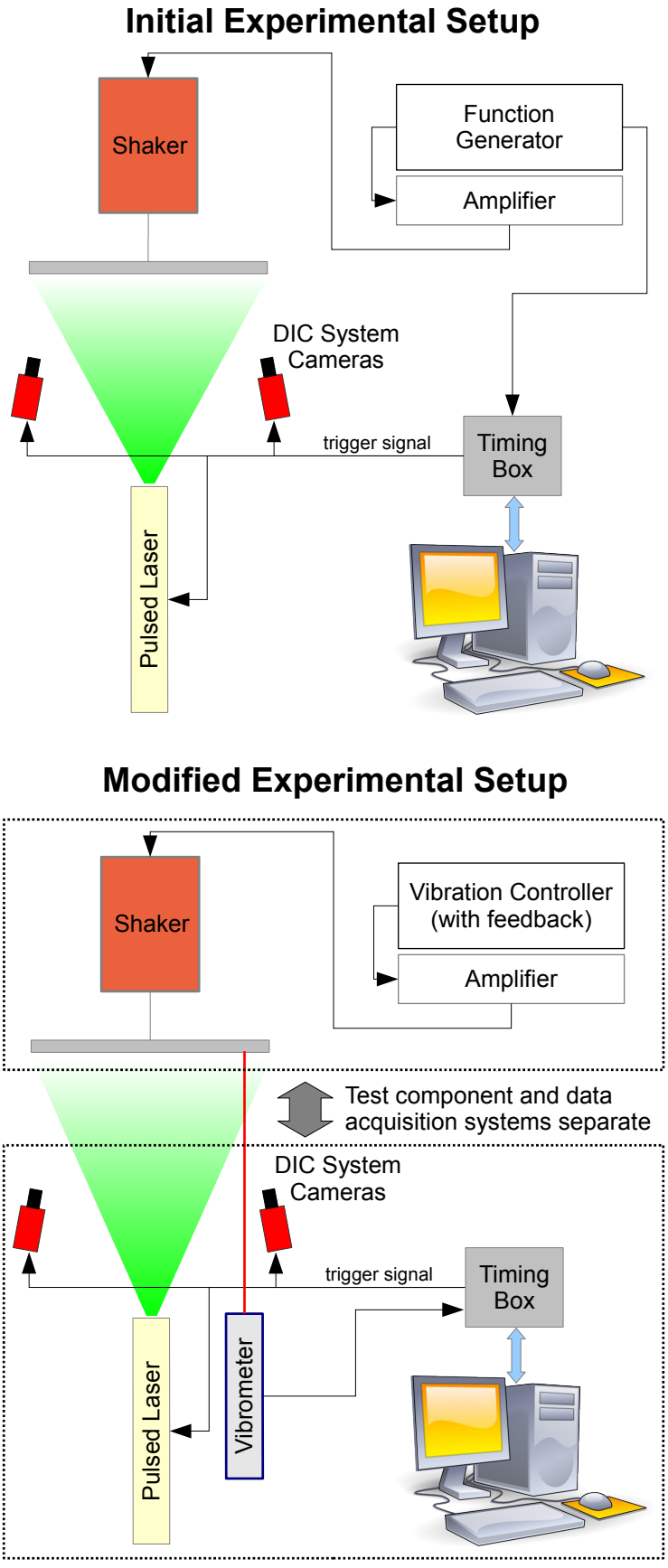

Figure 5.3: The original experimental setup used for resonant excitation *(top)* and the modified setup with the addition of the laser vibrometer used for random excitation *(bottom)*.

A system was created using LabVIEW to trigger the acquisition of images at the points of maximum potential energy. A National Instruments USB-6351 data acquisition module was used as it has the capability to trigger a counter output from an analog signal. The laser vibrometer outputs an analog voltage signal, so this was routed to the USB-6351 device and the counter output was connected to the trigger input of the DIC system. An example velocity trace and the trigger point are shown in figure 5.4. Looking at this typical trace, it can be seen that the amplitude is generally constant with the occasional large velocity excursion. If it is assumed that the maximum potential energy will be stored immediately following a point of maximum velocity, a trigger scheme needed to be devised to trigger the cameras at a point of zero velocity immediately following a peak. This was done by setting the trigger to assert on a falling edge at 0 velocity, with a threshold value set just below the peaks.

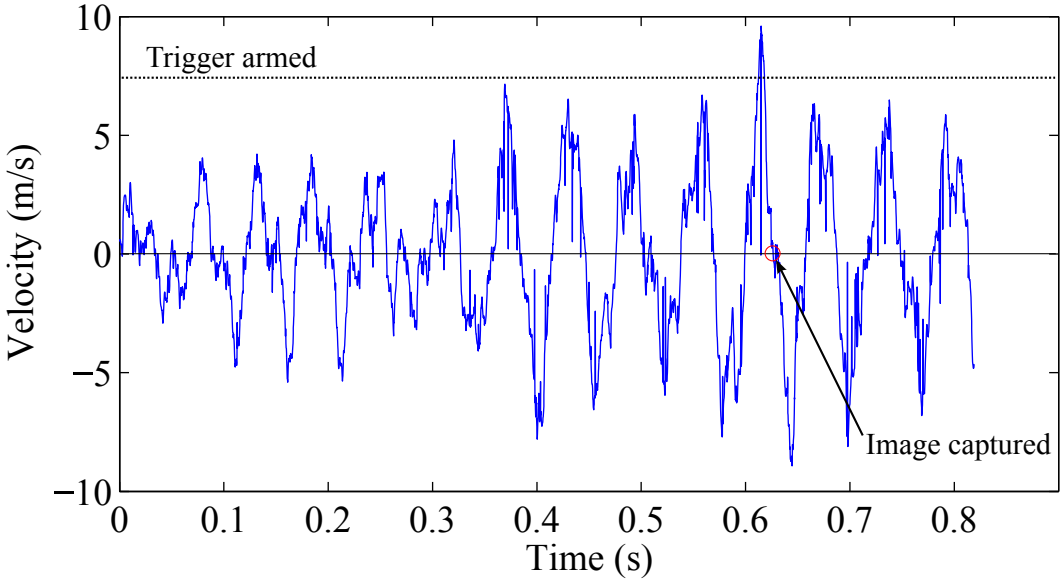

Figure 5.4: An example of the velocity signal measured with the laser vibrometer while applying random loading to the panel. The circle indicates the point at which the PL-DIC system acquisition was triggered.

5.4 Comparison to High-Speed DIC

The same reference material and procedure that was described in Chapter 4 to assess the high speed DIC system was used to assess the PL-DIC system. This was done to see how the uncertainties resulting from the different methods compared. While the PL-DIC system is based on cameras that have a slightly higher resolution than the high speed cameras (1624x1234 vs. 1280x800 pixels), it was thought that there might be some non-uniformity in the laser illumination source that would increase the measurement uncertainty. The increased resolution of the PL-DIC system meant that it had an image magnification of 9.2 pixels/mm, compared to 7.2 pixels/mm for the setup with high speed cameras. During the post-processing, the subset size was increased to 39 pixels to keep physical size the same as was used in Chapter 4, although this could potentially reduce the noise in the results.

The resulting uncertainty for the PL-DIC system is shown in table 5.2. Comparing

Table 5.2: Summary of the calibration uncertainty results for each of the three frequencies. N is the total number of experimental data points produced. $u(d_k)$ is the uncertainty from the residuals. $u(w_k)$ is the uncertainty from the cantilever reference material. $u_{\text{cal}}(w_k)$ is the combined uncertainty, and the last column on the right is the percent uncertainty relative to the amplitude of displacement for that frequency.

	N	$u(d_k)$ μm	$u(w_k)$ μm	$u_{\text{cal}}(w_k)$ μm	Amplitude μm	Relative %
$1^{st} : 126Hz^{(-)}$	1318	1.6	2.1	2.6	615	0.4%
$1^{st} : 126Hz^{(+)}$	1318	1.6	2.1	2.6	615	0.4%
$2^{nd} : 796Hz^{(-)}$	1284	2.7	2.1	3.4	320	1.1%
$2^{nd} : 796Hz^{(+)}$	1284	2.6	2.1	3.3	320	1.0%
$3^{rd} : 2123Hz^{(-)}$	1284	2.8	1.7	3.3	90	3.6%
$3^{rd} : 2123Hz^{(+)}$	1284	2.7	1.7	3.2	90	3.5%

these results to those from the HS-DIC system in table 4.3, it can be seen that the two systems performed similarly. Figure 5.5 plots the combined uncertainty, u_{cal}, from the two methods. At the 126 Hz frequency, the two systems performed almost identically,

but at the higher frequencies the PL-DIC system had a lower uncertainty than the HS-DIC. However, the slightly lower uncertainty in the PL-DIC system could be a result of the larger subset used to process the images, as this would reduce the random error component.

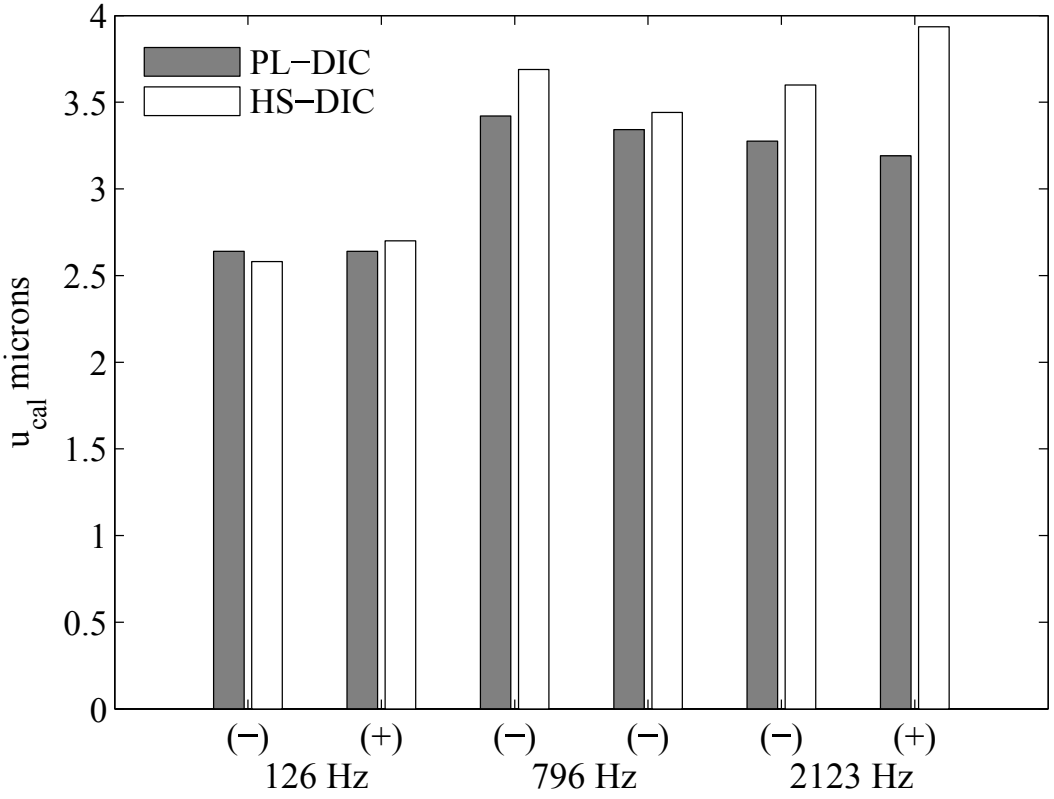

Figure 5.5: Comparison of u_{cal} from the PL-DIC and HS-DIC systems.

5.5 Results and discussion

A set of displacement measurements were taken using single frequency excitation with the experimental setup shown in the top of figure 5.3. A 600mm by 400mm by 1.7mm thick flat aluminum panel was used for the experiments. The front side of the panel was covered in a white vinyl with a random black speckle pattern printed on it. The PL-DIC system was used with a pair of 8mm lenses (Cinegon 1.4/8mm, Schneider, Germany) set to $f5.6$.

The excitation frequency was produced using a function generator, which was tuned to match the resonant frequency of the panel by monitoring the response with the laser vibrometer. Once the frequency was properly set, a series of 20 images was captured at 18 degree phase increments. In this fashion the first several modes of vibration were captured, covering a frequency range of 20-400Hz. The out-of-plane displacement of the vibration modes is shown in figure 5.6.

Using the pulsed laser with resonant excitation, it was possible to capture the displacement of the panel over a wide range of frequencies and amplitudes of vibration. The displacements were calculated using a commercial code (Istra4D, Dantec Dynamics) by comparing the images to a reference that was captured before exciting the panel. A subset size of 59 pixels with an overlap of 40 pixels was used to process the data. This subset size was chosen due to low contrast in the printed speckle pattern. With a better pattern it would be possible to reduce the subset size. At the lower frequencies, such as the 20 Hz bending mode, the out-of-plane displacement was of the order of 1mm. At the higher frequencies, this displacement was only 0.1-0.2mm.

Following the single-frequency measurements, the system was reconfigured for random excitation in which the laser vibrometer was used to trigger the image acquisition as shown in the bottom of figure 5.3. The panel was excited using a broadband random signal over the range of 20-1000Hz. The spectrum was produced using a shaker controller (ABAQUS, DataPhysics) with feedback from an accelerometer mounted to the back of the panel.

As the excitation was random for these experiments, the signal from the laser vibrometer was used with the LabVIEW program to intelligently trigger the cameras and pulsed laser. The program was set to trigger at the zero-crossing of the velocity signal immediately following a peak as shown in figure 5.4. In addition to triggering the cameras and pulsed laser, the LabVIEW program was setup to record the time history data from

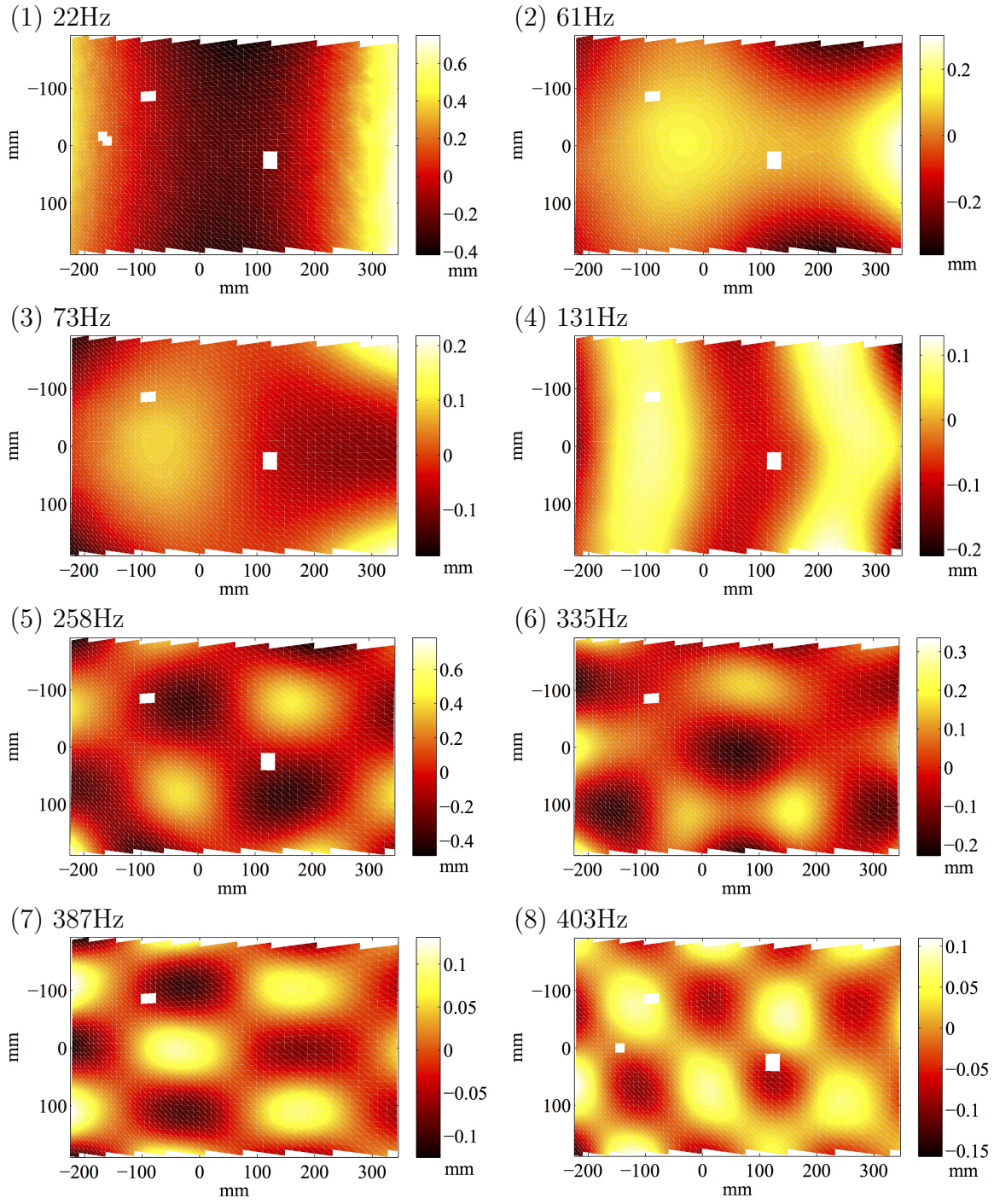

Figure 5.6: The out-of-plane (z-displacement) at resonance of the flat panel measured using single frequency excitation and phase shifting of the image acquisition.

the laser vibrometer. A total 4096 samples of data from the vibrometer were captured at a rate of 5000 Hz each time the system was triggered. This recording rate was chosen as the upper limit of the frequency range of interest was 500 Hz, so this was ten times that. Of the 4096 samples, 3072 of them were pre-trigger, and the remaining 1024 were post-trigger. A total of ten data sets were captured in this fashion.

The data from the laser vibrometer was imported into Matlab as a text file and processed to calculate the fast Fourier transform (FFT) of the signals. The resulting FFTs of the acquisitions are shown in figure 5.7. The 10 different signals have been plotted together to better show the trends in the data rather than detail of individual measurements.

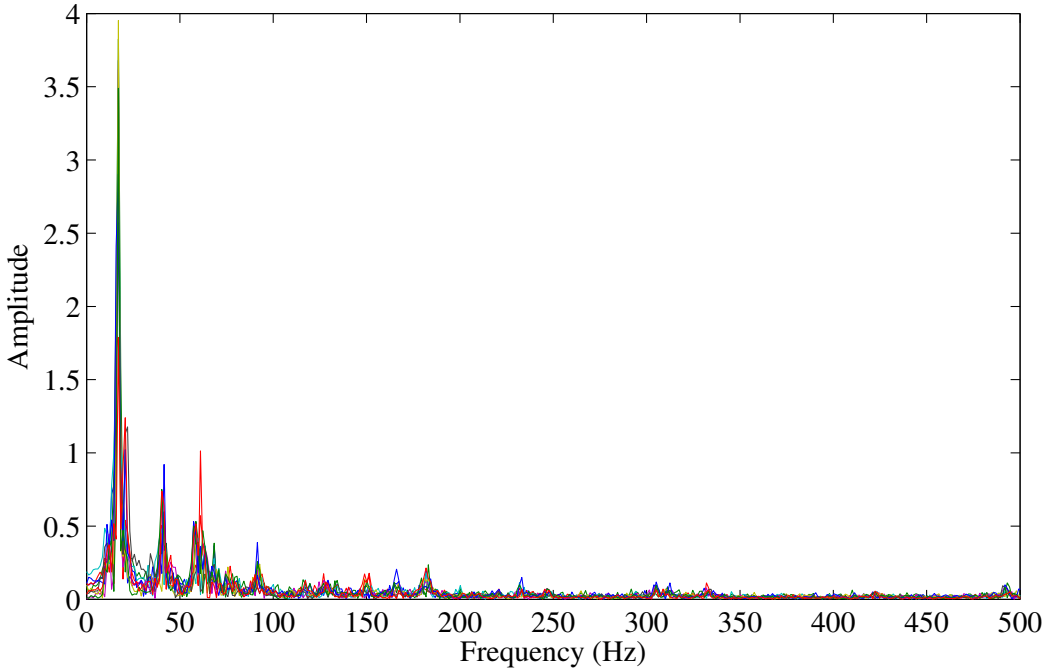

Figure 5.7: The FFT of the time history of the velocity signal from the laser vibrometer of the panel.

Examining figure 5.7, it can be seen that the response is dominated by a peak that occurs at 17Hz. This likely corresponds to the first torsional mode which was not measured, while the bending mode at 22 Hz was. There are also peaks at 42, 61, and 91 Hz

which correspond to some of the other modes. The experimentally measured deflected shapes corresponding to the 61Hz frequency can be seen in figure 5.6.

Four examples of the out-of-plane displacement captured with the random excitation are shown in figure 5.8. A total of three sets of ten data captures were collected and the full results can be found in Appendix D. These four in particular were chosen as a representative sample of the different deformation shapes that were captured. As the FFT of the vibrometer data contained several frequency components, one would expect this to be true of the full-field displacement response as well. Although this is only a few of the images captured with the random acquisition, the first bending mode is predominant with some features from the higher modes visible. The top right displacement map from figure 5.8 is interesting as it does not appear to be dominated by the first mode. Instead, it appears to be a combination, perhaps of the first and second modes.

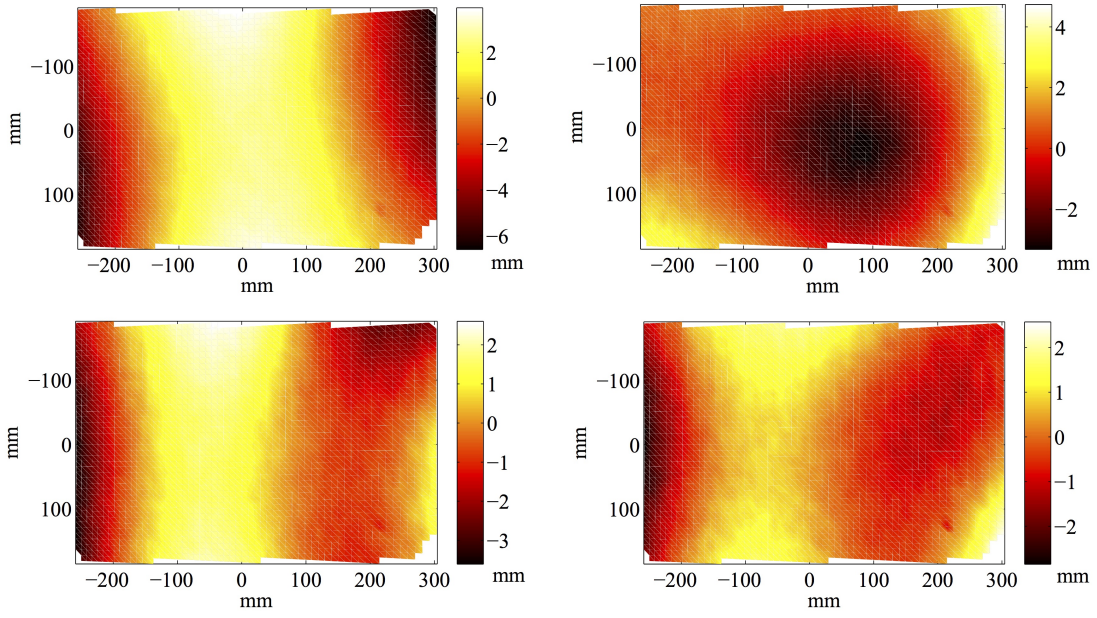

Figure 5.8: Four examples of different z-displacement measurements captured using the custom LabVIEW system and random excitation of the panel.

The individual FFTs calculated from the laser vibrometer signal which correspond to the out-of-plane displacement measurements is shown in figure 5.9. Since the majority of the response is below 100Hz, the plots have been truncated relative to figure 5.7 for clarity.

Whereas from figure 5.7 there appeared to be a single peak at 17Hz, the individual plots show that there are actually multiple peaks around this frequency. This is especially true in the top-left figure, as a distinct peak can be seen at 22Hz, which would correspond to the bending mode.

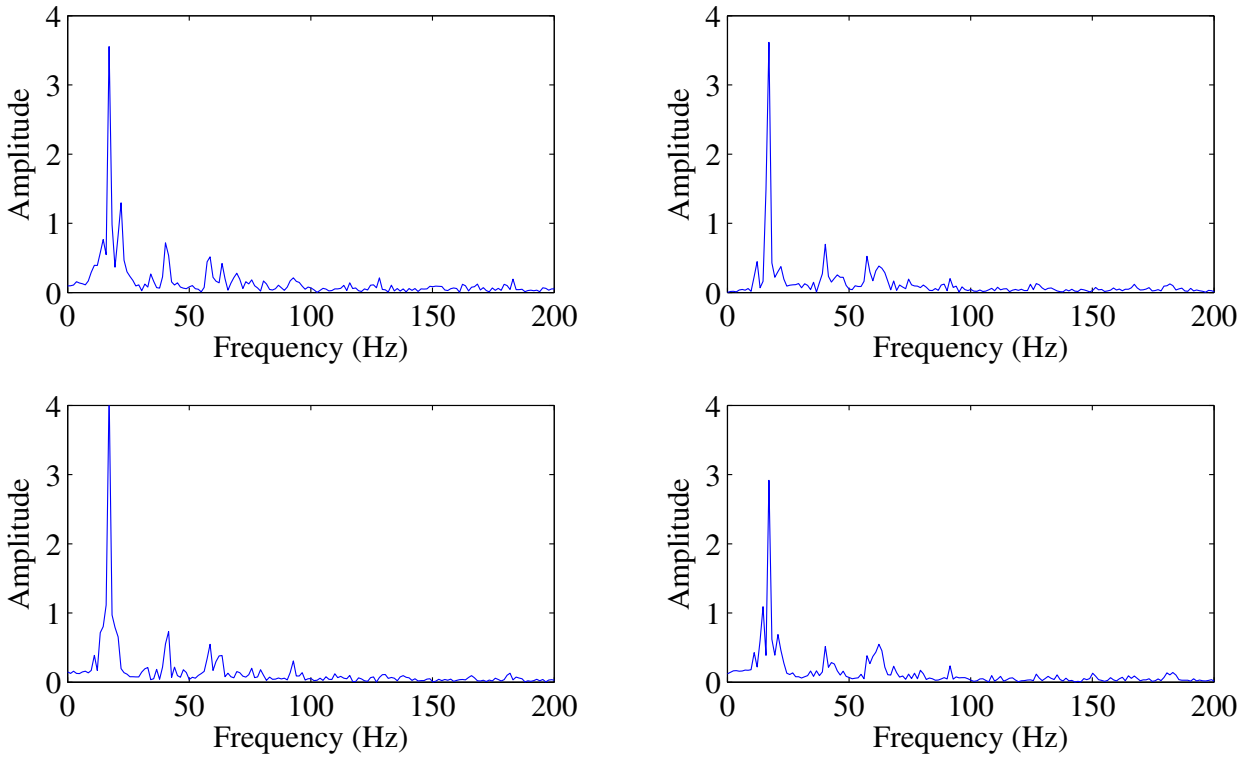

Figure 5.9: The FFT calculated from the laser vibrometer measurement that corresponds to figure 5.8.

The bottom-right FFT appears to be the most different from the others, in that the magnitude of the first peak is smaller. It also has more area under the 61Hz range, which corresponds to one of the modes measured previously in figure 5.6.

The displacements of the panel were calculated using the DIC code by comparing the images triggered at the peak velocity to a reference, undeformed image. The in-plane displacements for the top left image of figure 5.8 are shown in figure 5.10. In addition, the strain components in the x and y directions have been calculated. The strains were calculated from the displacement maps after applying a smoothing spline to the data with a grid reduction factor of 4 and a smoothness factor of -1.

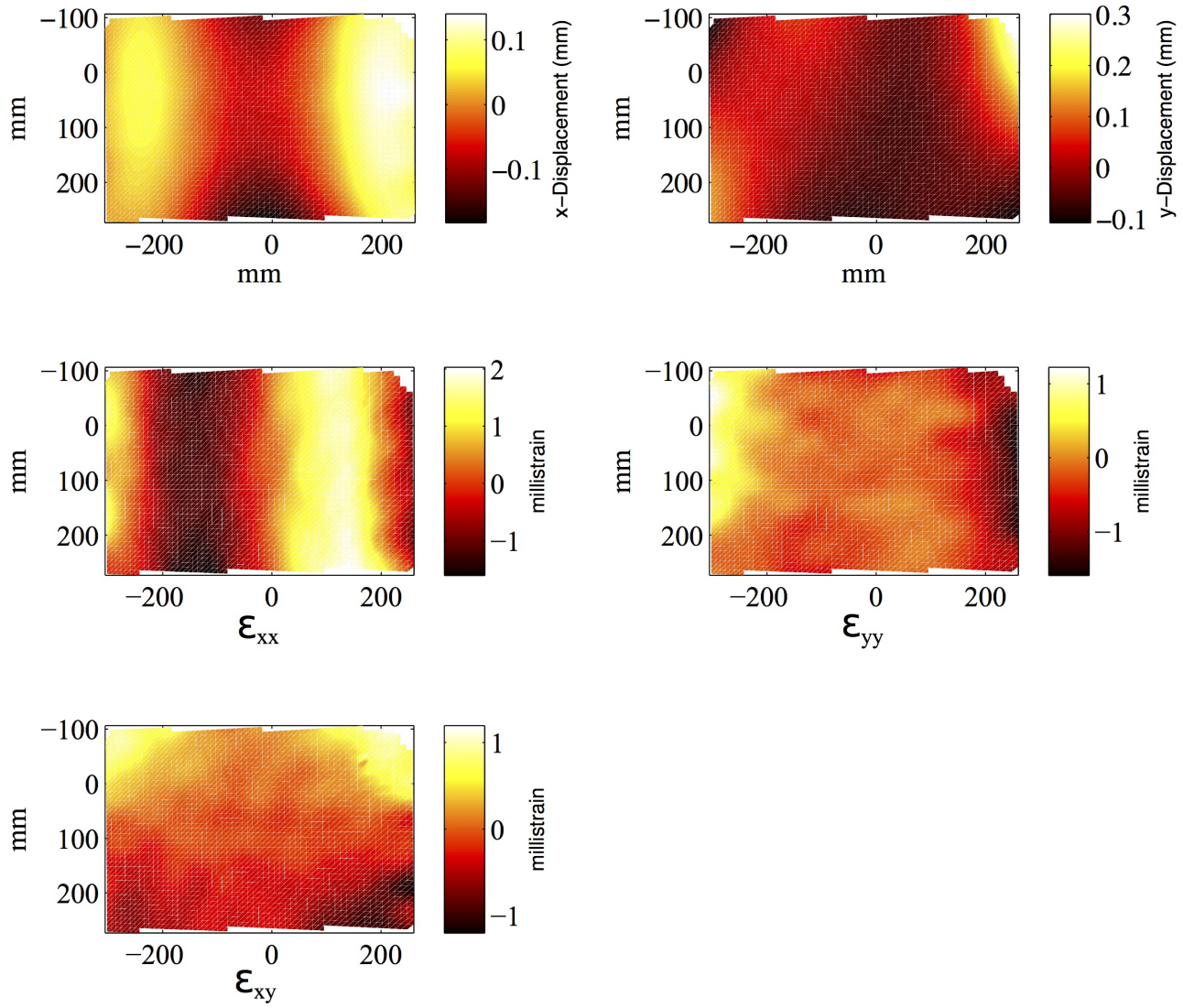

Figure 5.10: The in-plane displacements and strains calculated from the top-left example shown in figure 5.8.

As fatigue analysis typically uses strain data, the capability to measure strain during random excitation is important. Rather than using high speed cameras to capture large of amounts of data which then must be post-processed, a laser vibrometer was used to "intelligently" capture data of interest. Although modes up to 400Hz were measured using resonant excitation, the frequency response calculated from the FFTs indicated that the majority of the response was below 100Hz. Looking at the modes captured from figure 5.8, they appear to be representative of this.

5.6 Conclusions

A novel method to measure displacement and strain of a component excited with different inputs, including single frequency and random, has been presented. Typically this would require the use of high speed cameras, so a study was performed to see how well the pulsed laser system compares to high speed DIC. The systems were evaluated over a frequency range of 126-2123 Hz and an out-of-plane displacement of $90 - 600\mu m$. The PL-DIC was found to perform as well or better than the HS-DIC system, with a calibration uncertainty ranging from $2.6 - 3.4\mu m$.

The system was then used to capture the mode shapes of a rectangular panel excited at resonance. This was accomplished by phase shifting the acquisition relative to the excitation signal. The modes up to 400 Hz were captured with the system, with out-of-plane displacements ranging from 0.1-2.0 mm.

Finally, measurements were made of the panel using the PL-DIC system and excitation with a random vibration signal. The acquisition of images with the PL-DIC system were triggered by a laser vibrometer that monitored the surface of the panel. The acquisition was triggered at the zero-crossing immediately following a peak in the velocity signal, corresponding to maximum stored energy in the panel.

With the PL-DIC system and random excitation, it was possible to capture both the in-plane and out-of-plane components of displacement of the vibrating panel. These displacement were then used to calculate the associated strains in the panel. The ability to measure strains using random excitation without the use of high speed cameras is novel and will be critical to develop the technique for the purpose of validating structural mechanics models for life prediction.

Chapter 6

Validation of an Aerospace Component Simulation

6.1 Introduction

There are many challenges in the path of validation of computational models, especially when dynamics is involved. The use of full-field methods of experimental stress and strain analysis is gaining momentum, but presents new challenges in dealing with the large amount of data and the issue of performing a meaningful comparison with the simulation. There are also issues with capturing data during dynamic events, as fast motion requires the use of stroboscopic illumination or expensive high speed cameras. The actual comparison of the full-field experimental data to the simulation data can be difficult due to issues with alignment of the coordinate systems, scaling, and interpolation. Therefore the validation of dynamic models is especially challenging, as it encompasses all of these issues.

This chapter presents a validation of a computational mechanics model of a prototype aircraft panel using vibration data captured from 3D digital image correlation. Pulsed Laser DIC has been used to address the challenge of capturing the deformation of the panel resulting from the vibration excitation. To overcome the problems associated with the comparison of the experimental and simulation data, image decomposition has been used to compress the large data sets into a relatively small number of feature vectors.

The comparison was then made between the sets of feature vectors rather than the original data sets. The experimental setup was evaluated using the Reference Material and procedure from Chapter 4 to determine the measurement uncertainty.

The out-of-plane (z-direction) displacement was measured using the PL-DIC while exciting the panel at its first three resonances. The results were compared to those obtained from a modal frequency response simulation using Finite Element (FE) analysis. Four different simulation conditions were considered by varying the damping, constraints, and mesh type. Images were captured in 18 degree phase increments over the entire 360 degree cycle of vibration. The experimental and simulation results at each phase step were compared using image decomposition with the Tchebichef descriptor. In this example, the measured and predicted displacement from the simulation were compared with a confidence interval defined by the uncertainty in the experimental data.

6.2 Experimental setup

The panel used in these experiments was an 800mm wide by 400mm high aerospace component that had been milled from a single block of 7075 aluminium. A drawing of the panel is included in Appendix A. The panel was suspended by string from a framework mounted to a table. A speckle pattern was applied with paint, first with a base layer of white and then the speckle provided using a sponge to dab on the black. Pictures of the panel in the experimental setup are shown in figure 6.1.

The design of the setup was based in part from the results obtained from the modal analysis. The modal analysis was used to identify a suitable excitation point and frequencies for the experiment. It was decided to use the first three frequencies, which included a torsion mode (14Hz), a bending mode (44Hz), and a combination (59Hz). The excitation was provided by an electrodynamic shaker (DataPhysics V100) which was attached to

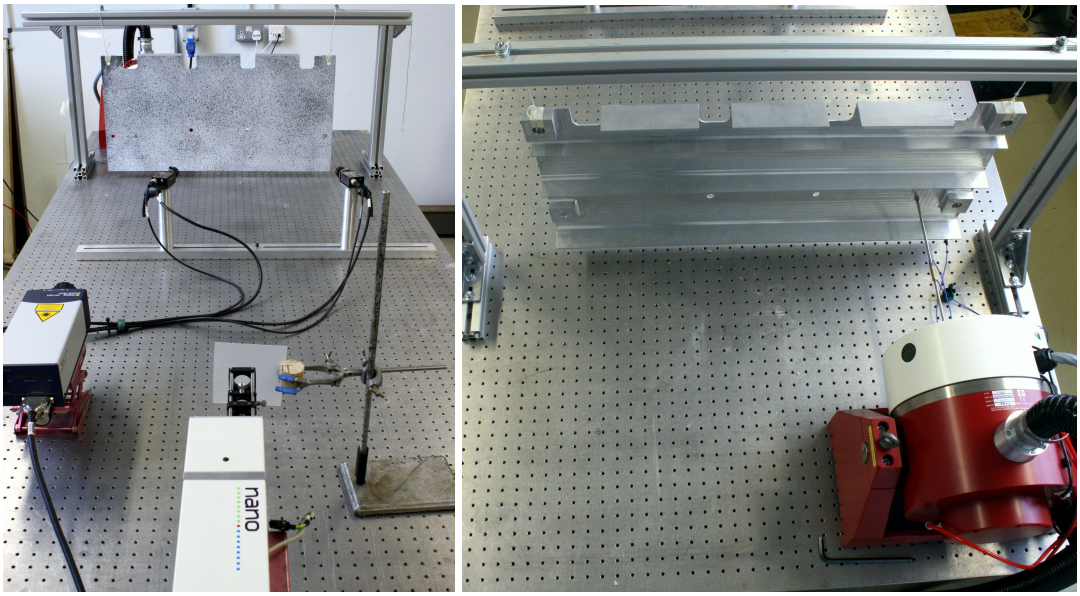

Figure 6.1: Picture of front of the experimental setup showing the cameras, laser vibrometer, and pulsed laser (*left*) and the back side of the panel showing the attachment to the shaker (*right*).

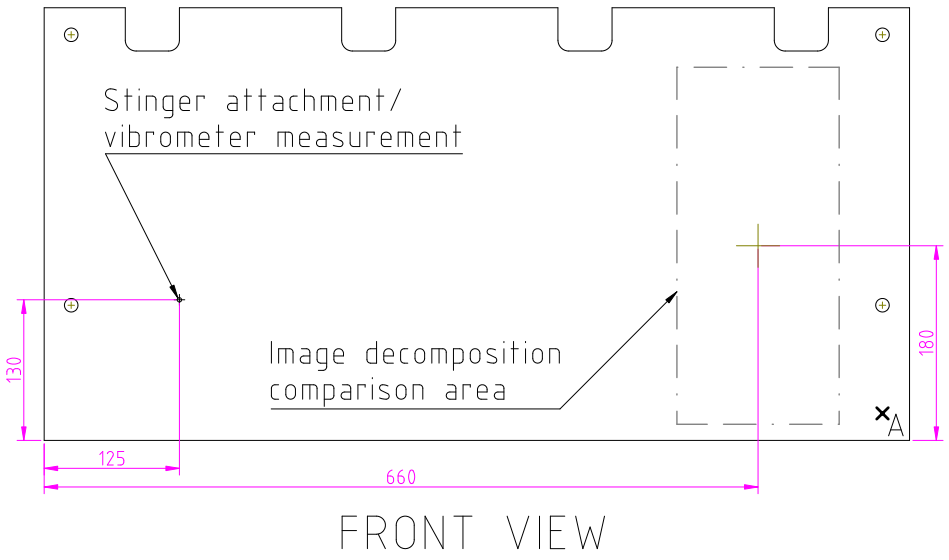

Figure 6.2: Front view of the panel showing the stinger attachment and the comparison area for the image decomposition.

the panel with a stinger (M4 300mm stainless steel rod) through a bolted connection. Figure 6.2 shows the front view of the panel and the location of the attachment of the stinger.

A function generator was used to drive the shaker at one of the panel's first three resonances. The vibration of the panel was controlled by adjusting the output of the function generator, which was in turn connected to an amplifier before being sent to the shaker. The amplitude was measured using a laser vibrometer (OFV-503, Polytec) aimed at the attachment point of the stinger. Table 6.1 shows the amplitude of vibration measured at the excitation point, and the response at the corner of the panel (Point A in figure 6.2).

Table 6.1: The measured excitation displacement at the attachment point of the stinger and the response of the panel at point A.

	Amplitude p-p (mm)	
	Excitation	Response pt. A
14Hz (1^{st} mode)	0.18	3.2
44Hz (2^{nd} mode)	0.34	1.6
59Hz (3^{rd} mode)	0.10	3.3

Images of the vibrating panel were captured using the PL-DIC system based on a pair of 2 megapixel firewire cameras with 1624x1234 pixel resolution (Stingray F-201B, AVT). The cameras were fitted with a matched pair of 8mm lenses (Cinegon 1.4/8, Schneider) set to an f-stop of 5.6, providing an image magnification of approximately 3.1 pixels/mm. A laser with a 4 nanosecond pulse duration and wavelength of 532 nm was used to freeze the motion of the panel. In addition to providing the driving frequency to the shaker, the function generator also provided a synchronization signal which was routed to the timing box of the DIC system. A diagram of the experimental setup is given in figure 6.3.

The DIC software (Istra4D, Dantec Dynamics) was used to phase shift the image acquisition relative to the driving frequency, permitting the capture of the entire cycle of

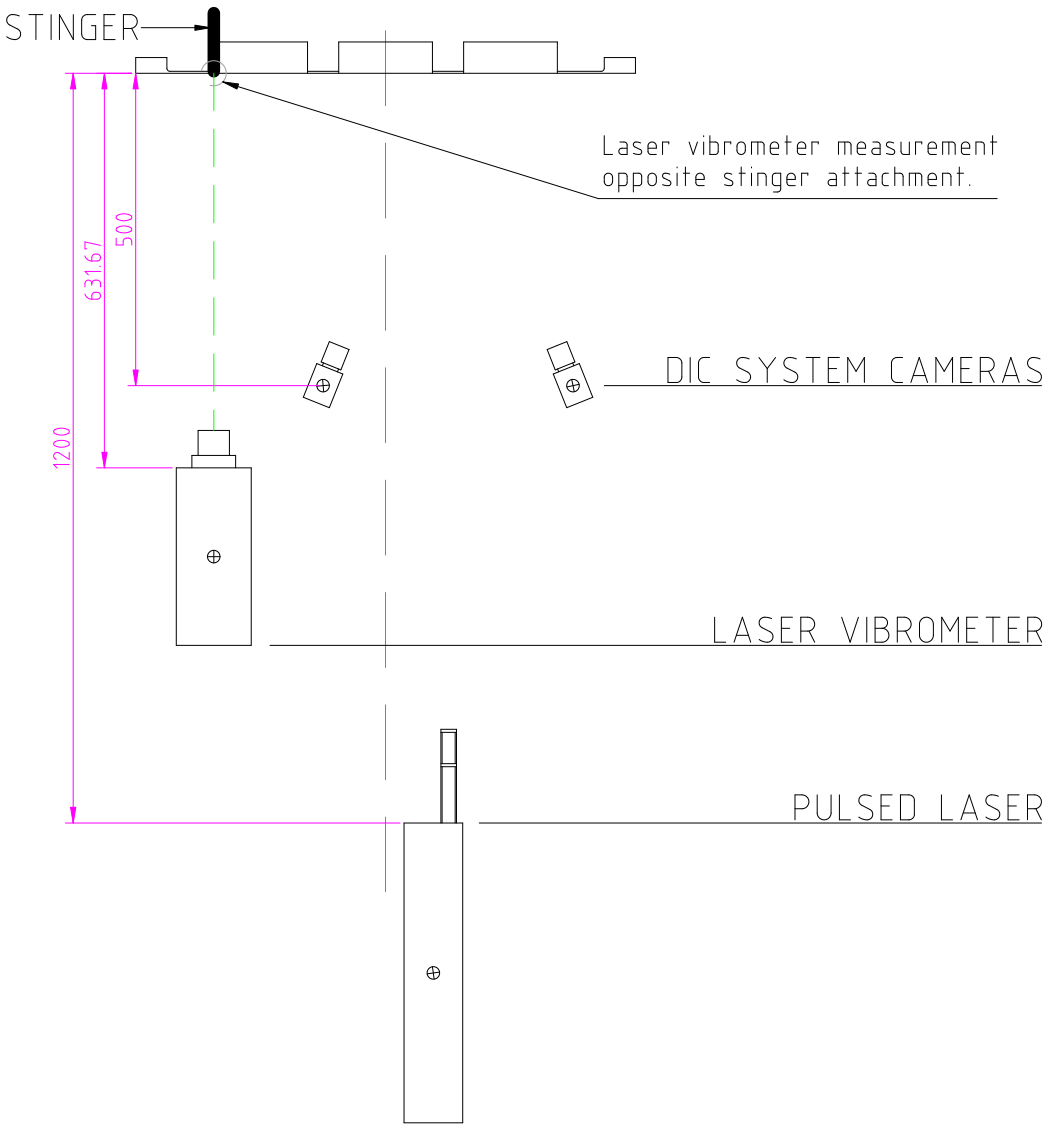

Figure 6.3: Diagram showing the arrangement of the experimental apparatus and the attachment of the shaker.

vibration of the panel. A total of 20 images were captured in this fashion at 18 degree phase increments, covering a full 360 degree cycle. The images were processed with the software using a subset size of 49 pixels and an offset of 20 pixels. The subset size was set to this relatively large value to compensate for the quality of the speckle pattern, which was applied by hand and not very uniform. A printed pattern could have potentially been used, although for such a large area there can be issues with bubbling or peeling of the surface.

The pulsed laser was triggered at the same time as the cameras and provided the illumination of the vibrating panel. In order to measure the amplitude of displacement of the excitation, a laser vibrometer was aimed at the front side of the panel where the stinger was attached. Both the velocity and the displacement analog voltage signals from the laser vibrometer were recorded by the data acquisition unit of the DIC system.

6.2.1 Dynamic calibration

A dynamic calibration was performed according to Chapter 4. The procedure was performed to assess the minimum measurement uncertainty in the experimental setup, which was then used in comparing the simulation data. A 160mm x 40mm x 4mm thick cantilever machined from a single aluminum block was excited acoustically while capturing the out-of-plane displacement with the PL-DIC system.

To assess the uncertainty of this particular experimental setup, the cameras were left in the exact same position as they were during the measurements of the aerospace panel. However, this meant that the cantilever that was used was smaller than the desired field of view for the experiments, so it was moved around to six different locations. Figure 6.4 shows the images from both of the cameras at each of the six different locations of the cantilever. Measurements were taken with the cantilever in both a horizontal and

vertical positions, to see if there was any difference in the uncertainty.

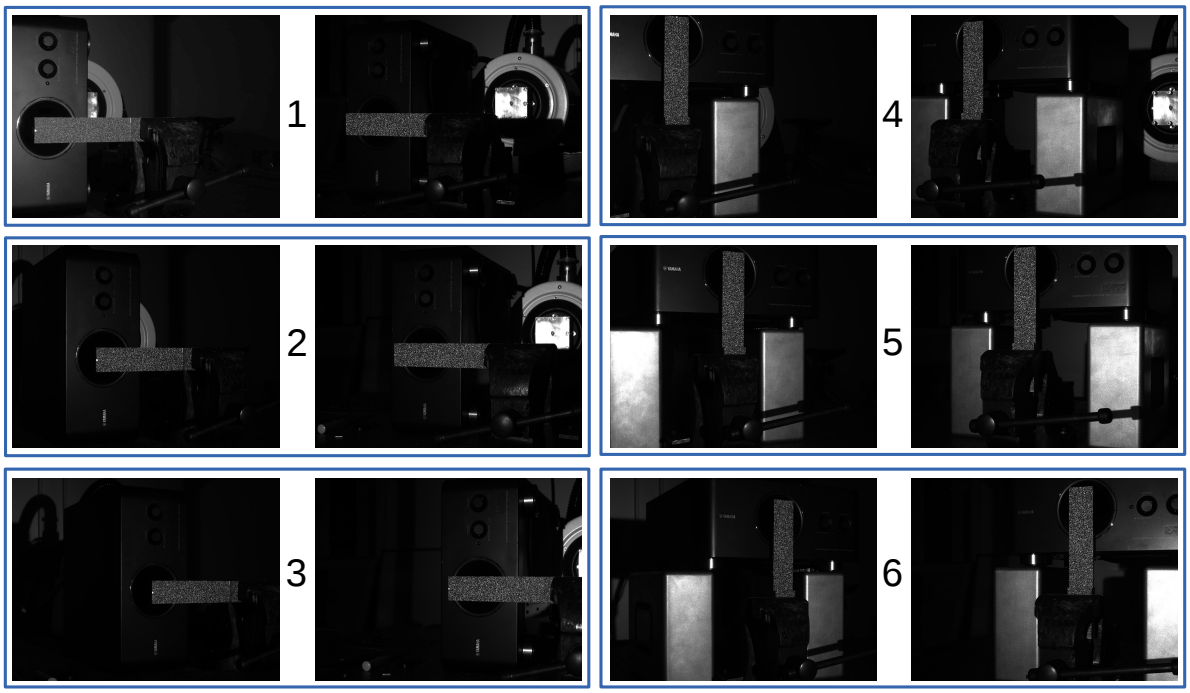

Figure 6.4: Images captured by the PL-DIC system of the cantilever at six different positions in the field of view. Locations 1-3 are with the cantilever horizontal and 4-6 are vertical.

The results are summarized in table 6.2 and compared to those previously obtained with the High-Speed DIC system. It should be noted that the image magnification was slightly less than half of what was achieved with the high-speed system, as a result of increasing the field of view for the larger aerospace panel. The uncertainties were calculated with the cantilever at the two extrema of deflection, denoted by $^{(-)}$ and $^{(+)}$ in the table.

6.3 Simulation setup and results

Initially a real eigenvalue analysis was performed to identify the mode shapes and natural frequencies of vibration for the panel. The analysis was performed using a commercial FE package (Altair Optistruct, MI USA). The mesh was created manually, with care taken

Table 6.2: Comparison of the uncertainty from the high speed cameras and the PL-DIC. N is the number of data points evaluated, $u(d_k)$ is the uncertainty in the measurement, $u_{cal}(w_k)$ is the combined uncertainty. The last column gives the uncertainty expressed as a percentage of the measured amplitude of vibration from the calibration process.

	N	$u(d_k)$ μm	$u(w_k)$ μm	$u_{\text{cal}}(w_k)$ μm	Amplitude μm	Relative %
High-Speed$^{(-)}$	1258	1.5	2.1	2.6	600	0.4%
High-Speed$^{(+)}$	1258	1.8	2.1	2.7	600	0.5%
PL-DIC-1$^{(-)}$	491	4.1	2.1	4.7	495	0.9%
PL-DIC-1$^{(+)}$	491	4.0	2.1	4.5	495	0.9%
PL-DIC-2$^{(-)}$	370	3.6	2.1	4.1	502	0.8%
PL-DIC-2$^{(+)}$	370	3.6	2.1	4.2	500	0.8%
PL-DIC-3$^{(-)}$	318	3.5	2.1	4.1	494	0.8%
PL-DIC-3$^{(+)}$	318	3.3	2.1	4.0	493	0.8%
PL-DIC-4$^{(-)}$	467	4.2	2.1	4.7	522	0.9%
PL-DIC-4$^{(+)}$	466	3.5	2.1	4.1	522	0.8%
PL-DIC-5$^{(-)}$	383	3.7	2.1	4.3	519	0.8%
PL-DIC-5$^{(+)}$	383	3.6	2.1	4.2	520	0.8%
PL-DIC-6$^{(-)}$	301	4.0	2.1	4.5	482	0.9%
PL-DIC-6$^{(+)}$	301	3.4	2.1	4.0	482	0.8%

to use brick elements. These were first order hex elements with 8 nodes per element. This resulted in a total of 170k elements. A view of the mesh is shown in the left side of figure 6.5. Due to the complexity of the mesh a convergence study was not performed as it was not practical to do so. For the purposes of this chapter it was not necessary to have a "perfect" model, as the emphasis is on the validation procedure.

The modulus of the material was 67 GPa, the Poisson's ratio was 0.33, and the density $2.85{*}10^{-9}$ ton/mm^3. The out-of-plane deformed shape of the first three eigenmodes from this analysis are shown in figure 6.6. The eigenvalue analysis was performed without applying any constraints or boundary conditions to the model. This information was helpful in designing and setting up the experiment.

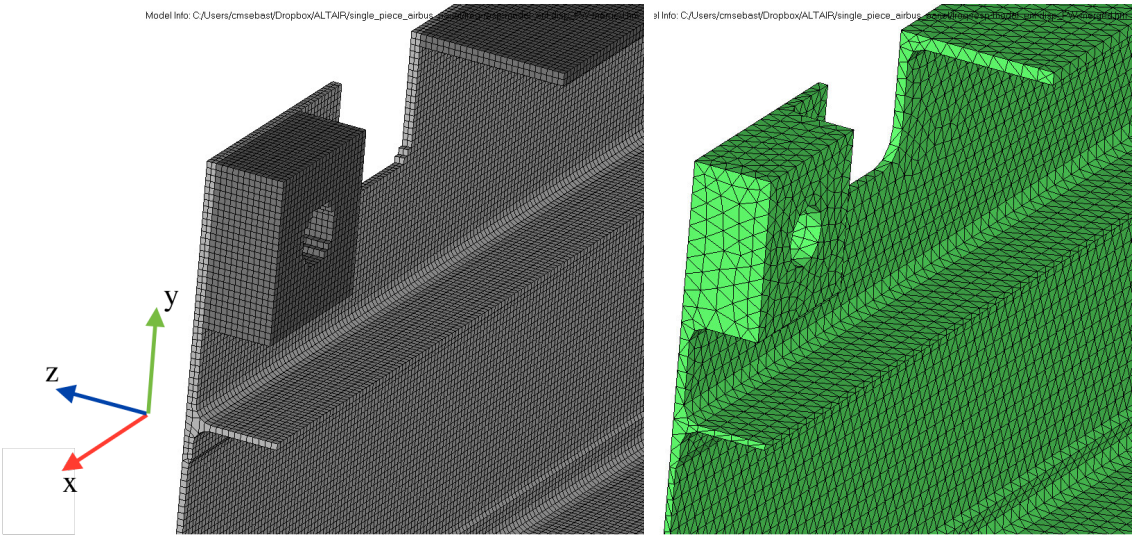

Figure 6.5: Close-up of the 3-D meshes used for the FE simulations. The manually meshed model *(left)* consisted of 170k brick elements. The computer-generated tetrahedral mesh *(right)* consisted of 115k elements.

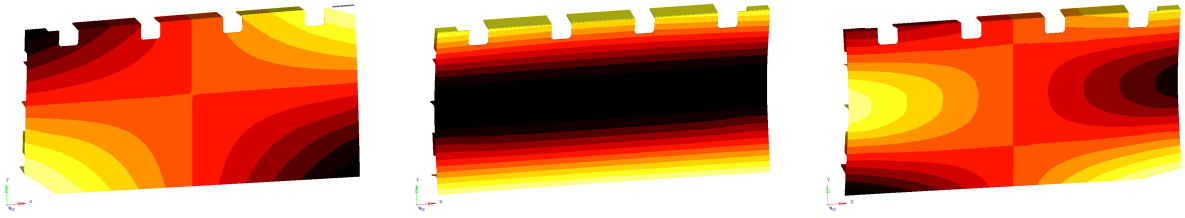

1^{st} mode (20 Hz) 2^{nd} mode (49 Hz) 3^{rd} mode (68 Hz)

Figure 6.6: The z-component of displacement plotted on the deformed shape from the eigenvalue analysis for the first three modes of vibration.

6.3.1 Simulation conditions

A modal frequency response analysis was performed to determine the full-field displacement of the panel subjected to the same loading as was measured during the experiment with the laser vibrometer. An enforced displacement constraint was applied to 12 nodes on the back of the panel at the location of the stinger from figure 6.2. These nodes were also constrained in the X and Y directions, and rotation about the Z-axis. The amplitude of the enforced displacement at each mode was measured by the laser vibrometer and is listed in table 6.1. At the first frequency, a displacement of 0.18mm was applied, 0.34mm at the second, and 0.1mm at the third.

Four different models were created to determine how sensitive the phase-stepped Tchebichef moment analysis was to various simulation conditions. The four conditions used were: baseline, constant damping, string constrained, and tetra-meshed. The deflected shapes from the simulation along with those measured with the PL-DIC system are shown in figure 6.7.

Baseline model. The baseline model was based on the quadrilateral mesh shown on the left of figure 6.5. Modal damping was used for this simulation condition, meaning that a different value was applied to each of the different modes. The values were found experimentally by using the half power method from the frequency response function. The damping coefficients were 0.045 for the first mode, 0.1 for the second, and 0.030 for the third.

Constant damping. This model was exactly the same as the baseline model except that constant damping was used rather than modal damping. For constant damping, the same value of 0.05 was used for all of the modes.

String constrained. This model was the same as the baseline with an extra constraint applied to simulate the panel hanging from the strings. Four nodes in each of the

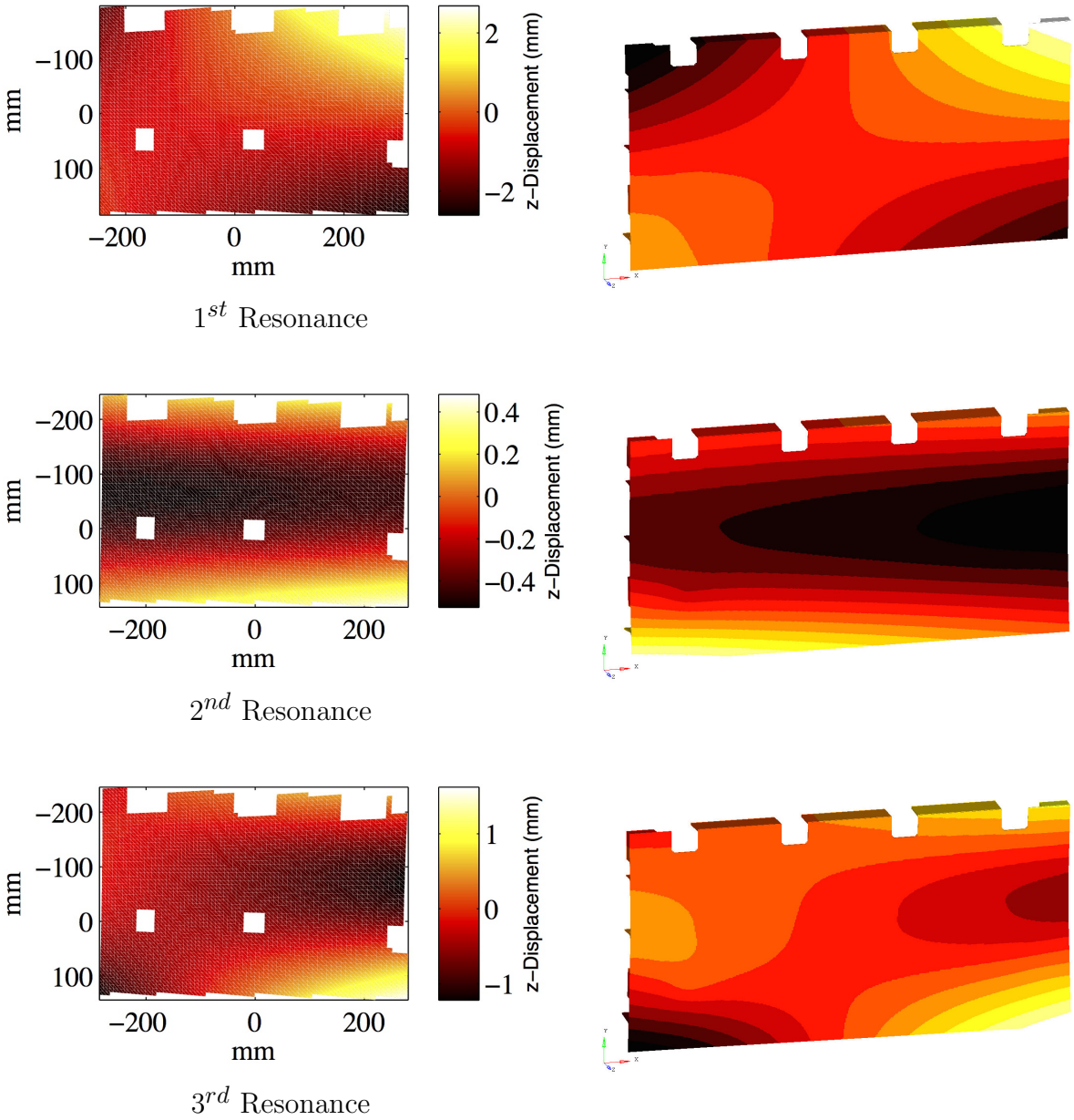

Figure 6.7: The out-of-plane displacement measured in the experiment *(left)* compared to the results from the FE modal frequency analysis *(right)*.

upper corners of the panel were constrained from translating in the y-direction.

Tetra-meshed. Whereas the baseline model was meshed with user input to ensure that primarily quadrilateral elements were used, the tetra-meshed model was meshed automatically by the software (Altair HyperMesh, MI, USA). The resulting mesh had a total of 115k elements, and is shown on the right of figure 6.5. Everything else was identical to the baseline model.

6.4 Tchebichef decomposition

The z-displacement results obtained from the PL-DIC were compared to the simulation results using image decomposition. As the data sets were rectangular and discrete, the Tchebichef descriptor (based on the Tchebichef polynomial) was used for the comparison.

The Tchebichef moments of an MxN discrete image are given by [55],

$$T_{p,q} = \sum_{x=0}^{M-1} \sum_{y=0}^{N-1} \tilde{t}_p(x)\tilde{t}_q(y)f(x,y) \tag{6.1}$$

where $\tilde{t}_p(x)$ and $\tilde{t}_q(y)$ are the normalized Tchebichef polynomials

$$\tilde{t}_p(x) = \frac{\tilde{t}_p(x)}{\sqrt{\tilde{\rho}(p,M)}}, \qquad \tilde{t}_q(x) = \frac{\tilde{t}_q(x)}{\sqrt{\tilde{\rho}(q,M)}} \tag{6.2}$$

and,

$$\tilde{\rho}(p,M) = \frac{M\left(1-\frac{1}{M^2}\right)\left(1-\frac{2^2}{M^2}\right)\ldots\left(1-\frac{p^2}{M^2}\right)}{2p+1} \tag{6.3}$$

The discrete Tchebichef polynomials are given by,

$$t_n(x) = n!\sum_{k=0}^{n}(-1)^{n-k}\binom{N-1-k}{n-k}\binom{n+k}{n}\binom{n}{k} \tag{6.4}$$

A graphical representation of the first 10 surfaces generated from the polynomial are shown in figure 6.8.

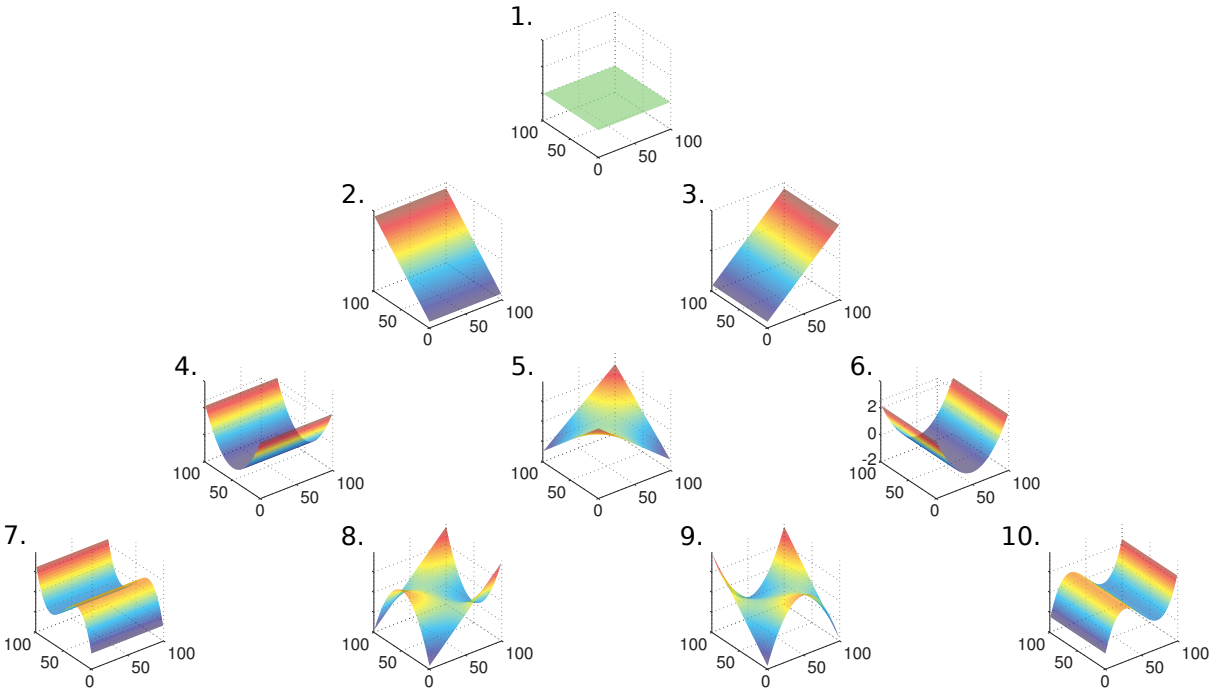

Figure 6.8: Graphical representation of the first 10 Tchebichef moments

The Tchebichef descriptor produced a feature vector from the experiment, S_E, and a feature vector from the simulation, S_M, which contained a number of moments based on the number of terms used in the process. The maximum number of terms for a data matrix is given by $(N_L * N_S) \times 1$, where N_L and N_S are the long and short dimensions of the matrix, respectively. However, this provides no reduction in dimensionality over the original image and so using the complete feature vector would not provide much benefit in the comparison process. Fortunately, it is typically not necessary to use all of the values of the feature vector to accurately describe an image. An example of the feature vector produced by the Tchebichef decomposition with 50 terms is shown in figure 6.9.

There are different approaches that can be taken during the decomposition and reconstruction process. One approach is to simply use the first X number elements of the vector. Another approach, and the one used here, is to use the most significant moments

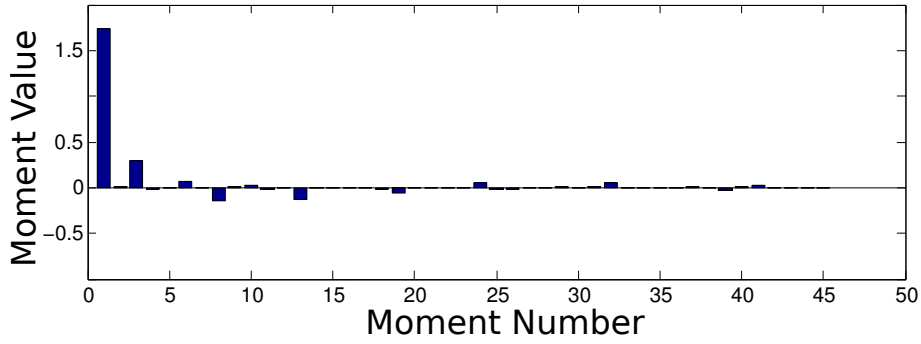

Figure 6.9: An example of the feature vector produced from the Tchebichef decomposition. In this case it can be seen that the first and third moments are significantly larger than the others.

from the feature vector. The advantage of using the most significant moments is that the largest ones are always included, regardless of their position in the vector. This is the same approach as has been successfully applied by Wang *et al.* in the past [56]. The experimental feature vector S_E was sorted in descending order of magnitude $\hat{S}_E$, and a threshold of 0.90 was defined. The first k elements of the vector were retained which satisfied the following equation:

$$\frac{\sum^{k} |\hat{S}_E|}{\sum |S_E|} \geq 0.9 \tag{6.5}$$

Regardless of the approach taken, it is necessary to check the reconstruction of the image from the feature vector, to ensure that it is an accurate representation of the original data. The author and his coauthors have provided one potential method for this procedure by analyzing the residuals resulting from the difference between the original and reconstructed image as follows:

$$u^2 = \frac{1}{n} \sum_{i,j}^{n} (\hat{I}(i,j) - I(i,j))^2 \tag{6.6}$$

where $\hat{I}(i,j)$ is the reconstructed matrix from the original data, $I(i,j)$. In addition, it

was recommended that u not be greater than the minimum measurement uncertainty and that there should not be a clustering of residuals greater than $3u$ [52].

The total uncertainty in the decomposed experimental data, $u(S_E)$, is given by a combination of the uncertainty from the reconstruction and from the calibration:

$$u(S_E) = \sqrt{u_{cal}^2 + u_E^2} \tag{6.7}$$

An expanded uncertainty can be defined as $2u(S_E)$ which will be used later on in the comparison of the experiment and simulation feature vectors.

A rectangular section of data was cropped from both the experimental and simulation data sets, indicated by the dashed line in figure 6.2. The reason a subset of the data was used is due to discontinuities in the PL-DIC data resulting from holes and other irregularities in the geometry. While it is possible to decompose data sets which contain discontinuities, it requires customization of the shape descriptors which can introduce other sources of uncertainty [56]. It was therefore decided to use a rectangular section from the data for this example. The validation could be extended to the rest of the data set by tiling the surface.

A total of 20 sets of data were compared for each of the three modes, covering a phase range of 0-360 degrees in 18 degree increments. In figures 6.10-6.12, the most significant moments from the experiment and the simulation found from equation (6.5) are plotted against each other. The experiment moments S_E are plotted on the x-axis and the simulation moments S_M are plotted on the y-axis. Each moment is plotted over the entire 360 degree cycle of vibration in 18 degree phase increments. Each of the solid markers indicates a phase increment with the 0 degree phase step circled. The four sub-figures in each plot represent the four different simulation conditions

If there were perfect agreement between the two data sets, all of the points would

lie along the ideal line with a gradient of unity. In figures 6.10-6.12, the ideal line is plotted as the solid black line. As there will tend to be scatter in the data, the author and his coauthors used a procedure in which the expanded measurement uncertainty is used to define a confidence interval to assess the agreement of the feature vectors [52]. The expanded measurement uncertainty is defined as $2u(S_E)$ and is shown as the dashed lines in the figures. For the simulation to be considered an acceptable realisation of the experiment, all of the points plotted from the two feature vectors should fall within the area bounded by the dashed lines.

Figure 6.10 shows the moments numbered 2,5,1,4,3 and 8 for the first mode of vibration. The moments are listed in order of magnitude, so the 2^{nd} moment has the largest values. As can be seen in figure 6.8 the 2^{nd} moment represents the tilt of the data along the y-axis. The next most significant moment is the 5^{th}, which represents a saddle shape, and the 1^{st}, which is a DC term.

Figure 6.11 shows the moments numbered 4,2,1,7,3,8 and 5 for the second mode of vibration. Again, the moments are listed in descending order of magnitude, so the 4^{th} moment has the largest values. As can be seen in figure 6.8 this moment represents a bending of the data along the y-axis. The next most significant moments are the 2^{nd} and the 1^{st}.

Figure 6.12 shows the moments numbered 4,2,5,1,8,7,12 and 11 for the third mode of vibration. Whereas the first mode of vibration could be accurately represented by six moments, the third mode of vibration required eight. For this mode, the 4^{th} and 2^{nd} moments are the largest and have a similar magnitude.

(a) Weighted concordance: 0.779

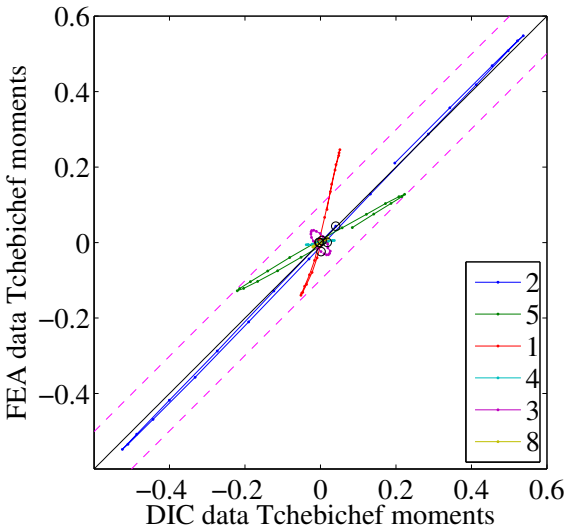

(b) Weighted concordance: 0.770

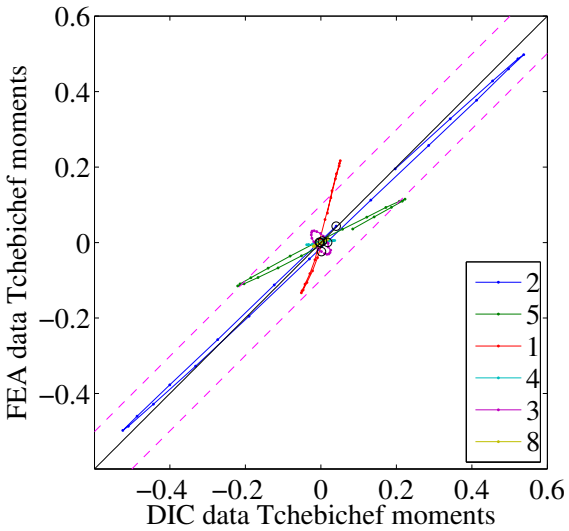

(c) Weighted concordance: 0.789

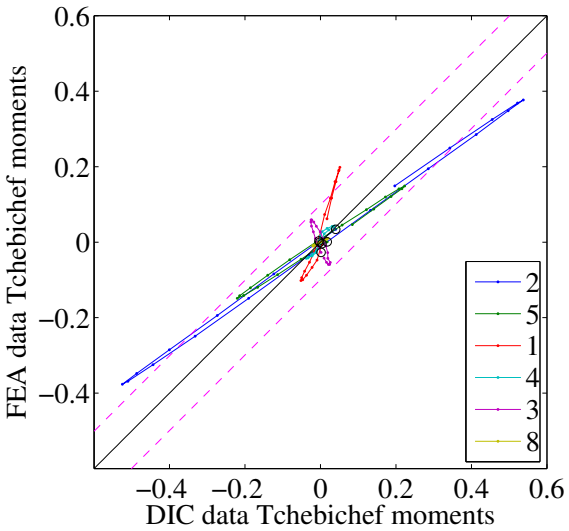

(d) Weighted concordance: 0.760

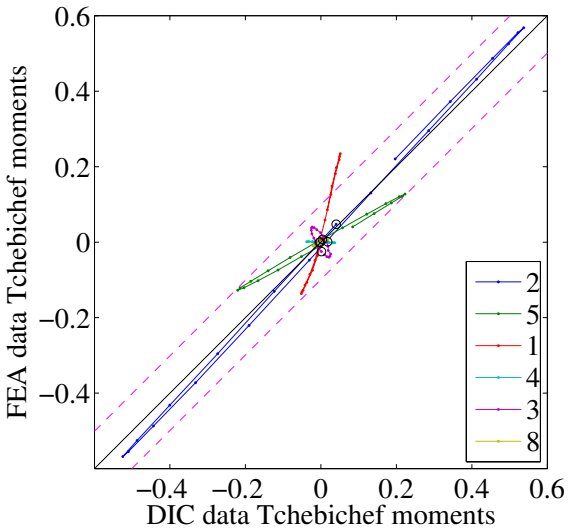

Figure 6.10: Plot of S_M against S_E for the baseline (a), constant damping (b), string constrained (c) and tetra-meshed (d) simulations of the first mode.

(a) Weighted concordance: 0.715

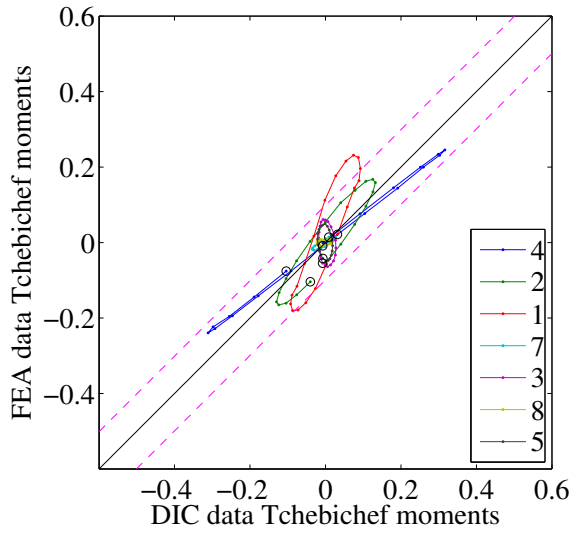

(b) Weighted concordance: 0.619

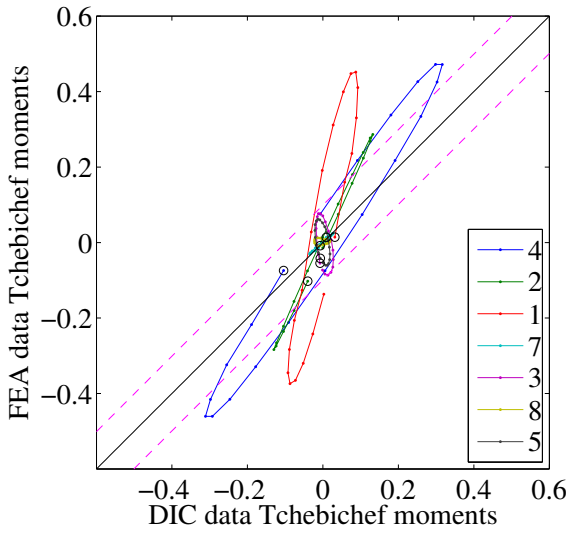

(c) Weighted concordance: 0.715

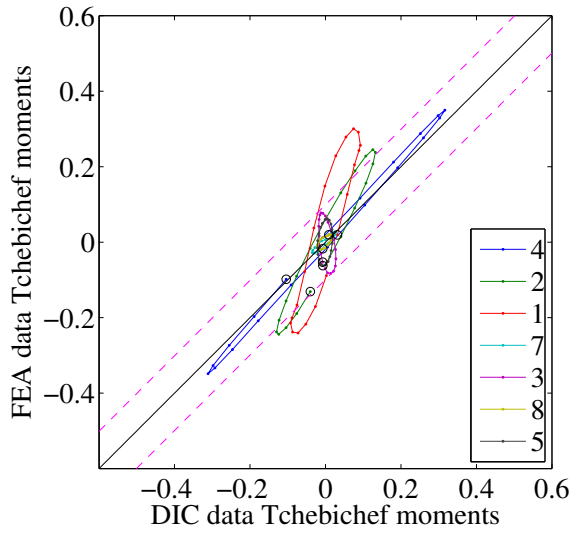

(d) Weighted concordance: 0.625

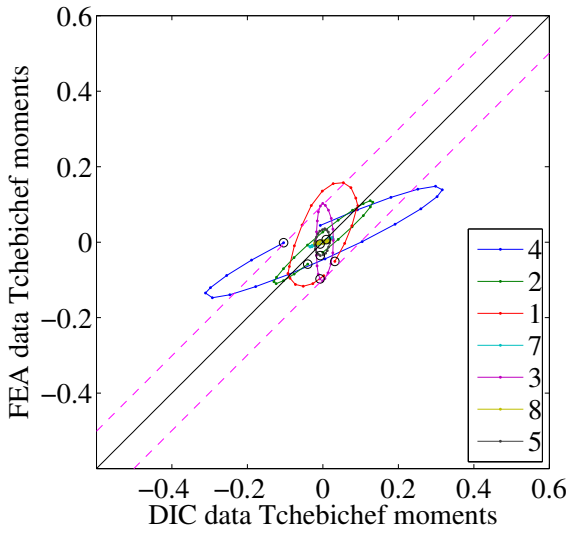

Figure 6.11: Plot of S_M against S_E for the baseline (a), constant damping (b), string constrained (c) and tetra-meshed (d) simulations for the second mode.

(a) Weighted concordance: 0.886

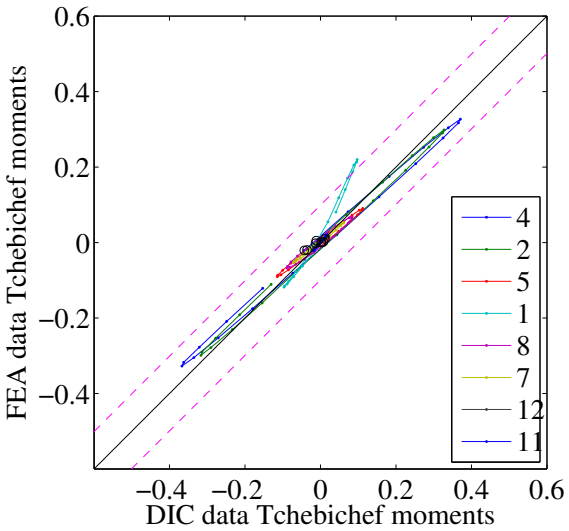

(b) Weighted concordance: 0.764

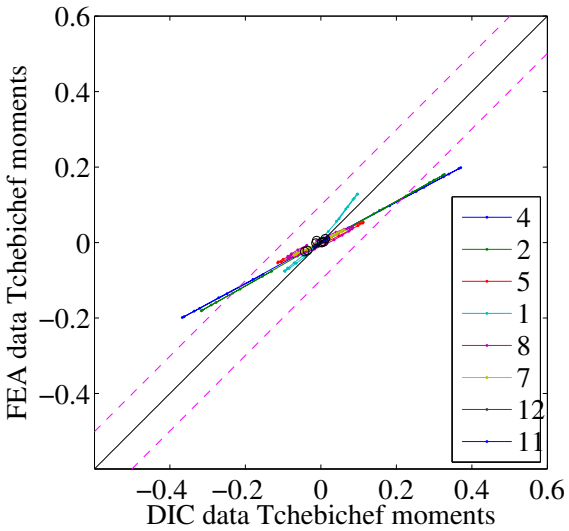

(c) Weighted concordance: 0.892

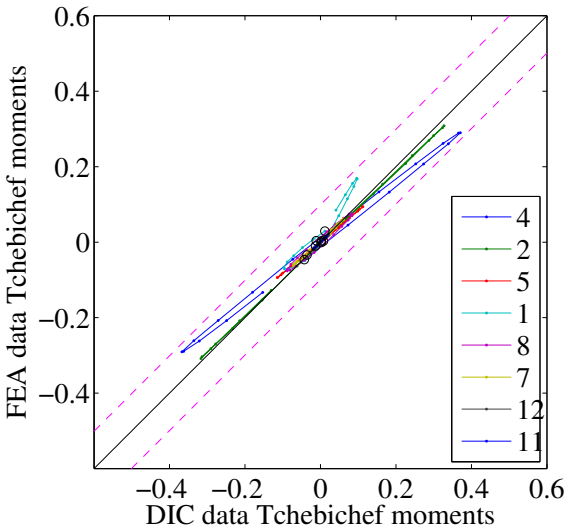

(d) Weighted concordance: 0.879

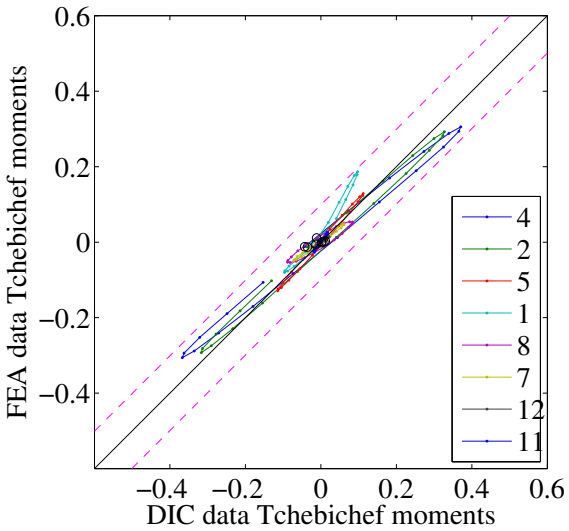

Figure 6.12: Plot of S_M against S_E for the baseline (a), the constant damping (b), the string constraints (c) and the tetra-meshed (c) simulations for the third mode.

6.5 Concordance

Lin proposed a concordance correlation coefficient that varied from -1 to 1 and gave an indication of the scatter, scale shift, and location shift when comparing two sets of data [104]. The method was developed because there was not a single test method that could characterise all of these things. The method has been applied here to compare two vectors from the image decomposition process, S_E and S_M, with means μ_E and μ_M, and standard deviations given by σ_E and σ_M.

Examples of the different cases the concordance correlation coefficient seeks to characterise are shown in figure 6.13. If there were perfect agreement between the experiment and the model, plotting the points would form a straight line of gradient unity with a zero intercept as shown in the top left figure. However, it is possible that the data could be shifted (top right) or scaled (bottom left). There could also be scatter in the data, as shown in the bottom right figure.

The concordance correlation coefficient, ρ_C, is a product of Pearson's correlation coefficient (r) and a bias correction factor (C_b).

$$\rho_C = rC_b \tag{6.8}$$

Pearson's correlation coefficient is a measure of precision which gives deviation from the best fit line when comparing two vectors,

$$r = \frac{\sigma_{EM}}{\sigma_E \sigma_M} \tag{6.9}$$

where σ_{EM} is the covariance of S_E and S_M.

The bias correction factor, C_b, is a measure of accuracy which indicates how far the best-fit line deviates from the ideal line. The correction factor is a combination of the

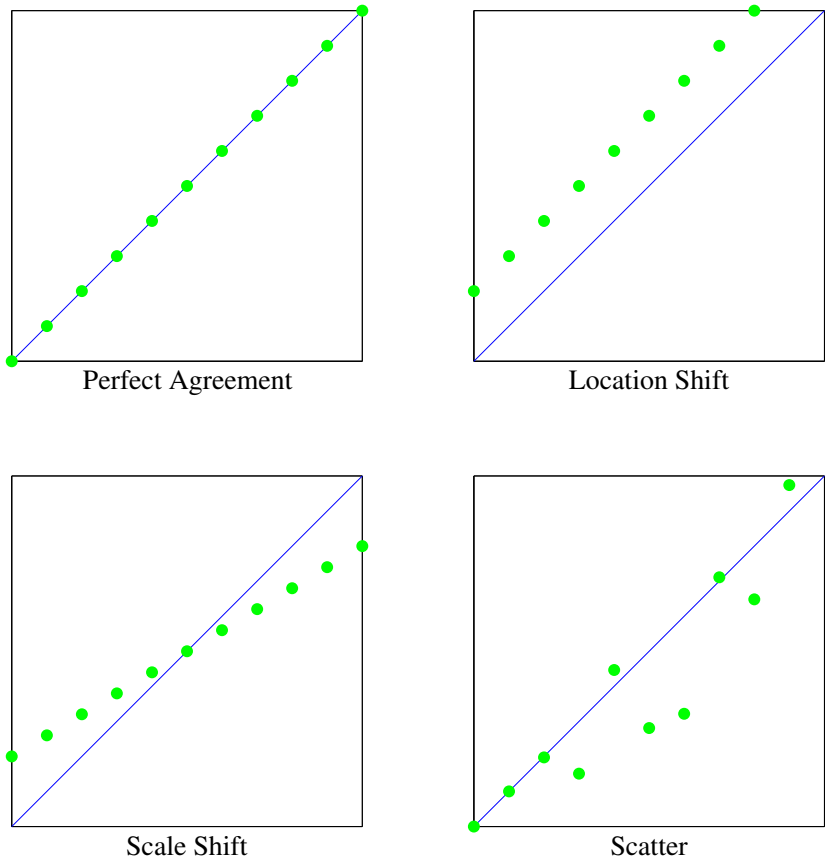

Figure 6.13: Comparison of the different cases the concordance correlation coefficient takes into account.

scale shift, v, and the location shift, τ. The bias correction factor will fall in the range $0 < C_b \leq 1$, where a value of 1 indicates perfect agreement.

$$C_b = \frac{2}{v + 1/v + \tau^2} \tag{6.10}$$

The scale shift is defined as the ratio of the standard deviations of the two data sets. This will always be a positive number, with an ideal value of 1.

$$v = \frac{\sigma_E}{\sigma_M} \tag{6.11}$$

The location shift is defined relative to the scale. It can either be negative or positive,

and will have a value of 0 when the means, μ_E and μ_M, are equal.

$$\tau = \frac{\mu_E - \mu_M}{\sqrt{\sigma_E \sigma_M}} \tag{6.12}$$

For the results presented here, a weighted concordance was defined based on the magnitude of the experimental moment, S_{Ek}:

$$\hat{\rho_C} = \frac{|S_{Ek}|}{\sum |S_E|} \rho_C \tag{6.13}$$

In this fashion each of the moments could be evaluated individually, producing a bias correction factor, scale shift, and location shift value, each of which contains valuable information about the agreement of S_E and S_M. The weighted concordance value would then give an overall indication of how well the simulation represents the experimental data.

Figures 6.14-6.16 give the results of performing a concordance analysis on the Tchebichef feature vectors. Each figure corresponds to one of the modes in figures 6.10-6.12. There are four sub-figures in each plot representing the concordance, accuracy, scale shift, and precision of the feature vectors. The first sub-figure (top left) in each set of four plots the calculated concordance values for each of the significant moments for each of the four simulations. The next sub-figure (top right) plots the accuracy, which is given as a value from 0 to 1. The third sub-figure (bottom right) plots the precision, which is given as a value from -1 to 1. The final sub-figure (bottom left) plots the scale shift, and is shown on a logarithmic scale from 0.1 to 100, with the ideal value of 1 shown as a dashed line.

At the first mode of vibration shown in figure 6.14, the concordance values are fairly consistent across the different simulation versions, with the exception of the fourth moment. The model with the additional string constraint has a much higher value than

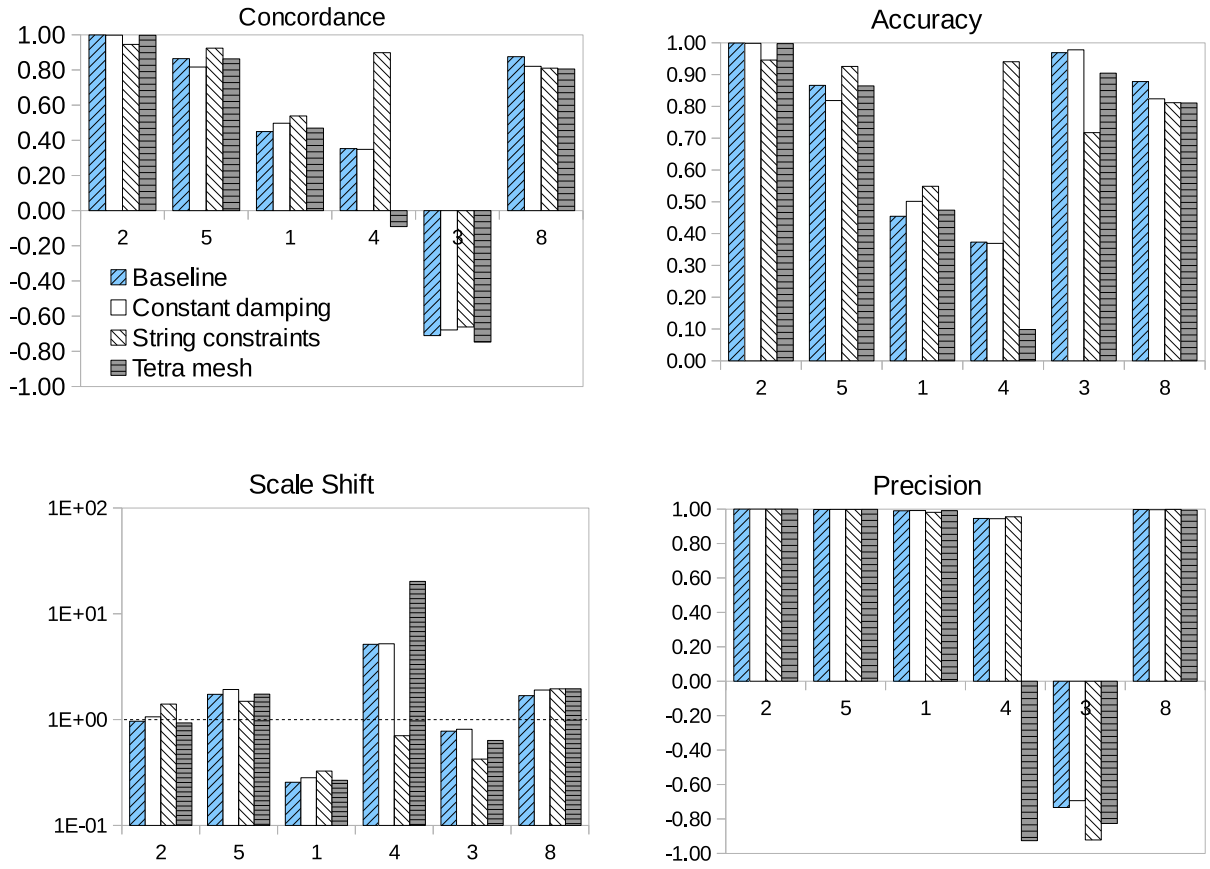

Figure 6.14: The concordance, accuracy, precision, and scale shift plots for the first mode of vibration corresponding to the results from figure 6.10.

the other simulations, while the tetra meshed simulation is the only one with a negative value.

At the second mode shown in figure 6.15 there is a fair amount of variability in the concordance values, in both the models and in the different moments. This is also true of the precision values.

The concordance values are all positive for the third mode, as shown in figure 6.16. The values are generally consistent although there is some variability between the different simulations. This is also reflected in the accuracy values, while the precision values are consistently high for all of the different simulations.

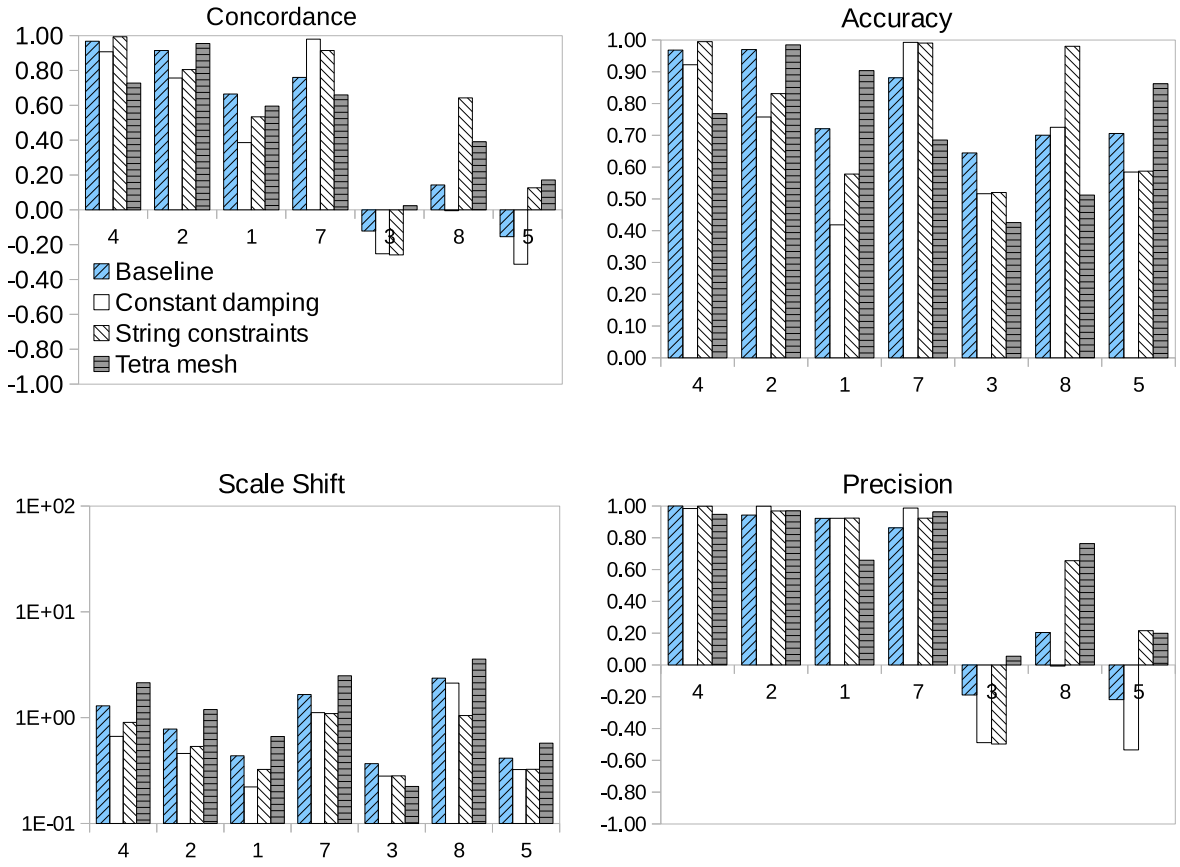

Figure 6.15: The concordance, accuracy, precision, and scale shift plots for the second mode of vibration corresponding to the results from figure 6.11.

6.6 Discussion

Ideally, the simulation would be a perfect realization of the experiment, and all of the points would lie exactly on the line defined by $S_M = S_E$. In reality however, differences between the simulation and the experiment will cause scatter of these points, as can be seen in the figures.

The expanded uncertainty was given by equation (6.7) and takes into account the minimum measurement uncertainty as well as the error in the reconstruction of the experimental data following decomposition. In this case the uncertainty is quite small, as there was only 0.9% error in the out-of-plane displacement measurement from table 6.2, and the reconstruction error was on the order of 4-5 microns. The measurement

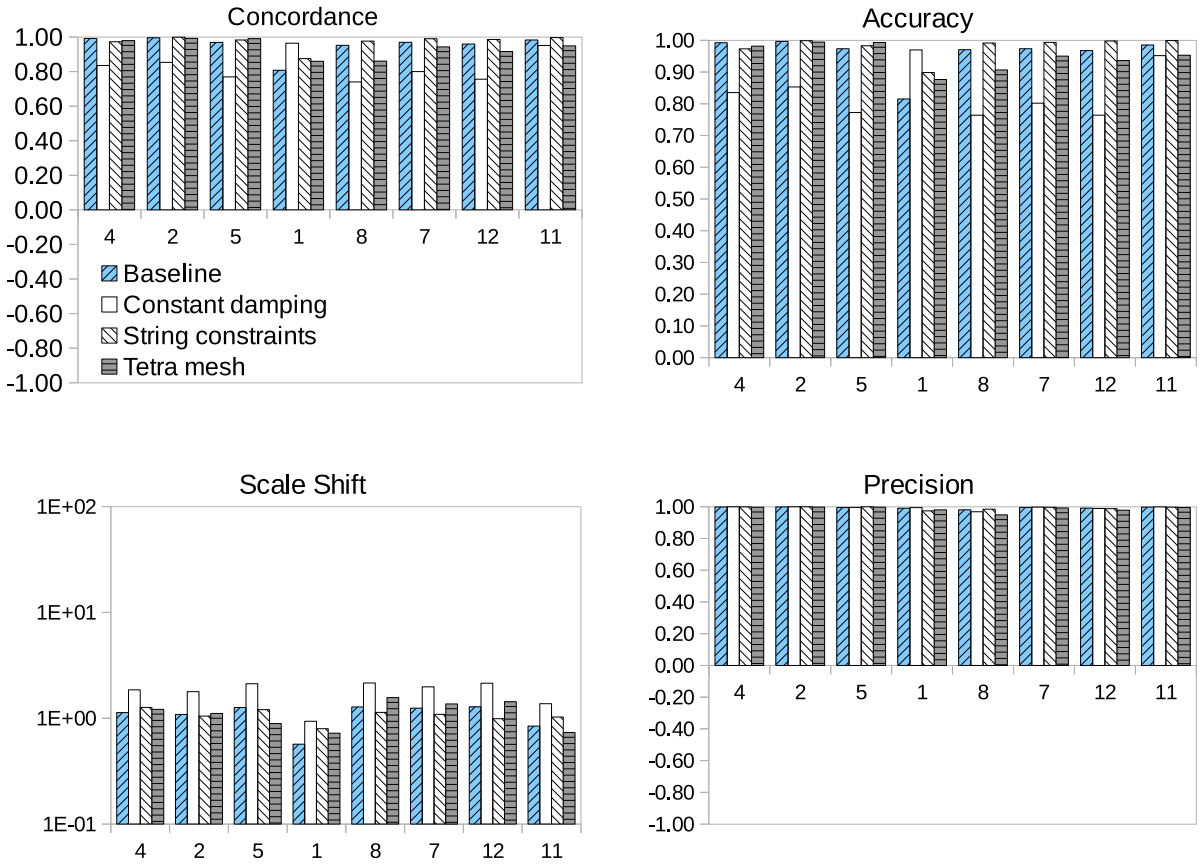

Figure 6.16: The concordance, accuracy, precision, and scale shift plots for the third mode of vibration corresponding to the results from figure 6.12.

uncertainty was calculated by multiplying the maximum displacement range measured from table 6.1 by the 0.9% relative uncertainty. This gave a total expanded uncertainty ranging from 30.0μm for the second mode to 60.4μm for the third mode. The worst case value of 60.4μm was used for the evaluation of all of the modes of vibration.

Figures 6.10-6.12 show the first few significant moments, over the entire 360 degree phase range. The dashed lines in the figures indicates the expanded uncertainty, and ideally all of the moments plotted should fall within the area bounded by these lines. Examining figure 6.10, it can be seen that none of the simulation conditions has all of the moments within the expanded uncertainty lines. The string-constrained condition appears to be the worst, as the 2^{nd} and 1^{st} moments fall outside the dashed lines, where only the 1^{st} moment falls outside for the other simulations. At this mode therefore none

of the simulation cases could be validated.

The results for the second mode of vibration, shown in figure 6.11, are similar to those for the first. None of the simulation conditions has all of the moments within the dashed lines, although the baseline has the best results with only the 1^{st} moment falling outside. The string constrained condition appears to be the worst for this mode, with three moments falling outside of the lines. Similar to the first mode, none of the simulation conditions can be validated for the second mode.

The results for the third mode of vibration, shown in figure 6.12, are the best of the three modes. For two of the four simulation conditions all of the moments fall within in the dashed lines: the string-constrained and the tetra-meshed. Therefore these two simulation can be considered to be validated for this mode. The baseline model is borderline, with the 1^{st} mode just barely falling outside one of the dashed lines.

Using the expanded uncertainty method, the simulation would only be validated for the third mode of vibration, and would require updating to obtain agreement at the other two modes. This is where the concordance correlation coefficient can provide benefit to the decision making process by providing information about the simulation conditions that were not acceptable using the expanded uncertainty. Whereas the expanded uncertainty method gives a go/no-go type of result, the concordance can help to quantify the level of confidence in a model. Figures 6.10-6.12 can be examined again looking at the weighted concordance values and in relation to the detailed concordance information in figures 6.14-6.16.

Examining figure 6.10, it can be seen that the string-constrained (c) simulation condition has the highest weighted concordance value at 0.789. This is interesting because this simulation condition has two moments that fall outside the uncertainty bands, compared to only one for some of the other conditions. Figure 6.10 provides more information about

each moment, where it can be seen that the string constrained simulation performed much better with the 4^{th} moment, which corresponds to a bend about the y-axis.The concordance values are all fairly close at this mode, ranging from 0.76 for the worst condition to 0.79 for the best.

There is more variation in the second mode of vibration, with the concordance values ranging from 0.62 to 0.72. In this case, the baseline and string-constrained models performed the best, with identical concordance values. Again, based on the uncertainty bands, it would appear the baseline simulation is the best, as only the 1^{st} moment falls outside. Looking at the detail in figure 6.11, it can be seen that the string-constrained simulation condition performed much better on the 8^{th} mode.

With the exception of the constant damping simulation condition, all of the concordance values are high for the third mode of vibration. The string-constrained simulation produced the best results, with a weighted concordance of 0.892, while the constant damping model had a value of 0.764. One interesting thing is that using the expanded uncertainty method the baseline model could not be considered to be validated because the 1^{st} moment fell slightly outside of the bands, however it has a slightly higher concordance value than the tetra-meshed simulation which was considered to be validated (0.886 vs. 0.879).

A more informed decision can be made using the information from both the expanded uncertainty and the concordance. Whereas with the expanded uncertainty approach it is left up to the judgement of the engineer to determine which condition performed the best, the concordance correlation coefficient helps to quantify the difference. Out of the four simulation conditions considered here, the string-constrained condition performed the best at all three modes of vibration. This simulation would therefore be the best choice to use, and then a decision would have to be made as to whether or not it needs to

be improved. For the third mode of vibration, all of the moments fell within the bands, and so it would not need to be updated for this mode.

To determine what aspects of the model need to be updated to improve the agreement with the experiment, quite a bit of information can be learned be examining the shape of the moment plots in more detail, as well as looking at the individual components that contribute to the concordance correlation coefficient. First is the shape of the path that the moments trace over the 360 phase range. The path is essentially an ellipse, with some of the moments almost forming a straight line, while others trace more of an oval shape. The width of the ellipse relative to the $S_M = S_E$ line appears to be related to the phase of the simulation data relative to the experimental data, and is reflected by the precision value from the concordance. The precision measures the deviation from the best fit line. This means if the shape of the ellipse is very narrow, the precision value will be high. If the ellipse is perpendicular to the $S_M = S_E$ line, then the precision value will be negative, indicating the moment is a poor representation of the experiment. If the forcing function applied to the simulation were 180 degrees out of phase with the experimental data, the moment would trace a line perpendicular to the $S_M = S_E$ line, and if they were perfectly in phase the moment would trace along the $S_M = S_E$ line. This could be useful in the identification of errors in the simulation setup, such as here when a forcing function has been applied.

A good example of this is illustrated by the baseline simulation condition (a) shown in figure 6.11. The ellipse formed by the 4^{th} moment is very nearly collapsed to the point of being a straight line, indicating that this component is in-phase between the simulation and the experiment. The 2^{nd} moment forms an ellipse that is more oval in shape, which indicates this component is out of phase between the simulation and experiment.

The second interesting thing is the angle of the major axis of the ellipse relative to

the $S_M = S_E$ line. Looking at all three sets of frequency plots, it can be seen that the moments will form a mixture of values with gradients that are less than one and greater than one. The angle is reflected in the accuracy and scale shift concordance values. The accuracy measures the deviation of the best fit line from a gradient of one. A value close to one indicates good agreement between the simulation and the experiment. However, the precision value should be taken into account first; that is if the precision value is negative a high accuracy value will be meaningless. The scale shift gives an indication of both the amount of deviation from the best fit line as well as the direction. A scale shift value of less than one indicates a gradient of greater than one, and vice-versa. If the gradient is less than one, it indicates that the values from the simulation are smaller than those from the experiment, which means that the simulation is under-predicting and could lead to a component that is not robust enough. However, if the gradient in greater than one, it means the simulation is over-predicting relative to the experiment which could lead to an overly conservative design.

A good example of this is illustrated by the 2^{nd} moment in figure 6.10. The path traced by this moment for the baseline simulation condition falls almost perfectly on the $S_M = S_E$ line, and as such has accuracy and scale shift values that are essentially one. This indicates that the simulation has accurately captured this aspect of the experiment. Examining the string-constrained condition, it can be seen that the 2^{nd} moment traces a path with a gradient less than one. This is reflected in the accuracy and scale shift values which both deviate from one.

The third thing is position of the ellipse. For most of the moments it is symmetric about the origin, indicating that the maximum and minimum values of the data are equal. However, it can be seen that some of the moments are shifted, indicating that there is some bias in that moment.

A good example of this is illustrated by the 1^{st} moment in figure 6.10. For all four of the simulation conditions, it can be seen that this moment is not symmetric about the origin, but rather that it is shifted slightly upward in the plots, indicating a bias towards the simulation.

With all of these things in mind, figures 6.10-6.12 can be examined again.

First mode of vibration, figure 6.10 At this mode, the results are dominated by the second moment, which is much larger than the three next significant moments. With the exception of the string-constrained simulation, the gradient of the second moment is close to unity for all the simulations, indicating that the simulations accurately captured this aspect of the experimental data. This is reflected in the accuracy and scale shift values in figure 6.14. The 1^{st} and 5^{th} moments are the next most significant, and they have gradients which deviate from the ideal line. The accuracy values for the 1^{st} moment are around 0.5 and for the 5^{the} moment they are around 0.85. Finally there is the 3^{rd} moment, which has a small magnitude relative to the others, but it is out of phase because of its shape. This is also reflected in the precision values, which are negative for all four of the simulation conditions.

Second mode of vibration, figure 6.11 This mode has seven significant moments, compared to six for the first mode of vibration. The largest moment is the 4^{th}, with the 1^{st} and 2^{nd} close behind. The results for the constant damping and the tetra-meshed simulation conditions look the most interesting, although they do have the lowest concordance values. The gradients of the first three significant moments for the constant damping (b) simulation condition indicates that the model is over-predicting the experiment. One possible explanation is the damping is too low, which is resulting in a higher response at this mode of vibration. The tetra-meshed model appears to be the other extreme, as the results are generally under-predicting the experiment, indicating that the

model may be too stiff. Also the ellipse of the 1^{st} moment is wide, indicating that this component of the simulation is out of phase relative to the experiment.

Third mode of vibration, figure 6.12 In general the results for this mode are good for all of the simulation conditions. There are eight significant moments for this mode, which would suggest that the results are the most complex of the three. The constant damping (b) simulation condition appears to be under-predicting at this mode, indicating that the damping is too high and resulting in a low response relative to the experiment. Also interesting to note is the slight bend in the results for the 1^{st} moment, particularly for the baseline simulation condition. As the bend occurs around the origin, this would indicate that the response in the positive and negative directions is different for this moment.

6.7 Conclusions

A novel methodology for the validation of a computational mechanics model using image decomposition and data obtained from Pulsed Laser DIC (PL-DIC) has been presented. The out-of-plane displacement of an aerospace component was captured using Pulsed Laser DIC (PL-DIC) over the entire cycle of vibration at the first three modes of vibration. The results were used to validate a modal frequency response model in which four different simulation conditions were considered. The comparison was performed by decomposing the data sets into Tchebichef moments and then plotting them against each other.

The results were assessed using the expanded uncertainty from the experiment and a concordance correlation coefficient. The expanded uncertainty approach uses the measurement uncertainty from the experiment to provide a go/no-go type of gauge to assess the data. The concordance correlation coefficient helps to quantify the quality of the model by assigning a number between -1 and 1 to the data, with perfect agreement

indicated by 1.

Based on the expanded uncertainty assessment method, it was found that only the string-constrained and tetra-meshed simulation conditions could be validated at the third mode of vibration. However, the use of the concordance correlation coefficient helped to quantify the quality of the different simulation conditions and identified the string-constrained as the best. The components of the concordance coefficient provided other useful information about the moments based on their individual shapes.

Chapter 7

High Temperature Vibration Measurements

7.1 Introduction

Digital image correlation has proven to be a very versatile measurement technique, capable of multi-scale measurements at a range of different temperatures and frequencies. Recently, the upper temperature limit of the technique has been pushed by the use of optical bandpass filters and narrow band lighting, which helps to reduce the influence of radiation from the specimen. And with the increasing quality and availability of high speed cameras, it is possible to make high-quality measurements of objects vibrating at several thousand Hertz.

However, the combined high-temperature and vibration environment is not well explored due to the difficulty of performing experiments in this extreme environment. Non-uniform thermal gradients generate internal stresses that can lead to local buckling and shifts in the natural frequencies [105]. Bailey demonstrated this behaviour analytically and numerically using 300mm square plates [106]. There have been some attempts to explore this behaviour experimentally, but complete understanding has been limited by the available measurement techniques. Virgin *et al.* performed experiments using rectangular steel plates subjected to narrow band acoustic excitation and quartz lamp heating in a progressive wave tube and measured the response using a strain gauge [107]. The

modal shifting and buckling was modelled analytically and numerically by Chen and Virgin [108]. Recently, Jeon *et al.* measured the response of a 100mm square plate to rapid thermal loading and broadband excitation using a scanning laser vibrometer [109].

This chapter seeks to address the lack of high quality experimental data by presenting some results of a combined high-temperature/vibration experiment. 3D digital image correlation was used to make measurements of two different sizes of 1 mm thick Hastelloy-X plate: 120x80 mm and 219x146 mm. The smaller plate was heated using an induction coil which could produce average temperatures in the plate of 600 °C with local areas that were 100-200 °C hotter. The larger plate was heated using quartz lamps, which provided a more even distribution but was only able to reach maximum temperatures of 500-550 °C. The measurements were made using standard CCD cameras (not high speed) by phase shifting the image acquisition relative to the excitation signal.

This work was a collaboration with the University of Illinois at Urbana-Champaign, and so the results presented here were obtained from experiments carried out in both locations. At the University of Illinois, heating of the specimen was accomplished using induction heating. For the experiments performed at the University of Liverpool, a specially-designed heating system using quartz lamps was constructed.

7.2 High temperature DIC

One of the major challenges associated with performing digital image correlation on hot objects with standard cameras and optics is the increased black body radiation that occurs. Figure 7.1 shows the amount of radiation as a function of temperature and wavelength. It is not until the temperature increases above 1000 K (727 °C) that it starts to become visible to the naked eye. However, most CCD sensors are sensitive to wavelengths outside the visible spectrum and therefore are susceptible to saturation at

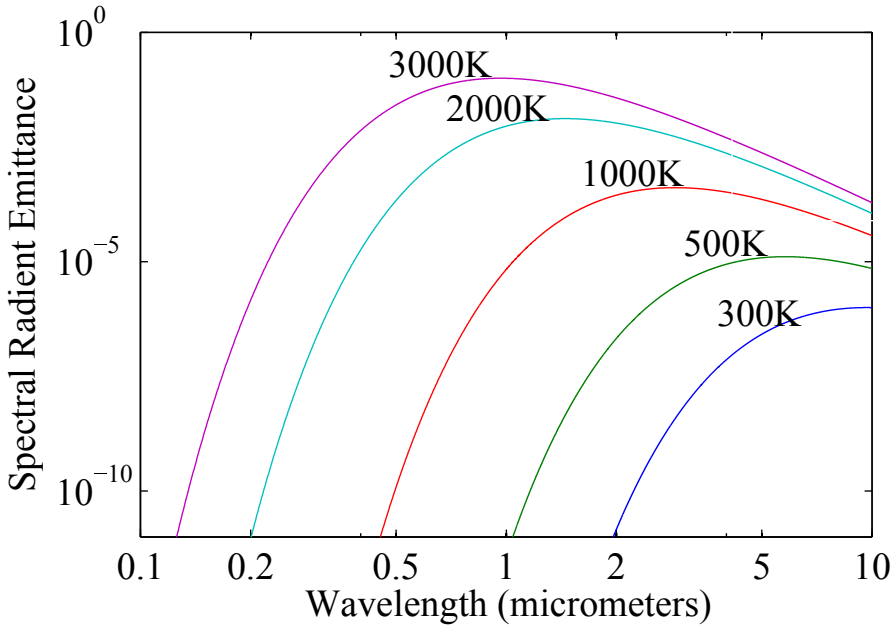

Figure 7.1: The amount of black body radiation of an object as a function of temperature and wavelength.

temperatures below 1000 K. This is the case with cameras used in these experiments, as can be seen from the plot of the sensitivity of the camera used in the induction heating experiments in figure 7.2.

It can be seen that the peak quantum efficiency is between 450-550 nm, which roughly corresponds to blue-green light. However, the sensor is able to detect wavelengths up to around 1000 nm. To counteract the effects of radiant emission by an object an optical bandbass filter was used.

An optical bandpass filter effectively allows a small portion of the electromagnetic spectrum through while blocking everything else. By choosing a filter with a short wavelength, it is possible to block out a significant amount of the radiation emitted by an object, effectively increasing the temperature capability of the system. However, as figure 7.1 shows, as an object heats up it emits more and more radiation at shorter wavelengths, which means that even with a bandpass filter there is still an upper limit to the temperature of the object that can be measured.

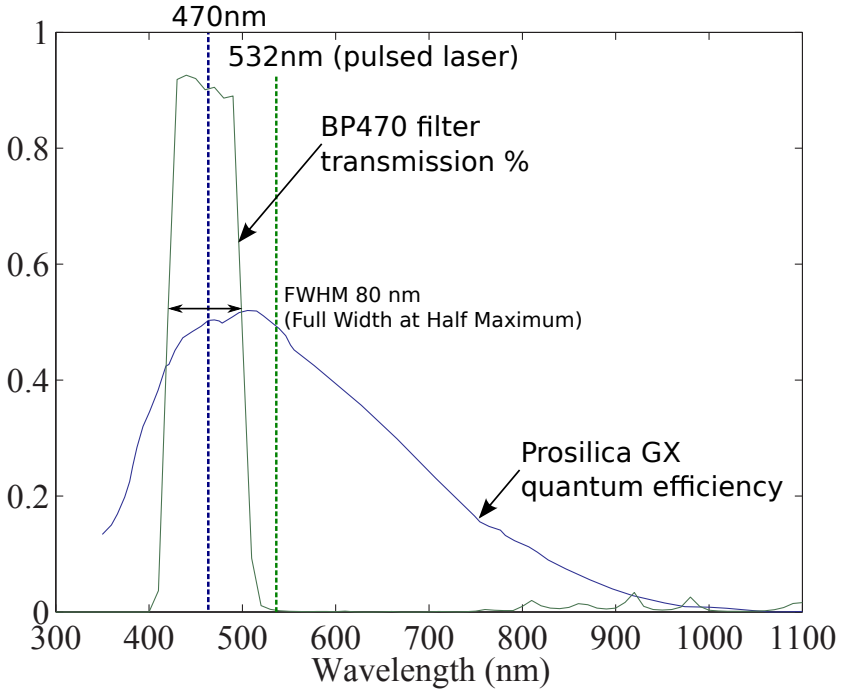

Figure 7.2: Comparison of the quantum efficiency of the CCD camera used in the induction heating experiments and the transmission efficiency of the blue bandpass filter.

Two different bandpass filters were used in these experiments. For the experiments with the induction heating a filter with a relatively short center wavelength of 470 nm was chosen. With the quartz lamp heating arrangement, the pulsed laser was used for illumination which produces light with a wavelength of 532nm. Therefore a filter with a center frequency of 532 nm was chosen.

Another major challenge is the issue associated with blurring of the images caused by the heating of the air around the plate. One way to quantify this is to capture a series of static images with the object at room temperature and a series of the object while it is being heated. These images are then processed with the DIC software and the standard deviation of the displacements calculated. Ideally this should be zero, but errors in the acquisition and processing of the images will cause it to be non-zero in reality. If there is blurring of the images, one would expect the standard deviation to increase when heating is used. Unfortunately a series of high-temperature static images was not obtained for

the induction heating setup and so this calculation was only able to be performed with the quartz lamp heating experiment.

7.3 Experiment

There were two main goals for the experiments presented here. Firstly, to develop a method to heat a Hastelloy plate to high temperatures (500+ °C). Second, to capture full-field displacement data of the high temperature plate while exciting it at resonance using 3D DIC.

To accomplish the first objective two different methods of heating were explored: induction and quartz lamps. Each method has its own benefits and drawbacks which will be discussed. The main challenge to the second objective was the application of high temperature DIC to vibration measurement. Although there has been a lot of interest in the use of DIC for high temperature measurements, it has not been applied to a high temperature vibrating component.

For the vibration aspect of the experiment, the plate was attached to a shaker by using stainless steel stinger mounted through the center of the plate. The physical attachment was made to the plate using a nut tightened on either side. A sine wave signal was sent to the shaker using a function generator. The panel was excited at resonance by tuning the frequency of the function generator. A laser vibrometer was used to help tune the frequency of vibration for the plate. By observing the response of the panel with the laser vibrometer, it was possible to get the panel vibrating at the correct frequency. This was done by observing both the magnitude and the form of the response and adjusting the driving frequency to maximize the output while at the same time ensuring it was in the form of a sinewave.

7.3.1 Induction heating setup

Induction heating was used along with the smaller plate for the experiment performed at the University of Illinois. A commercial 3D digital image correlation system (VIC3D, Correlated Solutions) based on a pair of cameras with an array size of 1024x1024 pixels was used (Prosilica GX, AVT). A matched pair of 35 mm lenses (Cinegon 1.9/35, Schneider) were mounted to the cameras. The cameras were located 480 mm apart at a distance of 790 mm from the plate. Images were captured using blue bandpass filters on the lenses and blue LED illumination (LDR2-90BL, CCS). The filters had a center frequency of 470 nm and a full width at half maximum (FWHM) of 80 nm (Midwest Optics BP470). The transmission characteristics of this filter are shown in figure 7.2 (Midwest Optics BP470). To ensure enough illumination of the specimen while using this filter, a pair of LED lights was used (CSS LDR2-90BL) which had a peak wavelength of 470 nm.

The induction heating process consists of passing an alternating current through a coil, which is placed close to, or around the workpiece to be heated. Similar to a transformer, the coil and workpiece are coupled, and electrical and thermal effects are induced in the workpiece [110]. The coils are typically fashioned from copper tubing. This allows the tube to serve as a conductor of the AC current, while cooling water can flow through the inside of the tube. For small workpieces, the coil may only be 3-4 mm in diameter or less, which means that various shapes can be easily fashioned by hand. A helical type coil in which the workpiece or specimen is encircled by several turns of the copper tube is commonly used to heat both circular and rectangular sections of metal.

The workpiece for these experiments was a thin, flat rectangular plate which necessitated a different type of coil design. This was due mainly to the need to have unobstructed optical access to the front of the plate. For this reason a pancake style coil was chosen. The first pancake coil that was created (CL-1) was fairly tightly wound and was circular

in shape, about 130mm in diameter. This size was well matched to the width of the plate (120mm), but overhung the plate by a large amount on the top and bottom. This led to much higher temperatures at the top and bottom edges of the plate which is shown in Figure 7.3.

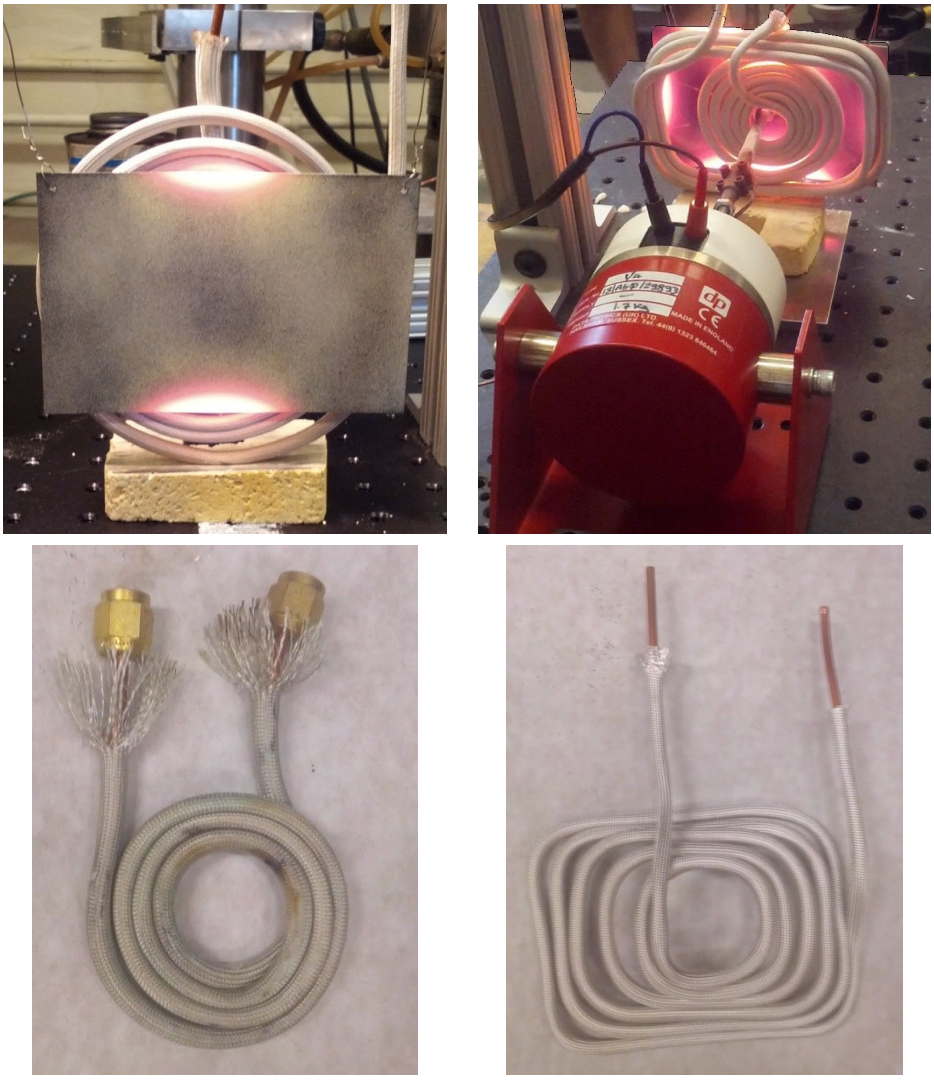

Figure 7.3: The original coil (CL-1) that created hot spots at the top and bottom edges of the plate (top left). This coil was reshaped to make it more rectangular and redesignated MOD-1 (top right). A smaller circular coil (CL-2) that did not overhang the edges (bottom left). The final iteration that gave the best results, designated RT-1 (bottom right).

While it was not necessary to obtain a perfectly uniform temperature across the surface of the plate, the coil in figure 7.3 was disproportionately heating the top and bottom of the plate causing local out-of-plane bending. As a result some modifications were made

to the coil and a couple of other designs were made to create a more uniform heating distribution. Coil CL-1 was reshaped by uncoiling the outer few turns and bending them back into a rectangular shape. The resulting heating coil and the distribution it created are shown in figure 7.3. This version was an improvement, but it still heated the edges unevenly.

In addition to reshaping the first coil, a couple of new designs were created. The first design was a smaller coil that did not overhang the edges of the plate at all. This coil is shown in figure 7.3. However this coil was too small, and was not able to heat the specimen above 400-500 °C. Another design was tried in which the coil was fashioned into a rectangle from the outside to the inside, using the size of the plate as the template to create the shape. Ultimately this coil gave the most uniform results, although it was not able to heat the specimen to as high a temperature as coil MOD-1.

To gain a better understanding of the temperature distribution in the plate, six type K thermocouples were attached along the vertical centerline of the plate using a thermocouple welder. The thermocouples were attached on both the front and back sides of the plate at the top, middle and bottom. The front of the specimen with the attached wires is shown in figure 7.4. As mounting thermocouples on both sides of the plate blocked the optical access, this experiment was performed without using the DIC system.

The plate was then heated in 100 degree increments and the temperatures recorded at each step up to a maximum setpoint of 650 °C. Feedback control of the setpoint temperature was provided by means of the thermocouple attached to the back-center of the plate. Figure 7.5 plots the temperatures measured with the thermocouples as a function of the setpoint temperature. As the back middle thermocouple was the one that was being used to control the temperature, so the measured temperature of this location matches the setpoint temperature. Ideally, if the coil were perfectly designed,

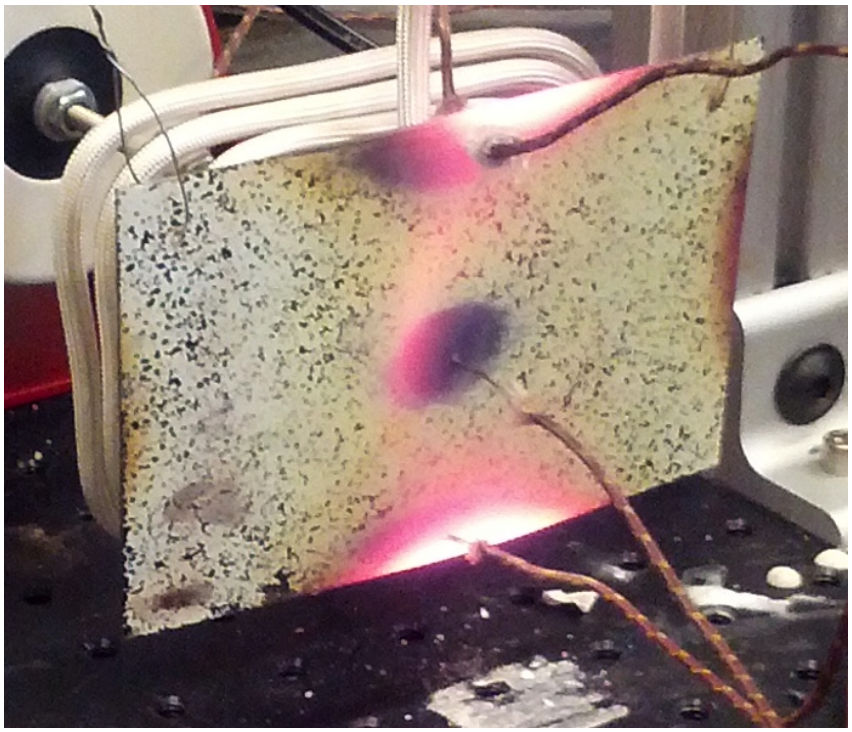

Figure 7.4: The front side of the specimen with the thermocouple wires attached. Coil RT-1 was used for this experiment.

the measured temperatures on the back would all be equal to the setpoint temperature, with the those measured on the front being a bit cooler. In reality, the temperatures at the top and bottom of the plate were much hotter than the center, with a spread of almost 200 °C between them at the 650 °C setpoint.

7.3.2 Quartz lamp setup

Quartz lamp heating was used along with the larger plate for the experiments performed at the University of Liverpool. A major advantage of quartz heating is that it can be used for any type of material, unlike induction heating, which is really only suitable for metallics. The quartz lamps are also relatively inexpensive and are easy to control. Each bulb can be controlled individually, which means that different temperature distributions can be created. In comparison to the induction heating which was used for the smaller plate specimen, quartz lamps heat primarily through radiation. To make the apparatus

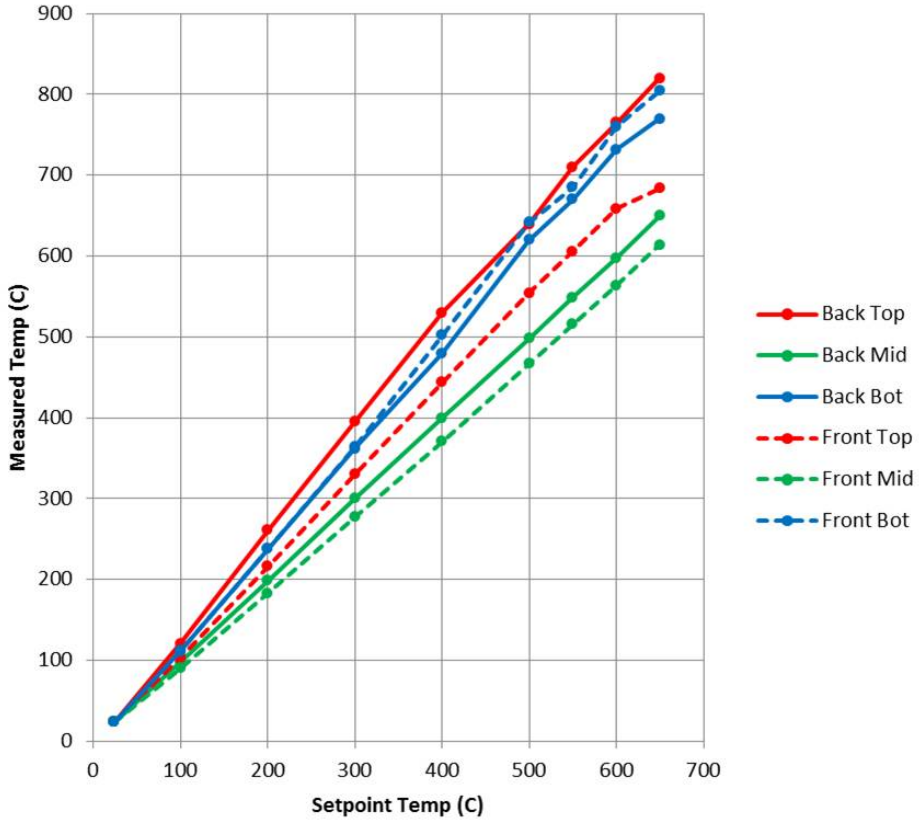

Figure 7.5: Plot of the measured temperatures against the setpoint temperature.

more flexible, it was designed as two separate banks of five lamps each. Each lamp has a power output of 1 kW at a color temperature of 3210K, giving a maximum output for the entire apparatus of 10kW. A picture of the apparatus is shown in figure 7.6. In this configuration one of the five lamps was removed to allow th estinger to pass through the middle of the bulbs, leavig a symmetric arrangement with two equally spaced lamps on either side of the stinger. The other bank of five lamps was placed at an angle and slightly to the side of the plate. This was done to permit optical access to the front of the plate for the DIC cameras and the thermal camera.

Pulsed Laser digital image correlation was used for the measurements with the quartz lamp heating. The system was based on a pair of cameras with an array size of 1624x1234 pixels (F-201b, AVT). A matched pair of 8 mm lenses (Cinegon 1.4/8, Schneider) were mounted to the cameras, providing an image magnification of 8.2 pixels/mm. The ar-

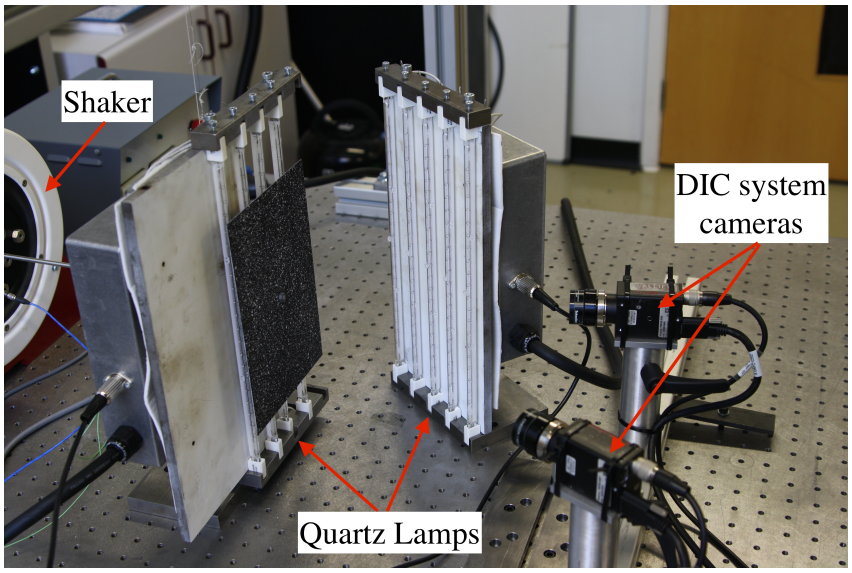

Figure 7.6: Picture of the quartz lamp heating setup with the large plate mounted to the shaker.

rangement of the cameras and their location to the plate is shown in figure 7.7. A thermal camera (SC7650, FLIR) was also used to image the surface to gather full-field temperature distribution information. The thermal camera produced images with a resolution of 320x256 pixels at 300 frames per second.

Images were captured using bandpass filters with a center wavelength of 532 nm and illumination was provided by a pulsed laser at the same wavelength. Due to the amount of light produced by the quartz lamps, it would ordinarily be difficult to place them behind the specimen and aimed into the cameras without washing out the image. An example of this can be seen in image (a) of figure 7.8. The pulsed laser produces light with a very narrow spectrum, permitting the use of a very narrow band filter. This meant that a large amount of the illumination from the quartz lamps was attenuated while all of the light from the laser was not. This can be seen in image (b), in which the plate is clearly visible while the influence of the quartz lamps has been reduced significantly.

As figure 7.6 shows, there are a bank of four lamps directly behind the plate. One of the five lamps was removed to allow the stinger to pass through the middle, leaving a

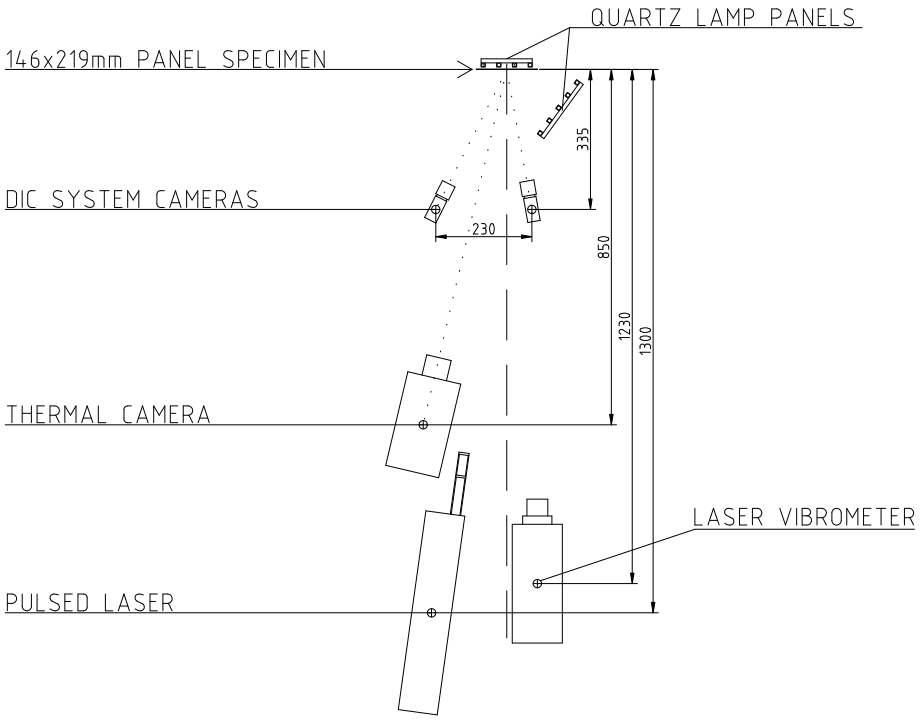

Figure 7.7: Scale drawing of the quartz lamp heating setup showing the arrangement of the different devices that were used in the experiments.

symmetric arrangement with two equally spaced lamps on either side of the stinger. The other bank of five lamps was placed at an angle and slightly to the side of the plate. This was done in order to permit optical access to the front of the plate for the DIC cameras and the thermal camera.

The DIC system cameras were placed approximately 300 mm away from the panel to simulate the standoff distance in the CEAC and SEF. The infrared camera and the pulsed laser had to be placed further away in order to be able to use them simultaneously. The laser vibrometer was located perpendicular to the plate and aimed at the corner to measure the response of the plate to the excitation.

A phase angle control circuit was implemented using a microcontroller (Arduino Nano) to vary the intensity of the lamps. For these experiments the lamps were operated in either a “low-power” or “full-power” state. At the low power state, only a portion of

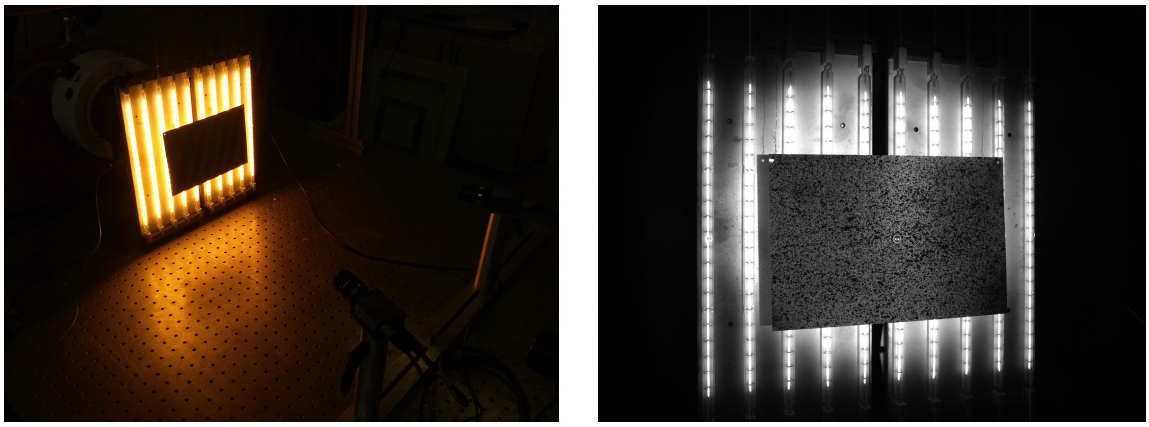

(a) Quartz heating without the laser (b) Lamps on with pulsed laser and filter

Figure 7.8: The effect of using the pulsed laser and filter on the images. Picture without the pulsed laser (a) and with the pulsed laser and bandpass filters (b).

the AC power signal is used. At full power, the entire sine wave is used and the lights emit their full power. The color spectrum will change slightly from the rated value if the lamps are not operated at full power.

Figure 7.9 shows the temperature distribution recorded in the plate using the thermal camera in several different heating configurations. In the top row of the figure, heat is applied to the back of the plate only. In the bottom row of the figure, heat is applied to both sides of the plate. For all of the DIC vibration results, heating was applied to both sides of the plate at low power corresponding to temperature distribution (c).

7.3.3 Specimen preparation

A commercially available high temperature spray paint (VHT Flameproof) in black and white colours was used to prepare the specimens for these experiments. A thin base layer of one colour was applied to the surface followed by a misting of the other to provide contrast. One of the panels sprayed this way can be seen in figure 7.3. It was determined that the spray pattern produced by using the nozzle was too fine, so an alternative method of applying the speckle was developed. A small amount of the paint was sprayed into a container and then a sponge was used to dab the paint on to the painted base colour.

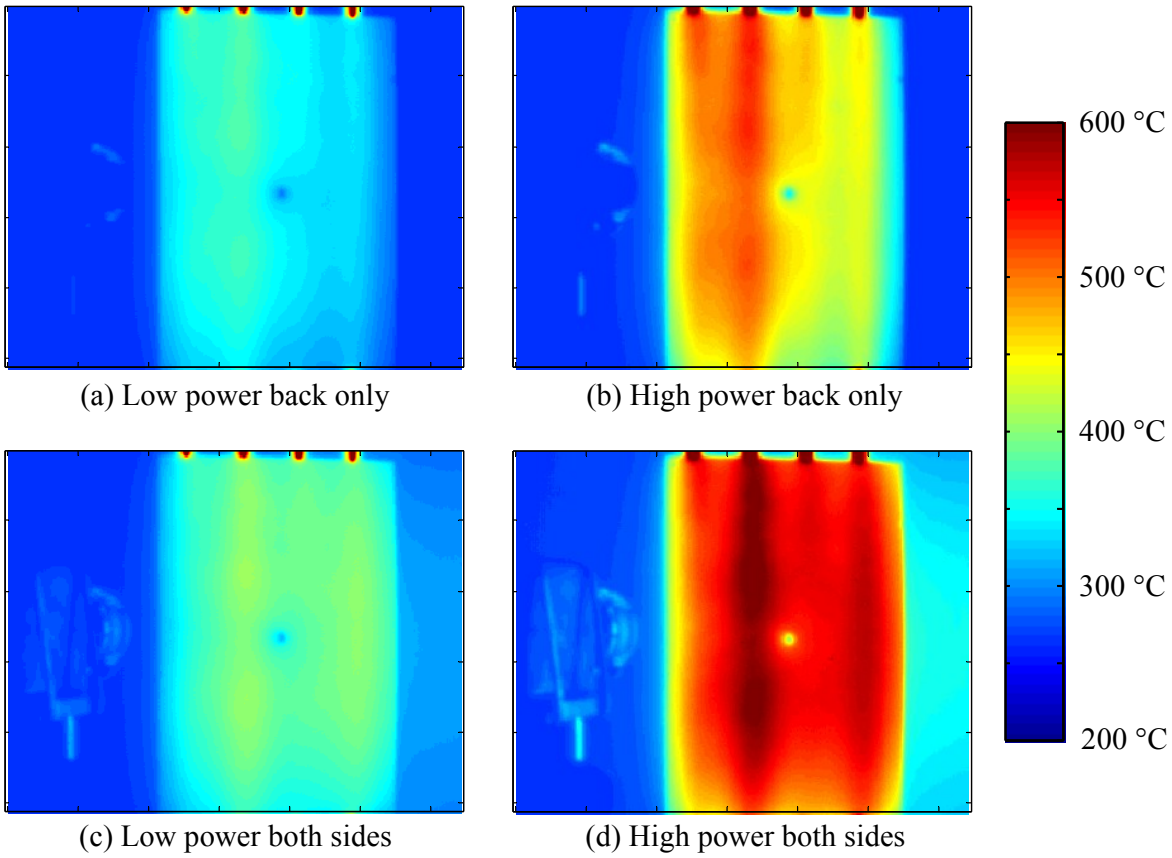

Figure 7.9: The temperature of the large plate in various heating configurations.

This produced a much larger pattern suitable for the scale of the panel as can be seen in figure 7.10.

The smaller plates used with the induction heating were prepared by applying a base with the white paint and using the black paint for the speckle. This produces good contrast and is beneficial if the illumination is limited, as the white paint is naturally more reflective. However, this was actually a disadvantage with the quartz lamp setup, as the reflectivity of the white paint kept the temperature of the plate down. To overcome this an inverted colour scheme was used in which the plate was painted black first and then a white speckle was applied. This also had the advantage of allowing the thermal camera to image the surface at the same time as the DIC system, as the black paint has a high thermal emissivity.

Another problem that was encountered was the flaking of the paint from the surface at higher temperatures as well as discoloration of the white paint. To help alleviate both the flaking and discoloration problems, the surface of the panel was lightly sanded with grit paper and cleaned using acetone. The prepped surface was immediately painted and then placed into a furnace to cure. The plate was heated to a temperature of 800 °C for 20 minutes. The furnace was then turned off and allowed to cool to room temperature.

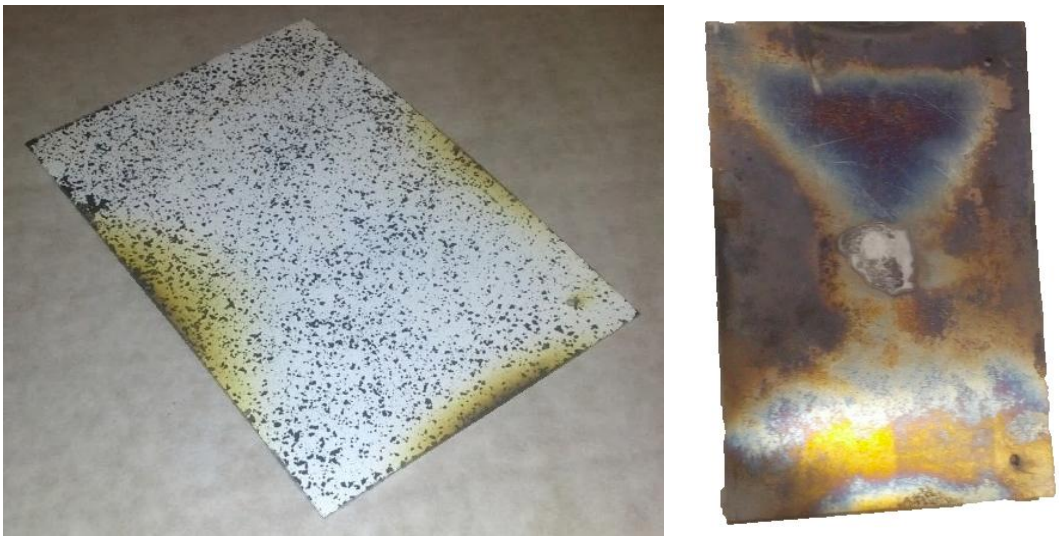

Figure 7.10: One of the small plate samples prepared by dabbing the speckle on with a sponge *(left)*. The back of the plate showing the oxidation due to heating *(right)*. Note the discolouration at the edges of the plate caused by uneven heating.

7.4 Simulation

Simulations were performed initially to aid in selecting a plate size and to design the experimental setup. A real eigenvalue analysis was performed on different plate geometries and thicknesses. This resulted in the selection of the 120x80 mm plate that was used for the induction heating and the 219x146 mm plate that was used with the quartz lamp heating. Both plates had a thickness of 0.040 in (1.016mm). The first four mode shapes for the small plate are shown in figure 7.11 and for the large plate in figure 7.12. The material properties used for the Hastelloy plate were as follows: modulus (E) 205GPa,

Poisson's ratio (v) 0.3, and density (ρ) 8.407e-9 ton/mm^3.

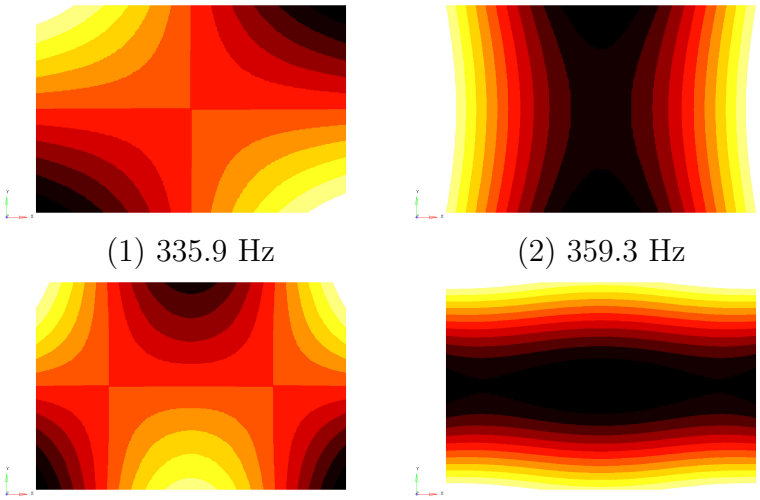

(1) 335.9 Hz (2) 359.3 Hz

(3) 774.6 Hz (4) 837.3 Hz

Figure 7.11: The first four real eigenmodes of the small Hastelloy plate.

The simulations were helpful in identifying the frequencies and mode shapes for the room temperature experiments. However, large differences between the experiment and simulation results in the natural frequencies were found at the elevated temperatures. Initially, it was thought that the change in modulus and the curvature of the plate at elevated temperature were the cause of the differences, and so were included in the model.

The curvature was relatively simple to include, as it was measured during the experiments with the 3-D DIC system. An example of the curvature measured as a result of the heating is shown in figure 7.18. The shape was imported into Matlab where a custom script was used to generate an FE mesh over the shape. A limitation of the DIC software used was that it did not output data at the edges of a plate, only for the center point of each subset. The shape data therefore did not cover the entire surface of the plate, and so extrapolation was used to generate the mesh at the edges. The mesh was then written to a text file in the format of the FE solver so it could be copied to the input file.

The temperature distribution was a bit more difficult to include in the model, as the experiments at UIUC were conducted without a thermal camera. The temperature distri-

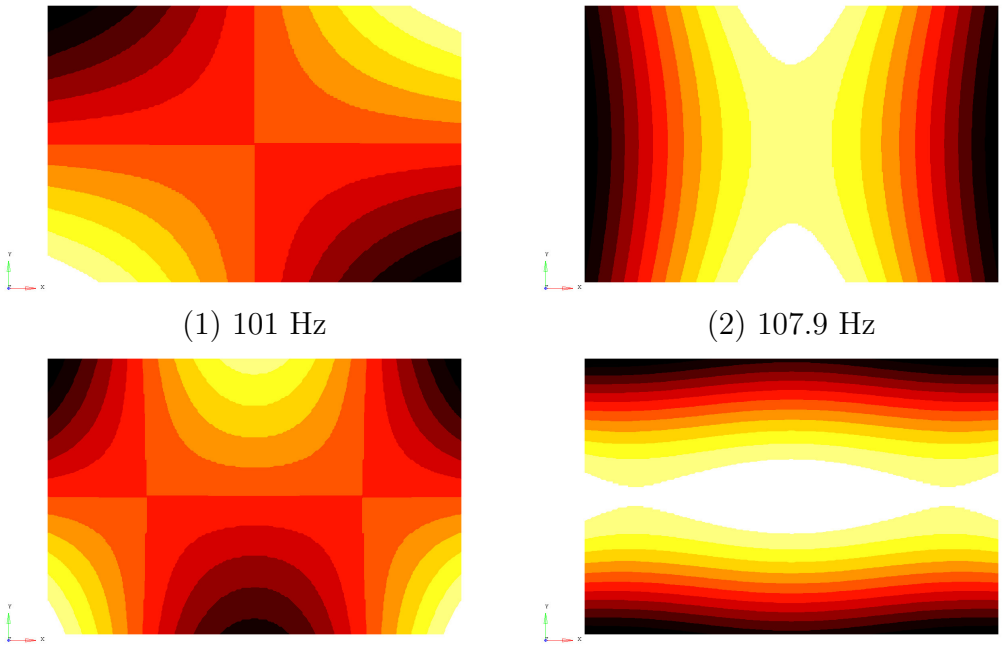

(1) 101 Hz (2) 107.9 Hz

(3) 233 Hz (4) 251.4 Hz

Figure 7.12: The first four real eigenmodes of the large Hastelloy plate.

bution was instead generated from the strain map and using the coefficient of expansion of Hastelloy (15.6e-6 m/m- °C). The temperature distribution was computed initially using ϵ_{xx} and also using ϵ_{yy}, but as they gave similar results the distribution from ϵ_{xx} was used. The temperature distribution calculated in this fashion is shown on the left (a) of figure 7.13.

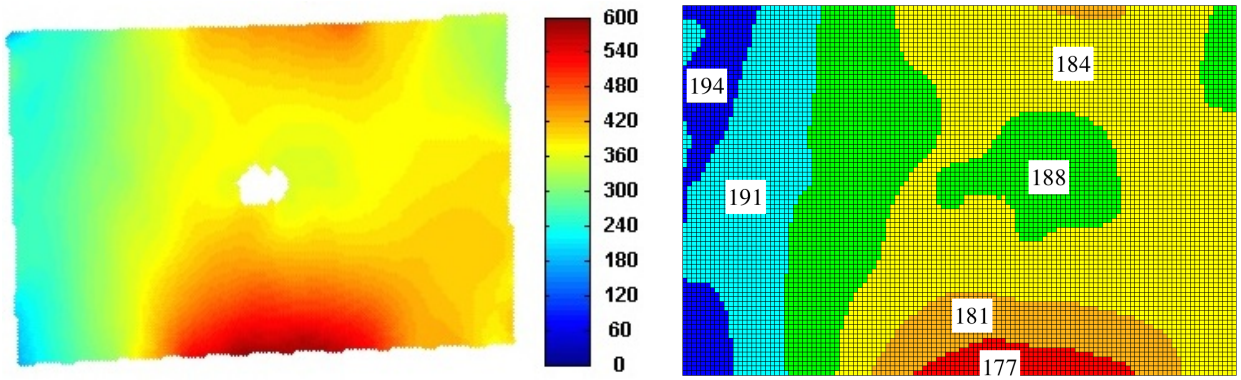

(a) Temperature from ϵ_{xx} (b) Matlab generated distribution

Figure 7.13: Comparison of the temperature distribution calculated from ϵ_{xx} (a) and the Matlab generated FE mesh with the temperature-dependent modulus values (in GPa) overlaid (b).

The stiffness (elastic modulus) of the material in the plate decreased as a function

of increasing temperature. However, as can be seen in figure 7.13, this change was not uniform. In order to approximate this behavior in the simulation it was necessary to change the stiffness of each individual element to reflect the modulus of the temperature at that point. This would be tedious to do one element at a time, so a custom Matlab script was created which could perform the change automatically. The computed temperature distribution was imported into Matlab and then divided into six zones of nominally uniform temperature, as shown on the right (b) of figure 7.13. Each of the elements in the zone was assigned the elastic modulus for that temperature range, which is shown overlaid on the figure. This method was an approximation of the actual behavior, as the change in temperature and therefore the modulus would in reality be continuous.

7.5 Results and discussion

7.5.1 Induction heating

A large amount of the initial work performed with the induction heating setup involved optimizing the coil for a more uniform temperature distribution. The results of the best performing coil are shown in figure 7.5. The thermocouple mounted to the back middle of the panel (solid green line) was used as the control signal for the induction heater so it assumed that these values should match the setpoint. At the middle of the plate there was between 5-8% difference in temperature from the back to the front, and this difference appeared to decrease as the temperature increased. The temperature at the top of the plate was the hottest, although only slightly hotter than at the bottom, and the difference between the back and the front was fairly large, as much as 17%. The difference at the bottom of the plate is of some interest due to the fact that the front side of the plate was hotter than the back, which is opposite to the other locations. This

difference was relatively small, being at most a 4.6% difference. This could have been caused by the coil extending past the bottom of the plate, resulting in stronger currents on the front face of the plate.

A series of images were captured at different temperatures using the blue light methodology described earlier. This involved placing blue filters on each of the camera lenses and using blue illumination of the plate. Images were captured from room temperature up to 600 °C and are shown in figure 7.14. The images are displayed using the Istra colormap, which increases the contrast to make it easier to see for the reader. Even with the blue light and blue filters used to capture these images, the panel is starting to get hot enough at the bottom to emit sufficient radiation to overwhelm the contrast of the image. This caused the results to de-correlate at a few spots at a temperature of 600 °C.

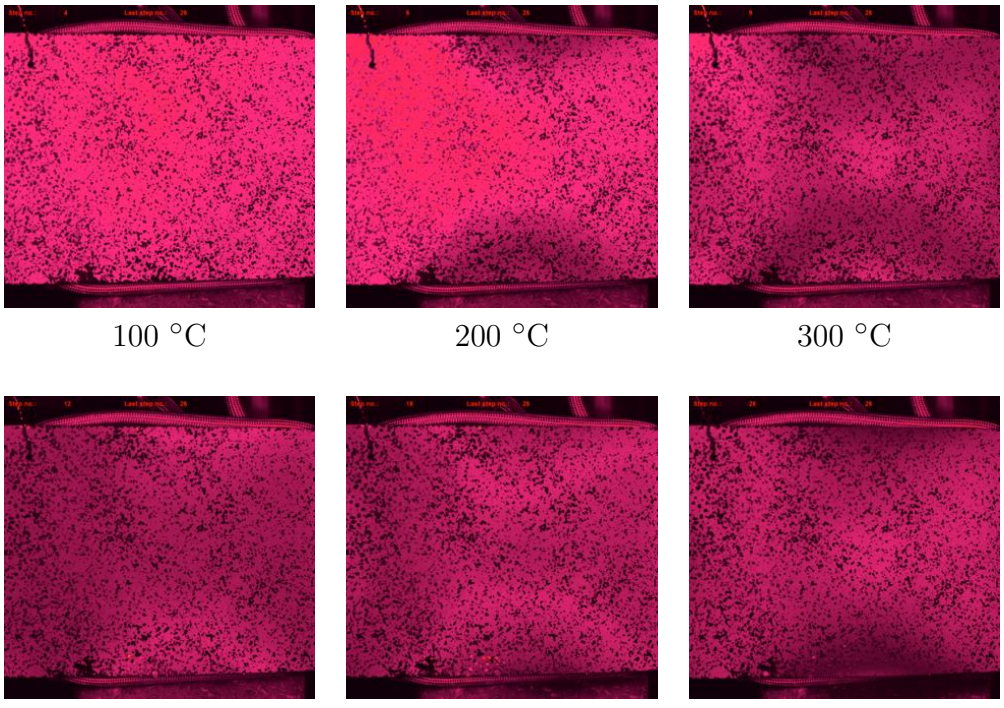

Figure 7.14: Images captured using a blue bandpass filter and blue LED lighting. Images were captured incrementally from 100 °C to 600 °C in 100 degree increments. It is possible to see the slight discoloration of the paint and the glowing at the top and bottom edges in the 600 °C image. An alternative colormap is used to increase contrast for the reader.

At about 500 °C the paint began to flake away from the surface at the bottom of the panel. It is also possible to see a reduction in contrast of the images at the hot spots at the top and bottom surfaces of the panel. This was due to discoloration of the painted surface, which occurred through a combination of oxidation and a chemical reaction of the paint with the material. This can be seen more clearly in figure 7.10. To help alleviate both the flaking and discoloration problems, a pre-heating procedure was performed (described earlier).

The out-of-plane (z-direction) displacement of the smaller plate excited at five different natural frequencies are shown in figure 7.15. The rigid body motions of the plate have been subtracted from the measured results. The plate was at a nominal temperature of 500 °C. The images were captured with an exposure time of 500 microseconds to reduce motion blur. This was the shortest possible exposure time while maintaining enough brightness in the images with the LED lights used. The images were processed using a commercial DIC code (VIC3D, Correlated Solutions) using a facet (or subset) size of 35 pixels with a spacing of 20 pixels.

7.5.2 Quartz lamp heating

In order to attempt to quantify the effects of refraction caused by heating of the air in front of the plate, a series of 10 images were captured at both room temperature and at elevated temperature. These images were then processed using a commercial DIC code (Istra4D, Dantec Dynamics) with a subset size of 35x35 pixels and an offset of 20 pixels. As there should have been no movement during the capture of the images, there should be a calculated displacement of zero in the results with no standard deviation. In reality, however, there will be errors which contribute to some calculated displacement. For the room temperature assessment, the mean calculated displacement was 10 microns with a

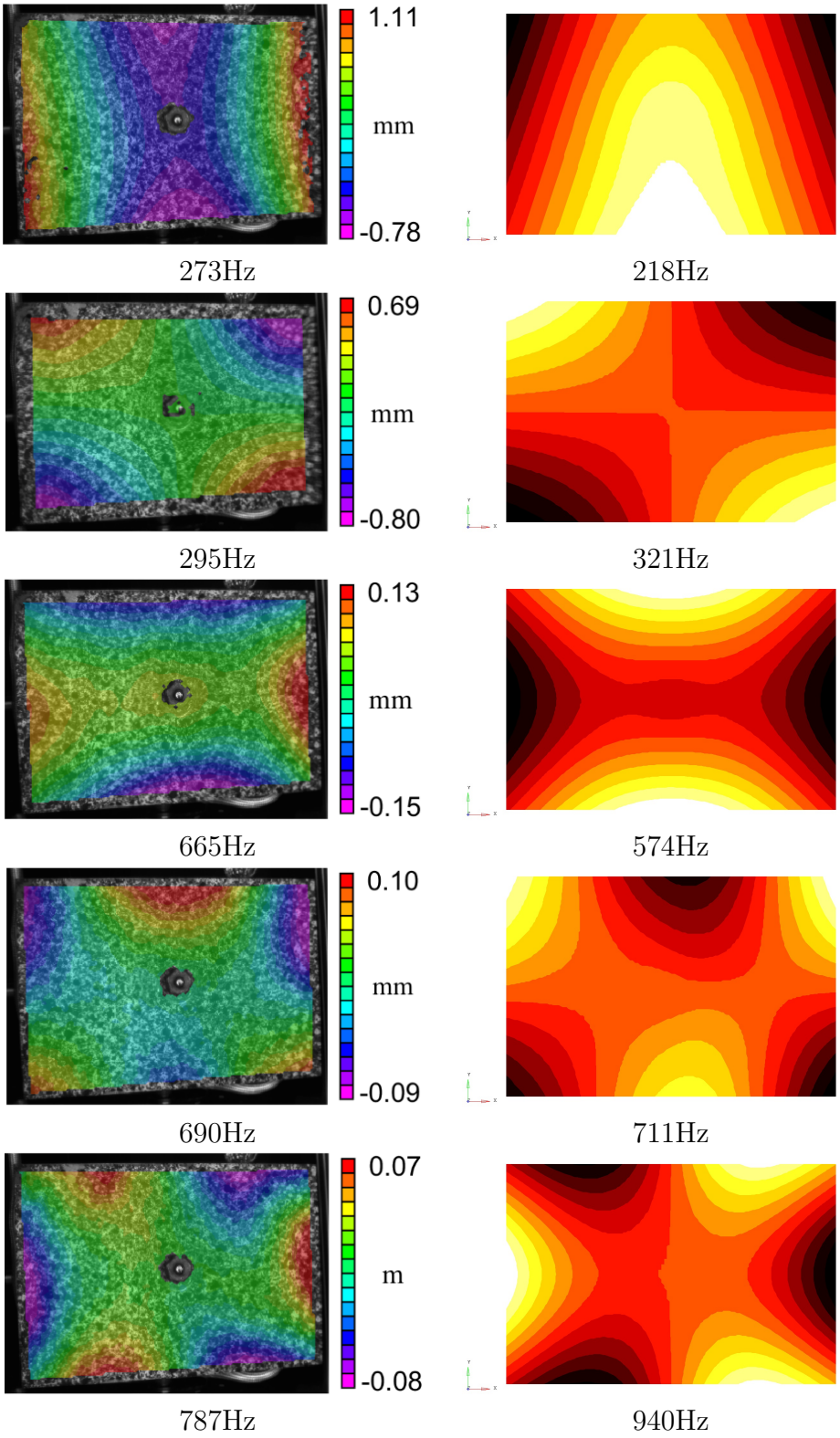

Figure 7.15: Comparison of the experimentally obtained mode shapes for the 120x80mm plate with induction heating and the predicted results from the simulation.

standard deviation of 1.3 microns. At a temperature of 590 °C (measured at the center of the plate with a type K thermocouple), the mean calculated displacement was 32 microns (0.27 pixels) with a standard deviation of 5.2 microns (0.04 pixels).

There was some difficulty taking the measurements with the plate at the elevated temperature, as the temperature is not constant. That means that there could be expansion and contraction of the plate during the course of capturing the 10 images (approximately 1 second) which could be contributing to the increased error. Nevertheless the result is still relatively low, but should be accounted for when the data is applied to the validation of computational models.

Figure 7.16 shows the frequency response function of the larger Hastelloy plate. To compute the FRF, the excitation of the plate was measured with an accelerometer that was mounted to the shaker, and the response of the plate was measured with a laser vibrometer aimed at the corner. Normally the input force would have been measured as well, but the transducer was not rated for high temperatures. The room temperature curve is shown as a dashed line, and the peaks are labelled with the frequencies. The data resulting from heating the plate with the quartz lamps at a low power setting is shown with the solid red line.

The mode shapes found from the analysis of the plate at room temperature are shown above the FRF figure. It can be seen that the frequencies from the simulation match up well with those measured experimentally. The first bending mode from both the simulation and the experiment occurs at 68 Hz and the first torsional mode also matches up at 101 Hz. There are some small differences at the higher frequencies, but there is agreement to within a few hertz. The only exception is at the measured peaks of 357 and 367 Hz, which occur vary close to each other. The simulation predicts modes at 367 and 370 Hz, so it is difficult to establish correspondence.

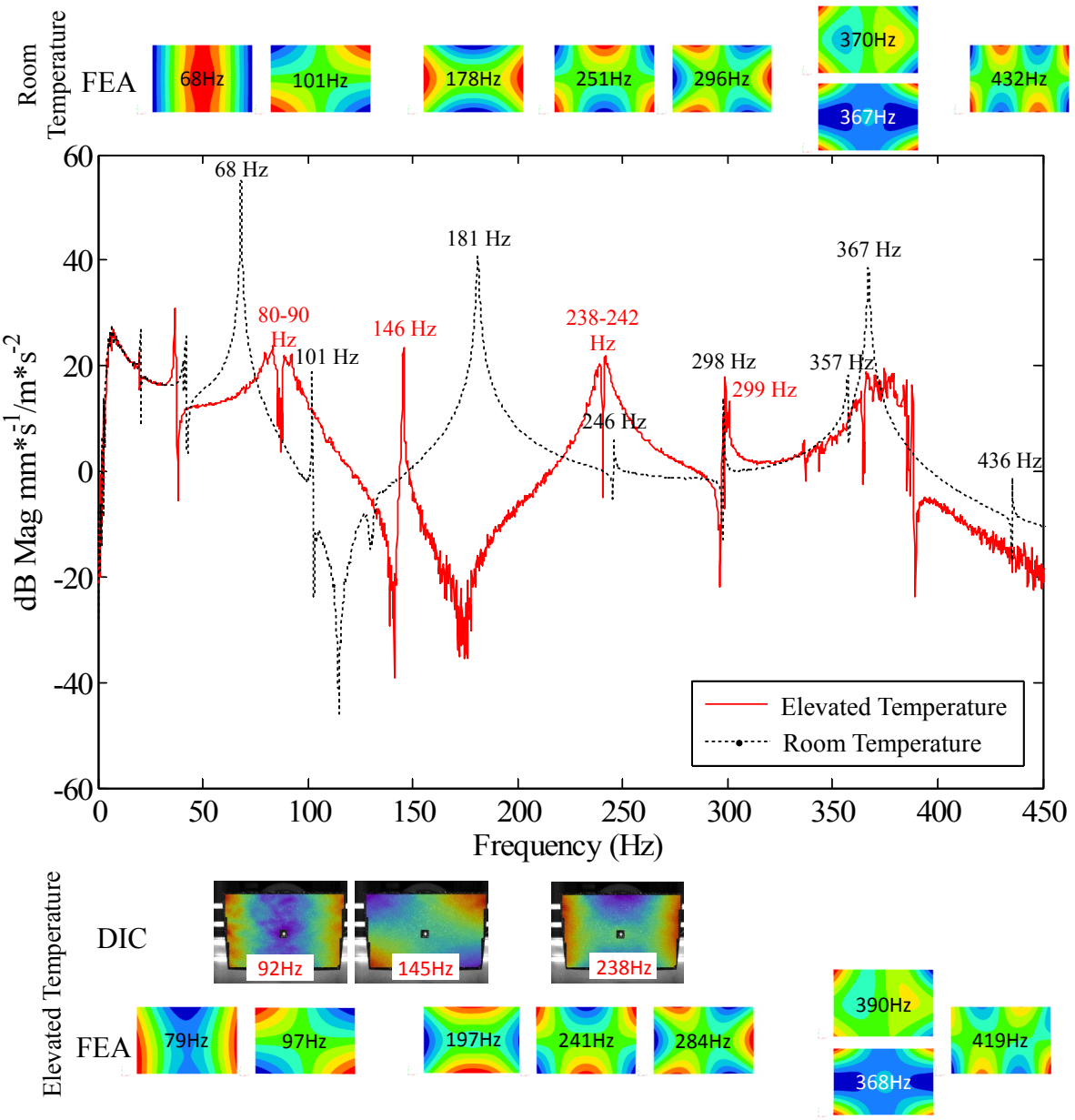

Figure 7.16: Comparison of the frequency response function for the 219x146mm plate at room temperature and elevated temperature.

The bottom row of figure 7.16 shows the mode shapes found from the high temperature simulations. While the frequencies have changed slightly from the room temperature analysis, they do not correlate as well with the FRF at elevated temperature. It is interesting to note the shape of the FRF curve at the elevated temperature relative to the room temperature curve. For a plate with free boundary conditions, one would normally expect the natural frequencies of the plate to decrease as it is heated due to a reduction in the stiffness of the material. In this figure though, it can be observed that the frequency peaks for the high temperature curve shift to higher frequencies relative to the room temperature curve. The peaks also show a shortening and widening effect which is usually caused by increased damping at elevated temperature.

It was initially thought that the curvature of the plate at elevated temperatures was the cause of the increase in the vibration frequencies. However, this was not supported by the simulations that were performed using the measured curvature. This can be seen looking at the frequencies of the simulation results compared to the measured peaks from the FRF. For example, the first torsion mode occurred at 101 Hz at room temperature but increases to 146 Hz at elevated temperature. The simulation predicts that the torsion mode occurs at 97 Hz with the addition of curvature and temperature.

This curvature can be seen in figure 7.18 and was thought to be a result of non-uniform heating through the thickness of the plate. However, the plate was actually curving towards the primary heating source (the quartz lamps directly behind the plate) which would seem to contradict the possibly that the curvature was caused by greater thermal expansion on one side of the plate than the other.

Clearly there are other factors at play that are not captured by the simple model used here. One possible explanation is that buckling occurred due to uneven heating of the plate. This is explained by Mead [105] as a statically unstable buckling mode caused

by internal stresses resulting from non-uniform heating. Mead performed simulations with several different temperature distributions, including a parabolic shape where the center of the plate is heated more than the edges. This causes the center of the plate to expand more than the edges, which form a stabilizing ring. Figure 7.17 gives vertical and horizontal cross sections of the full-field temperature map from the experiments. Three sections have been taken along each of the major axis, one through the center and one on each side of the centerline. Looking at the profiles along the major axis, it can be seen that the temperature has a parabolic shape. The parabolic heating could be causing the statically unstable buckling mode that Mead explained.

With that in mind, the contour of the plate at room temperature and at elevated temperature further supports this. A slight curvature can be seen in the plate at room temperature, this is likely due to residual stresses from the manufacturing process and the cutting process. If the plate were uniformly heated, it would maintain this shape while expanding uniformly. The combination of the slightly curved shape (from figure 7.18) with the parabolic heating distribution (from figure 7.17) causes the plate to buckle in the direction of the lamps. It should also be noted that this curvature phenomena was observed in both the induction heating and quartz lamp heating setups, but was only able to be fully explored under the more controlled conditions of the quartz setup with the aid of the thermal camera.

While the simulation was updated with the measured curvature information, the internal stresses causing the curvature were not included. Examining these results it appears that the experiments are more advanced than the simulation, and so things like the internal stresses would need to be included in the model to achieve agreement with the experiments. In addition to the simulations performed by Mead, Chen and Virgin performed some simulations to explore this phenomena, but they did not describe the heating profile

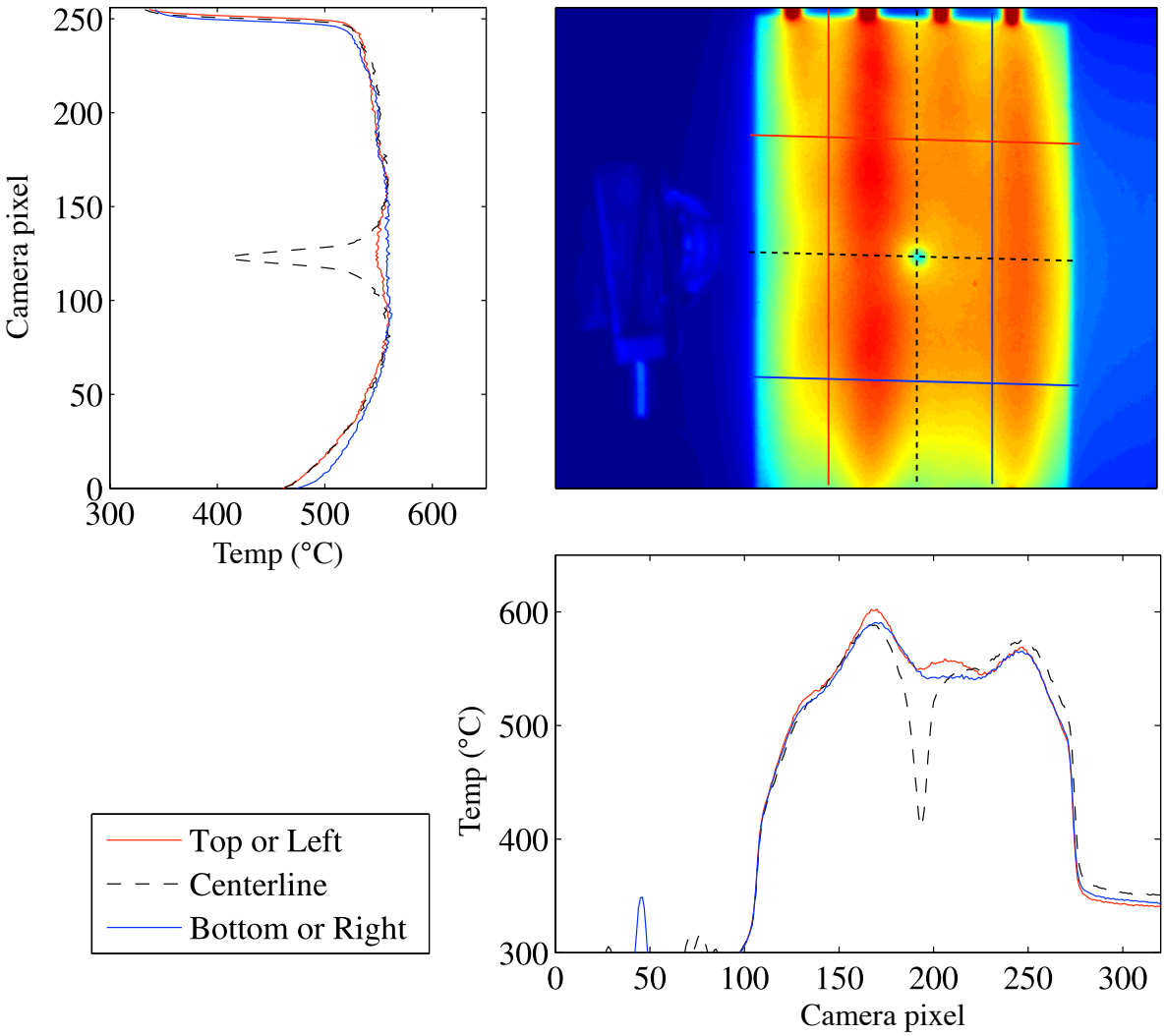

Figure 7.17: The full-field temperature map generated by the thermal camera. Vertical and horizontal sections have been cut through the map to better show the parabolic heating profile that resulted from the quartz lamp arrangement.

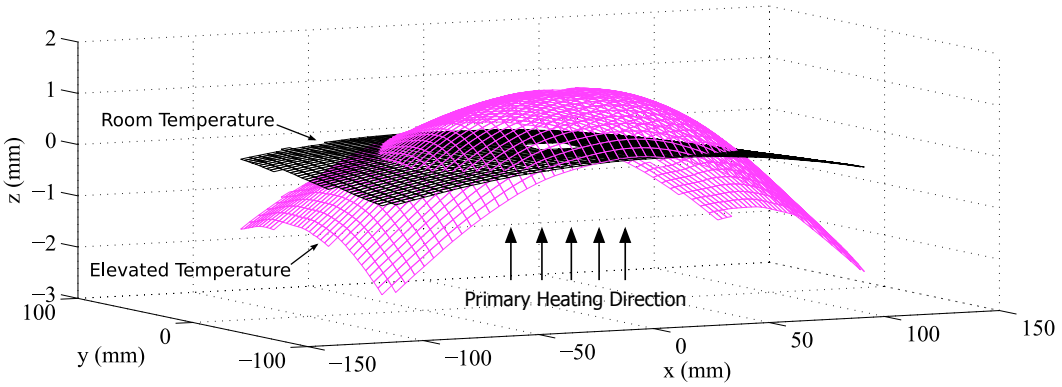

Figure 7.18: Comparison of the contour of the unheated and heated plates. The heating direction indicates the face of the plate that was oriented towards the quartz lamps.

that was applied to the plate [108]. They also used a constant modulus value despite the fact that the modulus decreases with increasing temperature. The results reported here are believed to be the first experimental evidence of full-field deformation to support the ideas described by Mead.

7.6 Conclusions

A novel methodology for making full-field displacement measurements on a panel excited at resonance at frequencies up to 1000 Hz and temperatures of 500-600 °C has been presented. Two different methods of heating a rectangular panel were explored: induction and quartz lamp heating. The induction heating was found to be very effective, and could easily heat the plate to temperatures which resulted in visible glowing. However, even after some optimization of the coil, it still tended to have hot spots at the edges. The quartz lamp heating could not reach as high temperatures as the induction heating but it produced a much more even distribution. The more controllable temperature distribution that can be achieved with the quartz lamp setup will be crucial in future experiments.

Vibration experiments were performed using a phase shifting technique to be able to capture the entire cycle of vibration of the plates using standard cameras with sampling rates on the order of 10s of Hertz. To cope with the increased blackbody radiation that occurs at elevated temperatures, bandpass filters and narrow spectrum illumination were utilized.

The frequency response function of the larger plate was obtained by using a laser vibrometer to measure the response of the plate to excitation provided by the shaker. It was found that the frequency response of the larger plate changed dramatically at higher temperatures, which was likely due to temperature induced buckling.

Simulations were conducted using the temperature distribution and measured contour

of the plate during heating. While this improved the simulation results they still did not match up perfectly with the experimental results. The simulations did not include any thermally induced stresses which likely caused the thermal buckling behaviour that was observed in the experiments, and would need to be improved to achieve agreement. With the quartz lamp setup that has been developed at the University of Liverpool, it is possible to measure the both the temperature distribution and the strains induced by the heating process. These quantities could then be included in the development of a more sophisticated model.

Chapter 8

Summary

The desire to build structures capable of operating in a combined thermal and vibration environment has motivated this research. To accomplish this a better understanding of thermoacoustic fatigue and its influence on aerospace components is needed. One of the objectives was therefore to develop a low-cost methodology to measure validation quality data during vibration loading. A low-cost system is desirable, as this would allow multiple systems to be deployed in a test of a potentially large and complex aerospace structure.

Stroboscopic illumination was considered as a potential alternative to the use of expensive high-speed cameras. One of the major advantages to using stroboscopic illumination is it permits the use of cameras with high resolution sensors. The DIC system used with the pulsed laser has a pair of 2 megapixel cameras which have approximately double the number of pixels of the high speed cameras. It is currently possible to obtain cameras with up to 5 megapixel resolution with a Firewire interface, and even higher with other types of interface. For high-speed cameras to achieve their maximum frame rates, it is necessary to reduced the resolution. This means that only a quarter (or less) of the pixels may actually be used, so there is a large difference in image quality between them and the full resolution images obtained with the Firewire cameras. The higher resolution allows for measurement of larger areas and for a lower noise floor, which makes it possible to measure smaller displacements and strains.

One of the major disadvantages to testing using stroboscopic illumination and standard cameras as compared to using high-speed cameras is that it is not possible to capture

transient responses. As was demonstrated by section 5.1, standard cameras are adequate for components that are being excited at a single frequency by using stroboscopic illumination. By phase stepping the acquisition of the images relative to the excitation signal, it is possible to capture the motion of the panel at every point during its vibration cycle. However, in the case of the Air Force's test chambers, the loading signal is random and therefore unknown. In this case it is not possible to capture all of the information about the vibration of the panel without sampling it at a frequency that is much higher than the frequencies of interest. This would mean taking measurements at a rate of 1-2 kHz, which is not possible with the 10 Hz repetition rate of the pulsed laser.

For this reason section 5.2 described an experimental setup which was modified to use the feedback from the laser vibrometer connected to a custom LabVIEW program to trigger the image acquisition at a desired point in the vibration cycle. The initial set of results discussed were taken with the displacement signal as the trigger source. This meant that the plate was at its maximum state of deformation and therefore the calculated local strain energies were quite high. As the velocity was at a local peak, this meant that the velocity was at zero, indicating that there was no kinetic energy in the plate because all of the energy was stored as deformation.

After this a set of measurements were made with the velocity as the trigger signal. The peak of the velocity signal was used to trigger the measurements, which meant that the kinetic energy as given by equation (5.1) was at a maximum. The images were captured at the zero crossing immediately following a peak in the velocity signal which corresponds to maximum stored or potential energy in the panel.

Besides the aforementioned points, there are some fundamental differences in the approaches taken by using stroboscopic illumination or high speed imaging. Beberniss *et al.* [4] captured and processed massive amounts of data in order to create a PSD to

predict the fatigue life. An alternate approach is to take less images, but with higher resolution cameras which provide better detail in the measurements. The method pursued here is to use standard cameras, which typically have lower noise and larger sensor array sizes than high speed cameras at a fraction of the cost. The lower noise and higher spatial resolution will be able to generate high quality displacement and strain maps for the purpose of validating computational mechanics models of components subjected to thermoacoustic loading.

In terms of performance, the pulsed laser system has a measurement uncertainty that is as good or better than that of a high speed system. Chapter 4 described in detail the evaluation of a commercial, high-speed DIC system that provided a benchmark against which to compare the PL-DIC system. The evaluation used a specially designed and manufactured cantilever Reference Material to produce a known out-of-plane deformation field. This deformation field was then compared with the values measured by the high-speed DIC system to determine the uncertainty. The measurements were made at three frequencies, covering a range of 126-2123 Hz and an out-of-plane displacement of $30 - 600\mu m$. The total calibration uncertainty over this range varied from $2.7\mu m$ at a frequency of 126Hz to $3.9\mu m$ at a frequency of 2123 Hz.

Section 5.4 described the evaluation of the PL-DIC using the same Reference Material and procedure as was used to assess the high-speed system. The total calibration uncertainty for the PL-DIC system varied from $2.6\mu m$ at a frequency of 126 Hz to $3.3\mu m$ at a frequency of 2123 Hz. This was an improvement over the high-speed system ranging from $0.1\mu m$ to $0.6\mu m$. This could potentially be improved further by using higher resolution cameras, which are readily available and less expensive than their high-speed counterparts.

As the ultimate goal of this project is to capture validation quality data for thermoa-

coustic loading, Chapters 6 and 7 address these items individually due to the complexity and challenges of each. Chapter 6 focused on the validation aspect while Chapter 7 addressed the high temperature, vibration aspect.

The author and his coauthors had previously developed a validation procedure which they had applied to quasi-static experiments [52]. In Chapter 6 this methodology was extended to a dynamic experiment in which data acquired over an entire cycle of vibration with the PL-DIC system of an aerospace component was used to validate a computational model. Four different simulation conditions were considered, to account for different variations in boundary conditions, damping, and element type that naturally occur in the modelling process. Image decomposition using Tchebichef moments was used to reduce the full-field data from the simulation conditions and the experiment to much smaller feature vectors. A comparison was then made throughout the entire cycle of vibration using the Tchebichef feature vectors.

The agreement between the two Tchebichef vectors was assessed using the expanded uncertainty from the experiment and also a concordance correlation coefficient. Whereas with the expanded uncertainty method only the string-constrained and tetra meshed simulation conditions were found to be acceptable at one of the modes of vibration, the concordance correlation coefficient provided more information. Using the concordance data, it was found that the string constrained simulation condition provided the best results across all of the simulation conditions at all three modes of vibration.

The difficulties associated with making DIC measurements at high temperature of a vibrating component were addressed in Chapter 7. Two different experimental setups were used to capture the motion of a Hastelloy plate subjected to combined vibration loading and nominal temperatures up to 600 °C. A small plate (120x80 mm) was used to measure vibration modes shapes up to 1000 Hz and a larger plate (219x146 mm) was

used up to 500 Hz. Simulations were created from the temperature distributions and measured curvature at high temperature.

The primary difference in the two experimental setups was the heating method. The first setup used induction heating, in which current was passed through a copper coil that was placed near the panel. The second setup used quartz lamps to heat the panel, which produced a much more even temperature distribution, but was not able to get the panel as hot as the induction heating.

During the heating process in the experiments, a buckling phenomena was observed in the Hastelloy plates. This buckling phenomena is described in the literature [105, 106, 107], but has not been very well explored experimentally, and not with the full-field measurement methods currently available.

Chapter 9

Conclusions

The research presented in this thesis has been performed over the course of three years under funding from the European Office of the United States Air Force (EAORD) as a part of a long-term project to collect high quality data for the validation of computational mechanics models of thermoacoustic loading. To that end, several major advances have been made as a part of this research, and a clear direction has been established for the future. The major contributions presented in this thesis are as follows:

A relatively low cost, high spatial resolution approach to capturing images, from which to evaluate strain fields using digital image correlation, has been designed and implemented in the Pulsed Laser DIC system. This system has the capability to make in-plane and out-of-plane measurements over a wide range of frequencies (10-2000+ Hz) and displacements (10s of microns to several mm). A novel triggering system and software has been developed which uses feedback from a laser vibrometer to permit the use of the PL-DIC system with a random excitation signal. The system uses standard machine vision cameras, which is a massive advantage compared to high speed cameras. Machine vision cameras are smaller, less expensive, and available with higher resolution sensors. High speed cameras are also currently unavailable in UV versions, which will be necessary to operate at very high temperatures.

The measurement uncertainty in the Pulsed Laser DIC system was evaluated and benchmarked against a more traditional High Speed DIC system. A cantilever Reference Material was excited at its first three bending modes (126, 796,

and 2123 Hz) and the out-of-plane displacement (30-600 microns) measured with the two systems. The maximum uncertainty for the PL-DIC system was 3.4 microns, compared to 3.9 microns for the High Speed system. It is believed that this could be reduced further by using higher resolution cameras, which are readily available.

A validation has been performed of a computational mechanics model of a prototype aerospace component using data captured with the Pulsed Laser DIC system. A novel method was used to compare data from four different simulation conditions over the entire cycle of vibration using Tchebichef decomposition. The measurement uncertainty for the system was used to assess whether or not the simulation was a good realization of the experiment. For the first time a simulation was assessed using a concordance correlation coefficient, which assigns a value ranging from -1 to 1, with a value of 1 indicating perfect agreement. Using the measurement uncertainty criteria, it was found that the baseline and string constrained simulations were acceptable. However, the concordance correlation coefficient had a higher value (0.789 vs. 0.779) for the string constrained simulation, indicating that it was the best realization of the experiment.

An experimental apparatus for high temperature work has been designed and established and results obtained which using PL-DIC. Based on successful experiments performed in collaboration with the University of Illinois at Urbana-Champaign, a high temperature apparatus which uses quartz lamps for heating was designed and built. A major advantage of the quartz lamps is the temperature distribution can be more precisely controlled, which will be critical for planned future experiments. The Pulsed Laser DIC system was used in conjunction with a green bandpass filter to capture images of the vibrating panel at a temperature of 600 °C. Using this system, a phenomenon was observed which was described by Mead as a statically unstable buckling mode caused by internal stresses resulting from non-uniform heating [105]. There is

limited literature on the use DIC at high temperature for dynamic measurements, and it believed that the results presented here are the first application of vibration measurement and the first to observe the buckling phenomenon with full-field results.

9.1 Further work

The PL-DIC with quartz lamp heating available in the experimental apparatus created as a part of this thesis has massive potential for future exploration of the complicated thermoacoustic response of panels. The thermal buckling phenomenon which was discussed in Chapter 7 will be explored further and compared to the analytical predictions in the literature. Specifically, it desired to have a rigorous relationship relating temperature and vibration frequency to the buckling phenomenon. To accomplish this the simulation will need to be improved by including the effects of the thermally induced stresses in the plate.

There is also potential to explore the use of Thermoelastic Stress Analysis (TSA) with random vibration. Some preliminary results have been obtained using the quartz lamp heating apparatus described in Chapter 7. Previous high temperature work in TSA has been performed in specially designed ovens to minimize thermal gradients [111]. It is believed that the results shown here are the first at high temperature without the use of such an furnace. One of the major advantages of TSA is that it has a relatively easy setup that doesn't need to be done in a controlled lab environment. However this is not the case for high temperature, as thermal gradients and reflections must be carefully controlled. It should be possible to circumvent this requirement by using image processing techniques to filter out the gradient effects, thereby permitting the use of TSA at high temperature in real-world applications.

APPENDICES

Appendix A

Airbus Panel Drawing

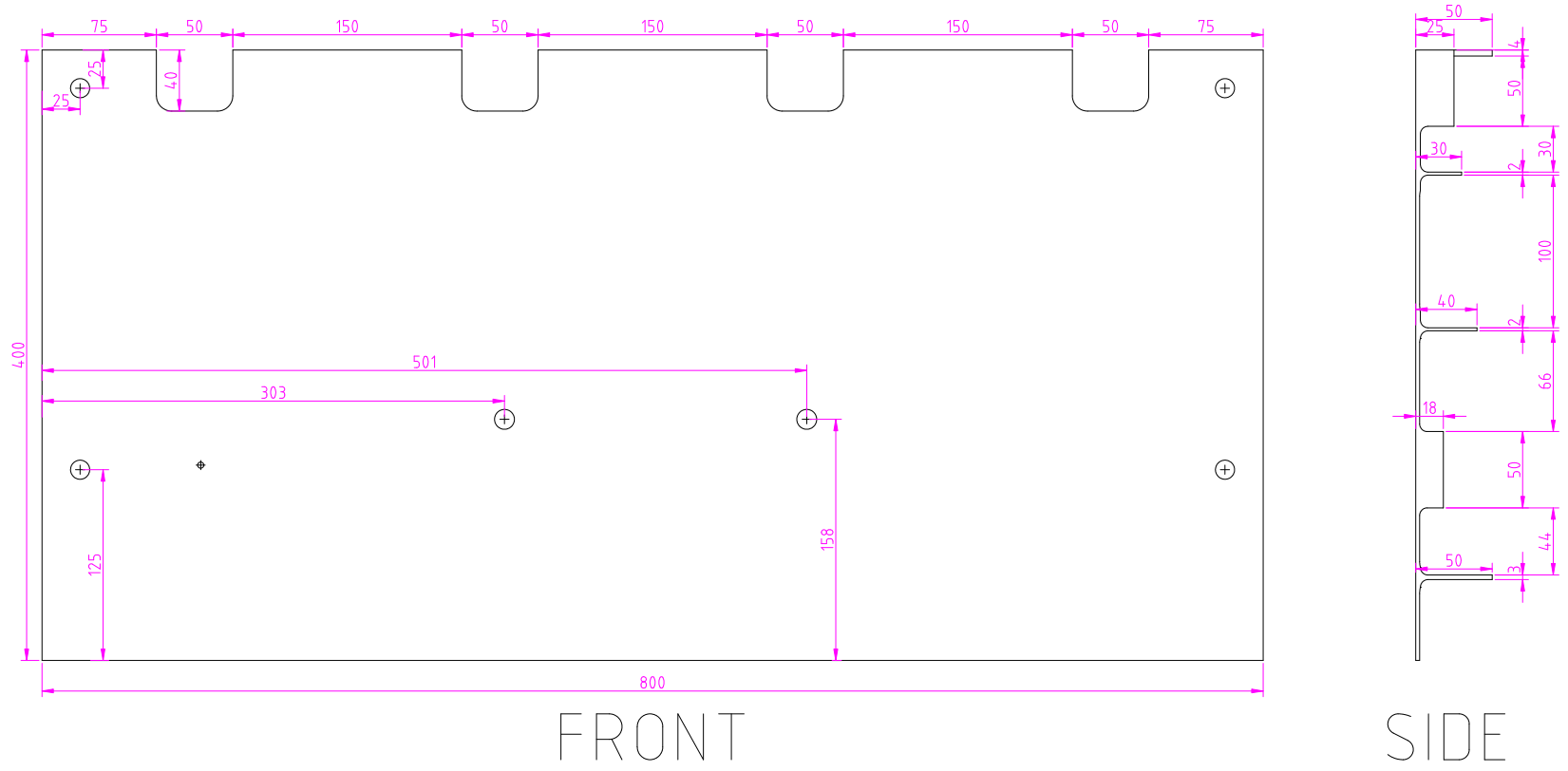

Figure A.1: Drawing of the airbus panel

Appendix B

Airbus Panel Mode Shapes

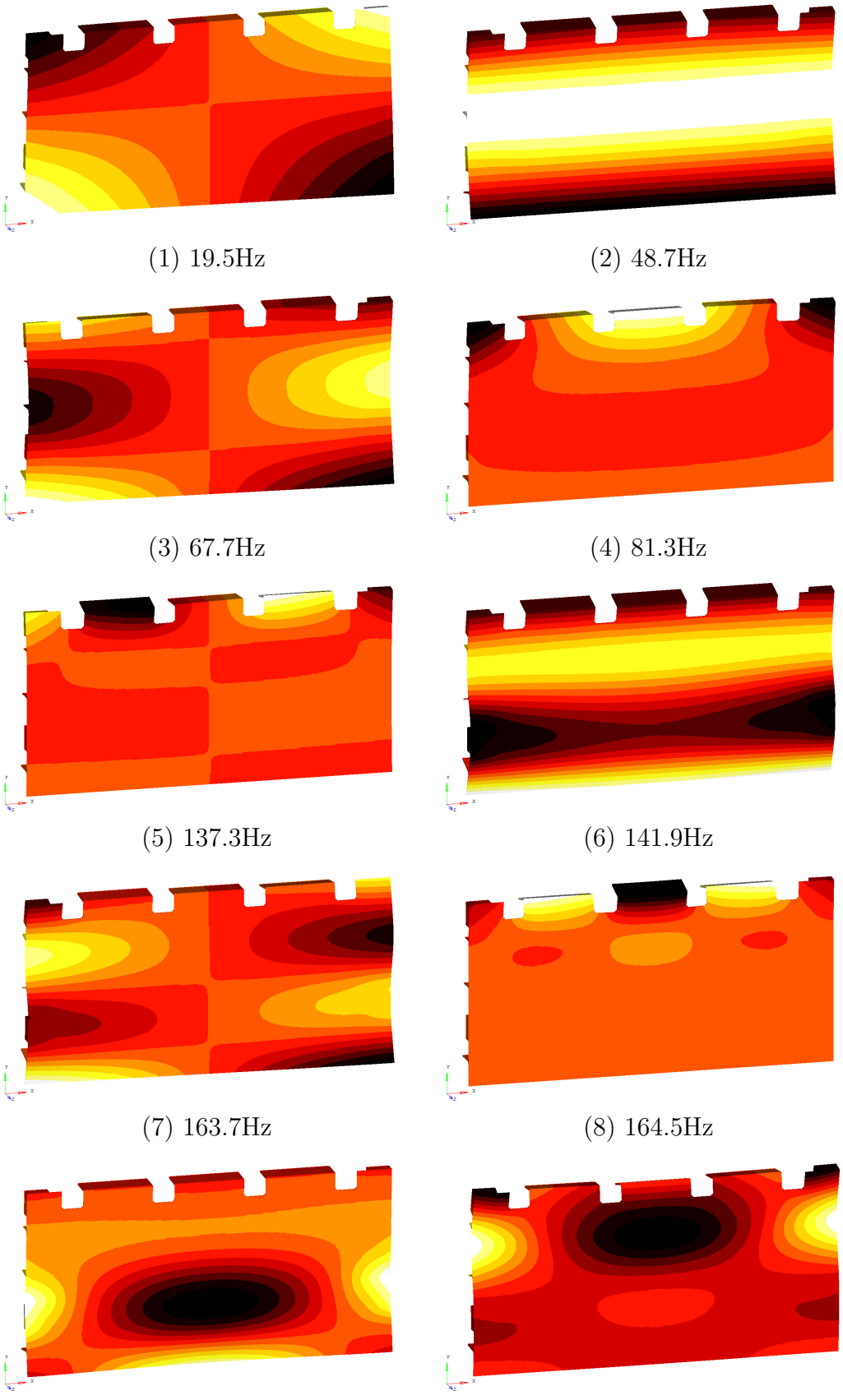

(1) 19.5Hz (2) 48.7Hz

(3) 67.7Hz (4) 81.3Hz

(5) 137.3Hz (6) 141.9Hz

(7) 163.7Hz (8) 164.5Hz

(9) 185.3Hz (10) 242.8Hz

Figure B.1: Real eigenmodes 1-10 of the aerospace component simulation.

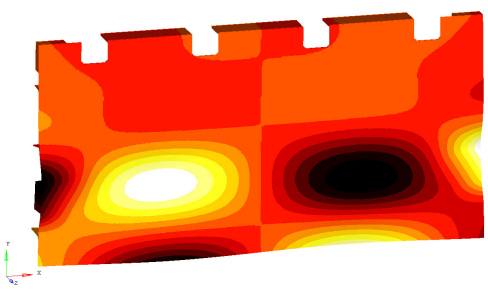

(11) 275.4Hz

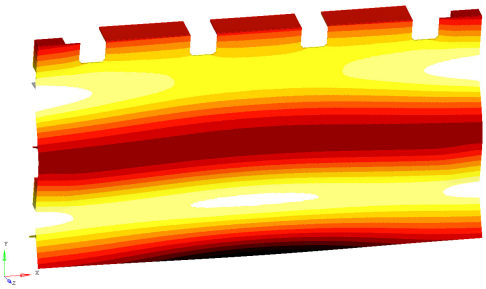

(12) 279.2Hz

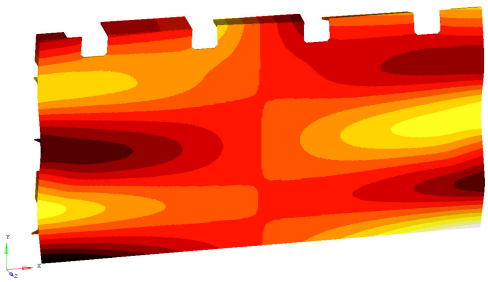

(13) 291.1Hz

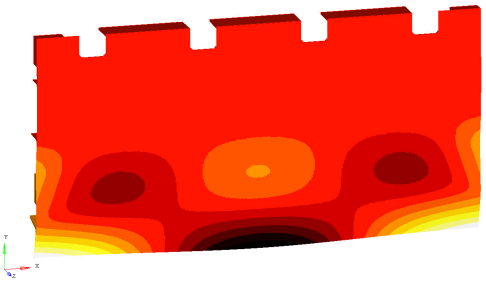

(14) 303.5Hz

(15) 306.9Hz

(16) 344Hz

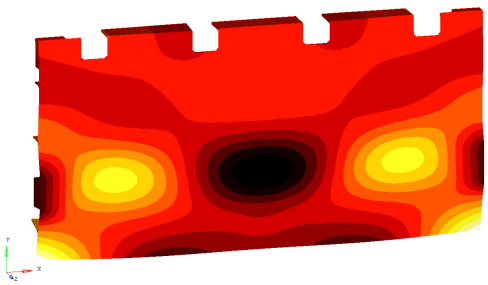

(17) 364.8Hz

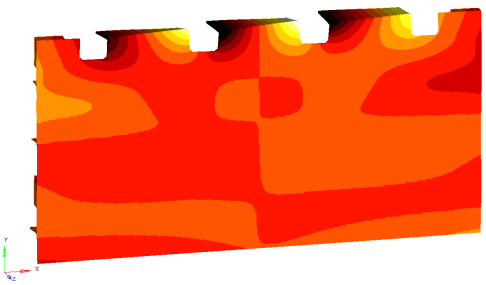

(18) 384.8Hz

Figure B.2: Real eigenmodes 11-18 of the aerospace component simulation.

Appendix C

Hastelloy Plate Mode Shapes

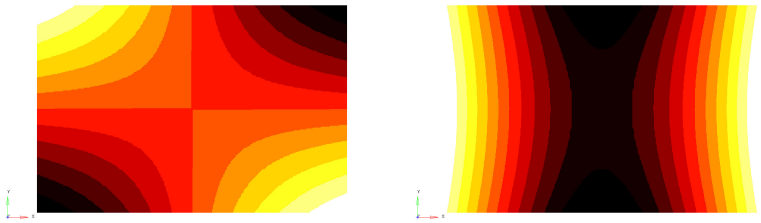

(1) 335.9Hz

(2) 359.3Hz

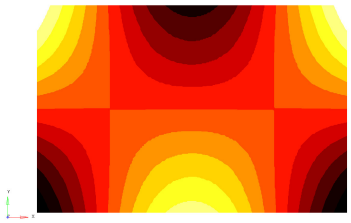

(3) 774.6Hz

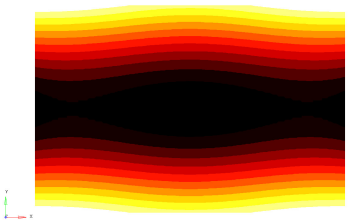

(4) 837.3Hz

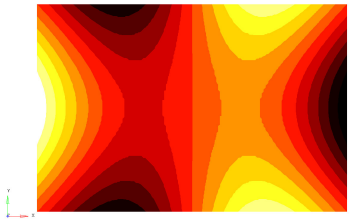

(5) 967Hz

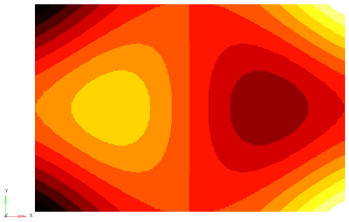

(6) 1123Hz

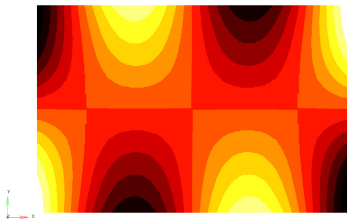

(7) 1435Hz

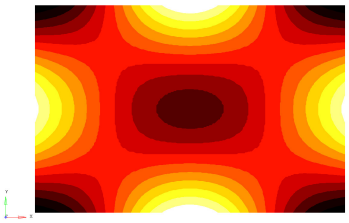

(8) 1650Hz

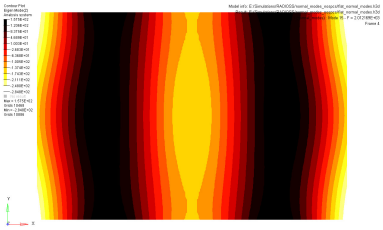

(9) 2012Hz

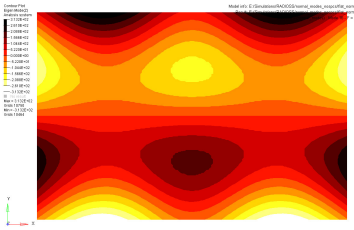

(10) 2263Hz

Figure C.1: The first 10 real eigenmodes of the small (120x80 mm) Hastelloy-X plate from simulation.

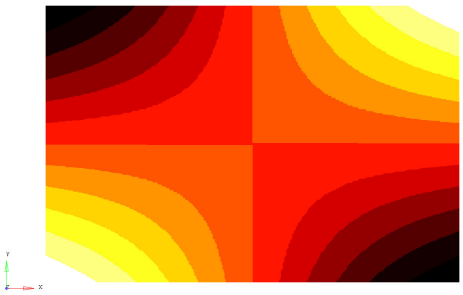

(1) 101Hz

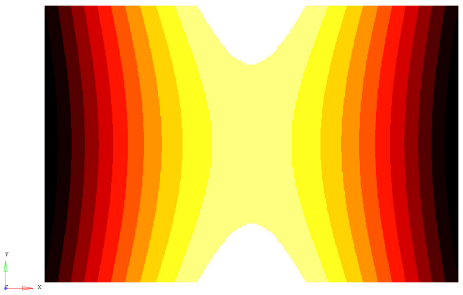

(2) 107.9Hz

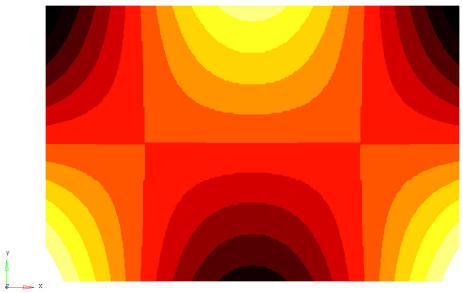

(3) 233Hz

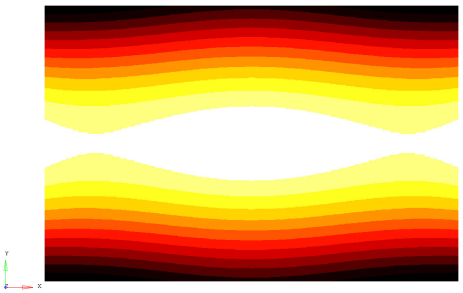

(4) 251.4Hz

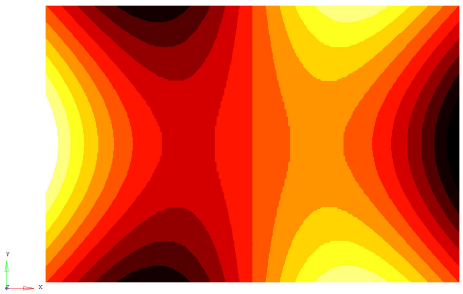

(5) 290.6Hz

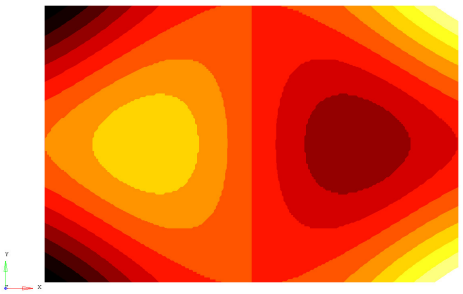

(6) 337.4Hz

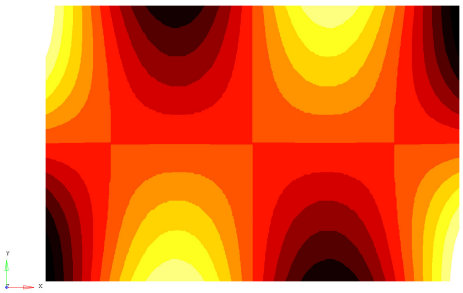

(7) 431.8Hz

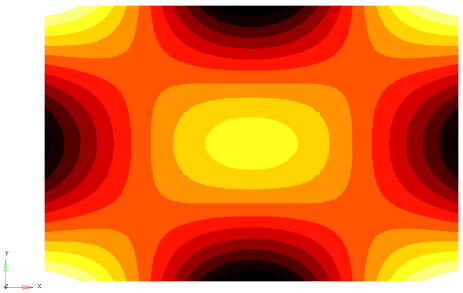

(8) 496.8Hz

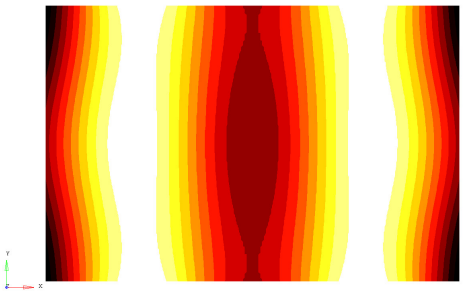

(9) 604.6Hz

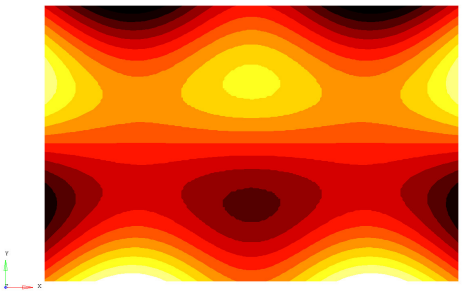

(10) 680.2Hz

Figure C.2: The first 10 real eigenmodes of the large (219x146 mm) Hastelloy-X plate from simulation.

Appendix D

PL-DIC Random Capture

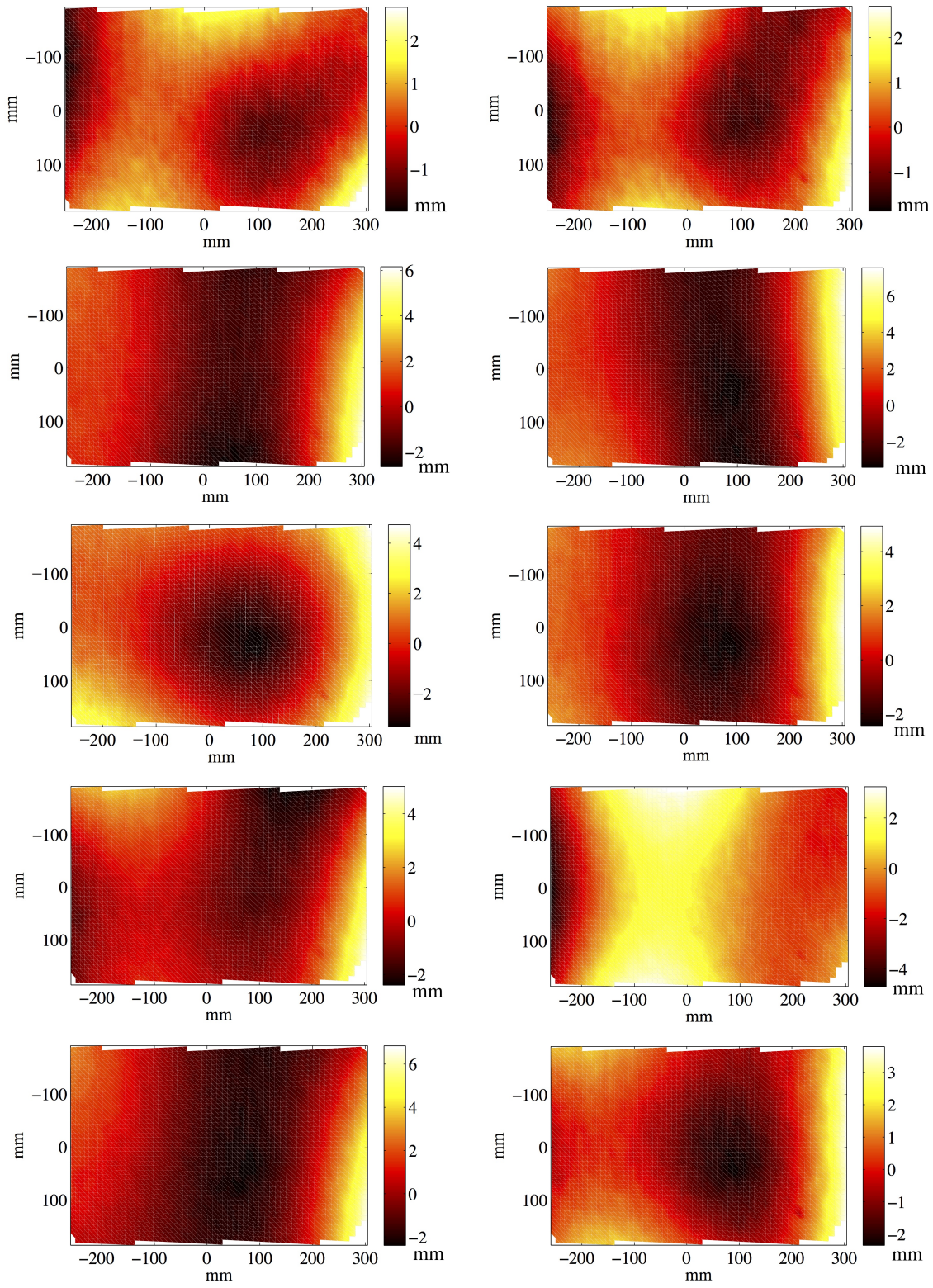

Figure D.1: The full set of the first series of out-of-plane displacement captured using PL-DIC with random excitation.

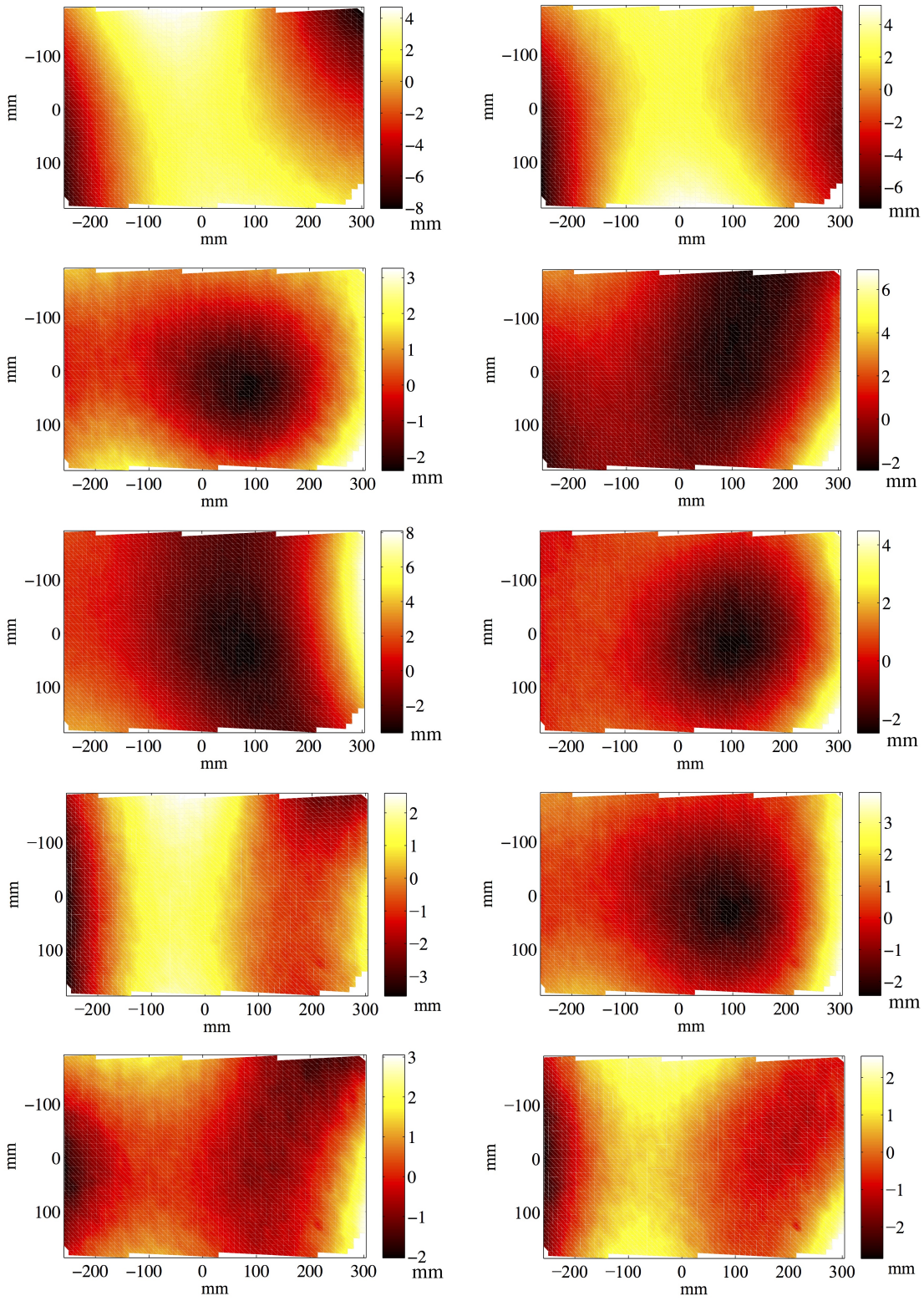

Figure D.2: The full set of the second series of out-of-plane displacement captured using PL-DIC with random excitation.

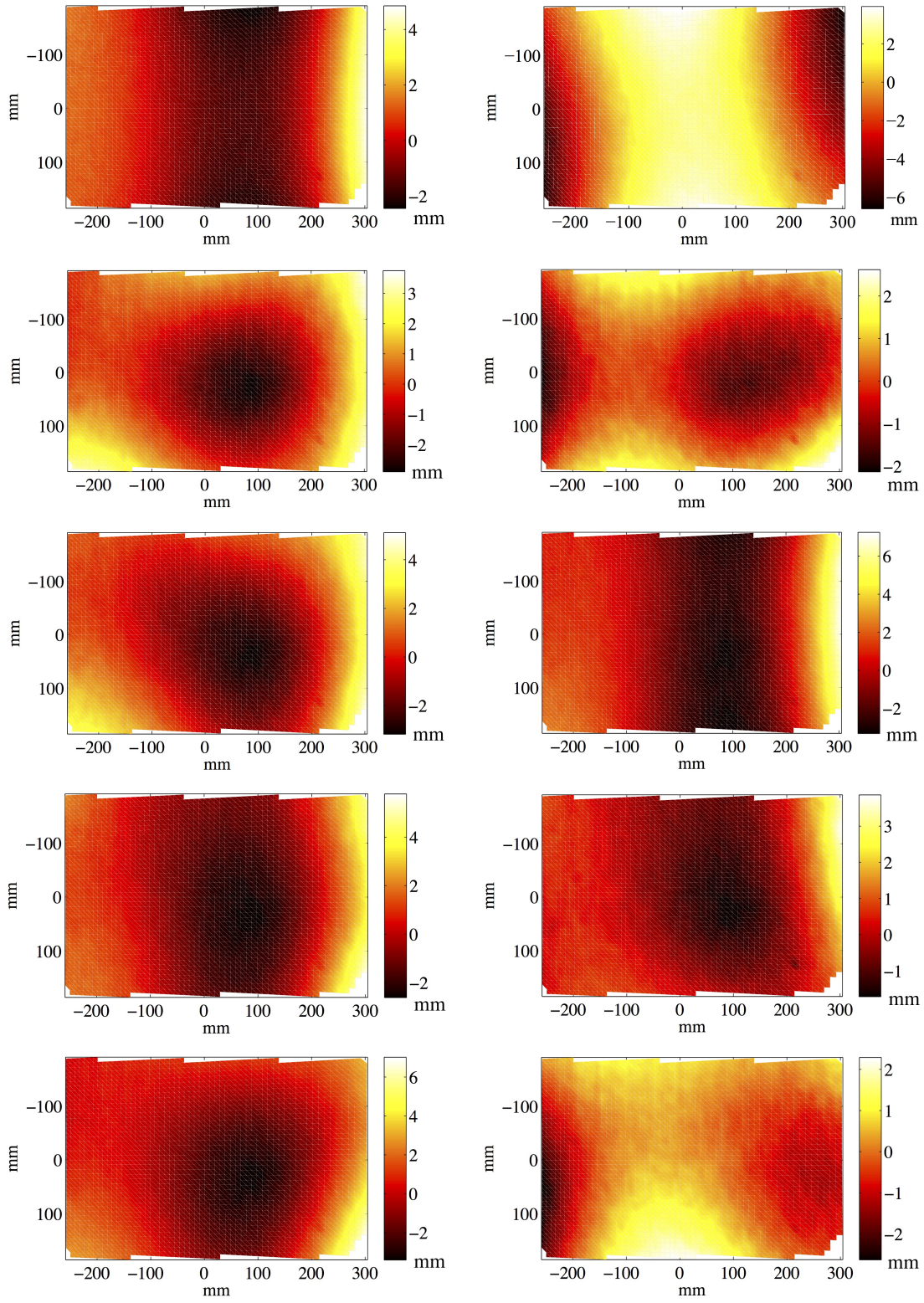

Figure D.3: The full set of the third series of out-of-plane displacement captured using PL-DIC with random excitation.

REFERENCES

REFERENCES

[1] L. Schwer, H. Mair, and R. Crane, "Guide for verification and validation in computational solid mechanics," *American Society of Mechanical Engineers, ASME V&V*, vol. 10, 2006.

[2] R. Shimovetz and K. Wentz, "High intensity acoustic testing of flight structures," in *Instrumentation in Aerospace Simulation Facilities, 1995. ICIASF'95 Record., International Congress on*, pp. 50–1, IEEE, 1995.

[3] R. Blevins, I. Holehouse, and K. Wentz, "Thermoacoustic loads and fatigue of hypersonic vehicle skin panels," *Journal of Aircraft*, vol. 30, no. 6, pp. 971–978, 1993.

[4] T. Beberniss, M. Spottswood, and T. Eason, "High-speed digital image correlation measurements of random nonlinear dynamic response," *Experimental and Applied Mechanics*, vol. 6, pp. 171–186, 2011.

[5] P. Cunningham and R. White, "Dynamic response of doubly curved honeycomb sandwich panels to random acoustic excitation. Part 1: Experimental study," *Journal of Sound and Vibration*, vol. 264, no. 3, pp. 579–603, 2003.

[6] A. Steinwolf, R. White, and H. Wolfe, "Simulation of jet-noise excitation in an acoustic progressive wave tube facility," *The Journal of the Acoustical Society of America*, vol. 109, p. 1043, 2001.

[7] S. Abotula, N. Heeder, R. Chona, and A. Shukla, "Dynamic thermo-mechanical response of Hastelloy-X to shock wave loading," *Experimental Mechanics*, vol. 54, no. 2, pp. 279–291, 2014.

[8] J. Leatherwood, S. Clevenson, C. Powell, and E. Daniels, "Acoustic testing of high temperature panels," in *AIAA, Space Programs and Technologies Conference*, vol. 1, 1990.

[9] B. Clarkson, "Stresses in skin panels subjected to random acoustic loading," Tech. Rep. AFML-TR-67-199, DTIC Document, June 1967.

[10] C. Schneider, "Acoustic fatigue of aircraft structures at elevated temperatures," Tech. Rep. AFFDL-TR-73-155, DTIC Document, March 1974.

[11] R. Blevins, D. Bofilios, I. Holehouse, V. Hwa, M. Tratt, A. Laganelli, P. Pozefsky, and M. Pierucci, "Thermo-vibro-acoustic loads and fatigue of hypersonic flight ve-

hicle structure," Tech. Rep. AFRL-RB-WP-TR-2009-3139, DTIC Document, June 2009.

[12] M. Gruber and A. Nejad, "Development of a large-scale supersonic combustion research facility," in 32^{nd} *AIAA, Aerospace Sciences Meeting and Exhibit, Reno, NV*, 1994.

[13] R. White, "Developments in the acoustic fatigue design process for composite aircraft structures," *Composite Structures*, vol. 16, no. 1-3, pp. 171–192, 1990.

[14] R. White, "A comparison of some statistical properties of the responses of aluminium alloy and CFRP plates to acoustic excitation," *Composites*, vol. 9, no. 4, pp. 251–258, 1978.

[15] C. Ng and R. White, "Dynamic behaviour of postbuckled isotropic plates under in-plane compression," *Journal of Sound and Vibration*, vol. 120, no. 1, pp. 1–18, 1988.

[16] C. Ng, "Nonlinear and snap-through responses of curved panels to intense acoustic excitation," *Journal of Aircraft*, vol. 26, pp. 281–288, 1989.

[17] P. Cunningham and R. White, "A review of analytical methods for aircraft structures subjected to high-intensity random acoustic loads," *Proceedings of the Institution of Mechanical Engineers, Part G: Journal of Aerospace Engineering*, vol. 218, no. 3, pp. 231–242, 2004.

[18] P. Cunningham, R. White, and G. Aglietti, "The effects of various design parameters on the free vibration of doubly curved composite sandwich panels," *Journal of Sound and Vibration*, vol. 230, no. 3, pp. 617–648, 2000.

[19] G. Cloud, *Springer handbook of experimental solid mechanics*, ch. 18. Basics of optics, pp. 447–478. Springer Science & Business Media, 2008.

[20] Y. Gan and W. Steinchen, *Springer handbook of experimental solid mechanics*, ch. 23. Speckle methods, pp. 655–673. Springer Science & Business Media, 2008.

[21] J. Leendertz and J. Butters, "An image-shearing speckle-pattern interferometer for measuring bending moments," *Journal of Physics E: Scientific Instruments*, vol. 6, no. 11, p. 1107, 1973.

[22] Y. Hung, R. Rowlands, and I. Daniel, "Speckle-shearing interferometric technique: A full-field strain gauge," *Applied Optics*, vol. 14, no. 3, pp. 618–622, 1975.

[23] J.-L. Piro and M. Grédiac, "Producing and transferring low-spatial-frequency grids for measuring displacement fields with moiré and grid methods," *Experimental Techniques*, vol. 28, no. 4, pp. 23–26, 2004.

[24] F. Pierron, B. Green, and M. R. Wisnom, "Full-field assessment of the damage process of laminated composite open-hole tensile specimens. Part I: Methodology," *Composites Part A: Applied Science and Manufacturing*, vol. 38, no. 11, pp. 2307–2320, 2007.

[25] C. Badulescu, M. Grédiac, and J. Mathias, "Investigation of the grid method for accurate in-plane strain measurement," *Measurement Science and Technology*, vol. 20, no. 9, p. 095102, 2009.

[26] S. Ri, M. Fujigaki, and Y. Morimoto, "Sampling moiré method for accurate small deformation distribution measurement," *Experimental Mechanics*, vol. 50, no. 4, pp. 501–508, 2010.

[27] Y. Surrel, N. Fournier, M. Grédiac, and P.-A. Paris, "Phase-stepped deflectometry applied to shape measurement of bent plates," *Experimental Mechanics*, vol. 39, no. 1, pp. 66–70, 1999.

[28] M. Grédiac, N. Fournier, P.-A. Paris, and Y. Surrel, "Direct identification of elastic constants of anisotropic plates by modal analysis: Experimental results," *Journal of Sound and Vibration*, vol. 210, no. 5, pp. 643–659, 1998.

[29] C. Devivier, F. Pierron, and M. Wisnom, "Impact damage detection in composite plates using deflectometry and the Virtual Fields Method," *Composites Part A: Applied Science and Manufacturing*, vol. 48, pp. 201–218, 2013.

[30] A. Moreau, D. Borza, and I. Nistea, "Full-field vibration measurement by time-average speckle interferometry and by Doppler vibrometry – A comparison," *Strain*, vol. 44, no. 5, pp. 386–397, 2008.

[31] T. Schmidt, J. Tyson, and K. Galanulis, "Full-field dynamic displacement and strain measurement-specific examples using advanceded 3d image correlation," *Experimental Techniques*, vol. 27, no. 4, pp. 22–26, 2003.

[32] S. Vanlanduit, J. Vanherzeele, R. Longo, and P. Guillaume, "A digital image correlation method for fatigue test experiments," *Optics and Lasers in Engineering*, vol. 47, no. 3-4, pp. 371–378, 2009.

[33] L. Chen, Y. Huang, X. Nguyen, J. Chen, and C. Chang, "Dynamic out-of-plane profilometry for nano-scale full-field characterization of MEMS using stroboscopic interferometry with novel signal deconvolution algorithm," *Optics and Lasers in Engineering*, vol. 47, no. 2, pp. 237–251, 2009.

[34] E. A. Patterson, P. Brailly, and M. Taroni, "High frequency quantitative photoelasticity applied to jet engine components," *Experimental Mechanics*, vol. 46, pp. 661–668, 2006.

[35] R. Greene, A. Clarke, S. Turner, and E. Patterson, "Some applications of combined thermoelastic-photoelastic stress analysis," *The Journal of Strain Analysis for Engineering Design*, vol. 42, no. 3, p. 173, 2007.

[36] C. Han and Y. Chao, "Photoelastic modulated imaging ellipsometry by stroboscopic illumination technique," *Review of Scientific Instruments*, vol. 77, no. 2, pp. 023107–023107, 2006.

[37] G. Moneron, A. Boccara, and A. Dubois, "Stroboscopic ultrahigh-resolution full-field optical coherence tomography," *Optics letters*, vol. 30, no. 11, pp. 1351–1353, 2005.

[38] G. Pedrini, B. Pfister, and H. Tiziani, "Double pulse-electronic speckle interferometry," *Journal of Modern Optics*, vol. 40, no. 1, pp. 89–96, 1993.

[39] G. Pedrini and H. J. Tiziani, "Double-pulse electronic speckle interferometry for vibration analysis," *Applied Optics*, vol. 33, no. 34, pp. 7857–7863, 1994.

[40] Z. Wang, T. Walz, and A. Ettemeyer, "3D-PulsESPI technique for measurement of dynamic structure response," in *XVIII Conference & Exhibition on Structural Dynamics, San Antonio*, 2000.

[41] M. Poncelet, G. Barbier, B. Raka, S. Courtin, R. Desmorat, J. Le-Roux, and L. Vincent, "Biaxial high cycle fatigue of a type 304L stainless steel: Cyclic strains and crack initiation detection by digital image correlation," *European Journal of Mechanics-A/Solids*, vol. 29, no. 5, pp. 810–825, 2010.

[42] T. Schmidt, J. Tyson, and K. Galanulis, "Full-field dynamic displacement and strain measurement using advanced 3D image correlation photogrammetry: Part 1," *Experimental Techniques*, vol. 27, no. 3, pp. 47–50, 2003.

[43] F. Pierron, R. Cheriguene, P. Forquin, R. Moulart, M. Rossi, and M. Sutton, "Performances and limitations of three ultra high-speed imaging cameras for full-field deformation measurements," *Applied Mechanics and Materials*, vol. 70, pp. 81–86, 2011.

[44] P. Reu, "High/ultra-high speed imaging as a diagnostic tool," *Applied Mechanics and Materials*, vol. 70, pp. 69–74, 2011.

[45] AIAA, "Guide for the verification and validation of computational fluid dynamics and simulations," Tech. Rep. G-077-1998, American Institute of Aeronautics and Astronautics, Reston, VA, 1998.

[46] DoD, "Modeling and simulation verification, validation, and accreditation," Tech. Rep. DODI 5000.61, Department of Defense, 2009.

[47] W. L. Oberkampf, T. G. Trucano, and C. Hirsch, "Verification, validation, and predictive capability in computational engineering and physics," *Applied Mechanics Reviews*, vol. 57, no. 5, pp. 345–384, 2004.

[48] L. Schwer, "An overview of the PTC 60/V&V 10: Guide for verification and validation in computational solid mechanics," *Engineering with Computers*, vol. 23, no. 4, pp. 245–252, 2007.

[49] M. Greenwald, "Verification and validation for magnetic fusion," *Physics of Plasmas*, vol. 17, p. 058101, 2010.

[50] K. Solanki, M. Horstemeyer, W. Steele, Y. Hammi, and J. Jordon, "Calibration, validation, and verification including uncertainty of a physically motivated internal state variable plasticity and damage model," *International Journal of Solids and Structures*, vol. 47, no. 2, pp. 186–203, 2010.

[51] L. Schwer, "Validation metrics for response histories: Perspectives and case studies," *Engineering with Computers*, vol. 23, no. 4, pp. 295–309, 2007.

[52] C. Sebastian, E. Hack, and E. Patterson, "An approach to the validation of computational solid mechanics models for strain analysis," *The Journal of Strain Analysis for Engineering Design*, vol. 48, no. 1, pp. 36–47, 2013.

[53] C. M. Sebastian, "A method for the validation of computational models using digital image correlation and image decomposition," Master's thesis, Michigan State University, 2011.

[54] M. Teague, "Image analysis via the general theory of moments," *JOSA*, vol. 70, no. 8, pp. 920–930, 1980.

[55] R. Mukundan, S. Ong, and P. Lee, "Image analysis by Tchebichef moments," *IEEE Transactions on Image Processing*, vol. 10, no. 9, pp. 1357–1364, 2002.

[56] W. Wang and J. E. Mottershead, "Adaptive moment descriptors for full-field strain and displacement measurements," *The Journal of Strain Analysis for Engineering Design*, vol. 48, no. 1, pp. 16–35, 2013.

[57] P.-T. Yap, R. Paramesran, and S.-H. Ong, "Image analysis by Krawtchouk moments," *IEEE Transactions on Image Processing*, vol. 12, no. 11, pp. 1367–1377, 2003.

[58] W. Wang, J. E. Mottershead, C. M. Sebastian, and E. A. Patterson, "Shape features and finite element model updating from full-field strain data," *International Journal of Solids and Structures*, vol. 48, no. 11, pp. 1644–1657, 2011.

[59] W. Wang, J. E. Mottershead, A. Ihle, T. Siebert, and H. Reinhard Schubach, "Finite element model updating from full-field vibration measurement using digital image correlation," *Journal of Sound and Vibration*, vol. 330, no. 8, pp. 1599–1620, 2011.

[60] W. Wang, J. E. Mottershead, T. Siebert, and A. Pipino, "Frequency response functions of shape features from full-field vibration measurements using digital image correlation," *Mechanical Systems and Signal Processing*, vol. 28, pp. 333–347, 2012.

[61] R. L. Burguete, G. Lampeas, J. E. Mottershead, E. A. Patterson, A. Pipino, T. Siebert, and W. Wang, "Analysis of displacement fields from a high-speed impact using shape descriptors," *The Journal of Strain Analysis for Engineering Design*, 2013.

[62] C. M. Sebastian, E. A. Patterson, and D. Ostberg, "Comparison of numerical and experimental strain measurements of a composite panel using image decomposition," *Applied Mechanics and Materials*, vol. 70, pp. 63–68, 2011.

[63] R. Allemang, M. Spottswood, and T. Eason, "A principal component analysis (PCA) decomposition based validation metric for use with full field measurement situations," in *Model Validation and Uncertainty Quantification*, vol. 3, pp. 249–263, Springer, 2014.

[64] BIPM, "International vocabulary of metrology–Basic and general concepts and associated terms (VIM)," *Joint Committee for Guides in Metrology*, vol. 200: 2008.

[65] B. Pan, K. Qian, H. Xie, and A. Asundi, "Two-dimensional digital image correlation for in-plane displacement and strain measurement: A review," *Measurement Science and Technology*, vol. 20, no. 6, p. 062001, 2009.

[66] H. Haddadi and S. Belhabib, "Use of rigid-body motion for the investigation and estimation of the measurement errors related to digital image correlation technique," *Optics and Lasers in Engineering*, vol. 46, no. 2, pp. 185–196, 2008.

[67] M. Bornert, F. Brémand, P. Doumalin, J.-C. Dupré, M. Fazzini, M. Grédiac, F. Hild, S. Mistou, J. Molimard, J.-J. Orteu, L. Robert, Y. Surrel, P. Vacher,

and B. Wattrisse, "Assessment of digital image correlation measurement errors: Methodology and results," *Experimental Mechanics*, vol. 49, pp. 353–370, 2009.

[68] M. Fazzini, S. Mistou, O. Dalverny, and L. Robert, "Study of image characteristics on digital image correlation error assessment," *Optics and Lasers in Engineering*, vol. 48, no. 3, pp. 335–339, 2010.

[69] P. Lava, S. Cooreman, S. Coppieters, M. De Strycker, and D. Debruyne, "Assessment of measuring errors in DIC using deformation fields generated by plastic FEA," *Optics and Lasers in Engineering*, vol. 47, no. 7, pp. 747–753, 2009.

[70] P. Lava, S. Cooreman, and D. Debruyne, "Study of systematic errors in strain fields obtained via DIC using heterogeneous deformation generated by plastic FEA," *Optics and Lasers in Engineering*, vol. 48, no. 4, pp. 457–468, 2010.

[71] Y. Wang, P. Lava, S. Coppieters, M. De Strycker, P. Van Houtte, and D. Debruyne, "Investigation of the uncertainty of DIC under heterogeneous strain states with numerical tests," *Strain*, vol. 48, no. 6, pp. 453–462, 2012.

[72] T. Becker, K. Splitthof, T. Siebert, and P. Kletting, "Error estimations of 3D digital image correlation measurements," Tech. Rep. T-Q-400-Accuracy-3DCORR-003-EN, Dantec Dynamics GmbH, Ulm, Germany, 2006.

[73] T. Siebert, T. Becker, K. Spiltthof, I. Neumann, and R. Krupka, "High-speed digital image correlation: Error estimations and applications," *Optical Engineering*, vol. 46, no. 5, pp. 051004–051004, 2007.

[74] M. Sutton, J. Yan, V. Tiwari, H. Schreier, and J. Orteu, "The effect of out-of-plane motion on 2D and 3D digital image correlation measurements," *Optics and Lasers in Engineering*, vol. 46, no. 10, pp. 746–757, 2008.

[75] P. Lava, S. Coppieters, Y. Wang, P. Van Houtte, and D. Debruyne, "Error estimation in measuring strain fields with DIC on planar sheet metal specimens with a non-perpendicular camera alignment," *Optics and Lasers in Engineering*, vol. 49, no. 1, pp. 57–65, 2011.

[76] P. Reu, "A study of the influence of calibration uncertainty on the global uncertainty for digital image correlation using a Monte Carlo approach," *Experimental Mechanics*, vol. 53, no. 9, pp. 1661–1680, 2013.

[77] E. Zappa, P. Mazzoleni, and A. Matinmanesh, "Uncertainty assessment of digital image correlation method in dynamic applications," *Optics and Lasers in Engineering*, vol. 56, pp. 140–151, 2014.

[78] E. A. Patterson, E. Hack, P. Brailly, R. L. Burguete, Q. Saleem, T. Siebert, R. A. Tomlinson, and M. P. Whelan, "Calibration and evaluation of optical systems for full-field strain measurement," *Optics and Lasers in Engineering*, vol. 45, pp. 550–564, 2007.

[79] M. P. Whelan, D. Albrecht, E. Hack, and E. A. Patterson, "Calibration of a speckle interferometery full-field strain measurement system," *Strain*, vol. 44, pp. 180–190, 2008.

[80] C. Sebastian and E. Patterson, "Calibration of a digital image correlation system," *Experimental Techniques*, 2012.

[81] X. Tan, Y. Kang, and E. Patterson, "Calibration of a 3-D digital image correlation system for large deformation contact problems," in *Journal of Physics: Conference Series*, vol. 382, p. 012035, IOP Publishing, 2012.

[82] J. L. Turner and S. S. Russell, "Application of digital image analysis to strain measurement at elevated temperature," *Strain*, vol. 26, no. 2, pp. 55–59, 1990.

[83] J. Lyons, J. Liu, and M. Sutton, "High-temperature deformation measurements using digital-image correlation," *Experimental Mechanics*, vol. 36, no. 1, pp. 64–70, 1996.

[84] B. Grant, H. Stone, P. Withers, and M. Preuss, "High-temperature strain field measurement using digital image correlation," *The Journal of Strain Analysis for Engineering Design*, vol. 44, no. 4, pp. 263–271, 2009.

[85] B. Pan, D. Wu, Z. Wang, and Y. Xia, "High-temperature digital image correlation method for full-field deformation measurement at 1200 °C," *Measurement Science and Technology*, vol. 22, no. 1, p. 015701, 2011.

[86] X. Chen, N. Xu, L. Yang, and D. Xiang, "High temperature displacement and strain measurement using a monochromatic light illuminated stereo digital image correlation system," *Measurement Science and Technology*, vol. 23, no. 12, p. 125603, 2012.

[87] B. Pan, D. Wu, and J. Gao, "High-temperature strain measurement using active imaging digital image correlation and infrared radiation heating," *The Journal of Strain Analysis for Engineering Design*, 2013.

[88] R. B. Berke and J. Lambros, "Ultraviolet digital image correlation (UV-DIC) for high temperature applications," *Review of Scientific Instruments*, vol. 85, no. 4, p. 045121, 2014.

[89] J. Hammer, J. Seidt, and A. Gilat, "Strain measurement at temperatures up to 800 °C utilizing digital image correlation," in *Advancement of Optical Methods in Experimental Mechanics*, vol. 3, pp. 167–170, Springer, 2014.

[90] X. Guo, J. Liang, Z. Tang, B. Cao, and M. Yu, "High-temperature digital image correlation method for full-field deformation measurement captured with filters at 2600 °C using spraying to form speckle patterns," *Optical Engineering*, vol. 53, no. 6, pp. 063101–063101, 2014.

[91] M. A. Sutton, "Digital image correlation for shape and deformation measurements," in *Springer handbook of experimental solid mechanics*, pp. 565–600, Springer, 2008.

[92] J. W. Dally and W. F. Riley, *Experimental stress analysis*. College House Enterprises, LLC, 4th ed., 2005.

[93] T. Siebert, T. Becker, K. Spiltthof, I. Neumann, and R. Krupka, "Error estimations in digital image correlation technique," *Applied Mechanics and Materials*, vol. 7, pp. 265–270, 2007.

[94] P. Reu, "Speckles and their relationship to the digital camera," *Experimental Techniques*, vol. 38, pp. 1–2, 2014.

[95] P. Reu, "All about speckles: Aliasing," *Experimental Techniques*, vol. 38, pp. 1–3, 2014.

[96] P. Reu, "All about speckles: Speckle size measurement," *Experimental Techniques*, vol. 38, pp. 1–2, 2014.

[97] P. Reu, "All about speckles: Contrast," *Experimental Techniques*, vol. 39, pp. 1–2, 2015.

[98] Macneal-Schwendler Co, *MSC/NASTRAN dynamic analysis users guide*, 2012.

[99] A. Davighi, R. L. Burguete, M. Feligiotti, E. Hack, S. James, E. A. Patterson, T. Siebert, and M. P. Whelan, "The development of a reference material for calibration of full-field optical measurement systems for dynamic deformation measurements," *Applied Mechanics and Materials*, vol. 70, pp. 33–38, 2011.

[100] B. N. Taylor and C. E. Kuyatt, "NIST Technical Note," *Guidelines for evaluating and expressing the uncertainty of NIST measurement results*, no. 1297, p. 24, 1994.

[101] R. D. Blevins, *Formulas for natural frequency and mode shape*. Van Nostrand Reinhold, 1979.

[102] M. Sutton, J. Orteu, and H. Schreier, *Image correlation for shape, motion and deformation measurements: Basic concepts, theory and applications*. Springer Verlag, 2009.

[103] BIPM, "Guide to the expression of uncertainty in measurement (GUM)," *Joint Committee for Guides in Metrology*, vol. 100:2008.

[104] L. I.-K. Lin, "A concordance correlation coefficient to evaluate reproducibility," *Biometrics*, pp. 255–268, 1989.

[105] D. Mead, "Vibration and buckling of flat free–free plates under non-uniform in-plane thermal stresses," *Journal of Sound and Vibration*, vol. 260, no. 1, pp. 141–165, 2003.

[106] C. Bailey, "Vibration and local instability of thermally stressed plates," *Computer Methods in Applied Mechanics and Engineering*, vol. 25, no. 3, pp. 263–278, 1981.

[107] K. Murphy, L. Virgin, and S. Rizzi, "Characterizing the dynamic response of a thermally loaded, acoustically excited plate," *Journal of Sound and vibration*, vol. 196, no. 5, pp. 635–658, 1996.

[108] H. Chen and L. N. Virgin, "Dynamic analysis of modal shifting and mode jumping in thermally buckled plates," *Journal of Sound and Vibration*, vol. 278, no. 1, pp. 233–256, 2004.

[109] B. Jeon, H. Kang, and Y. Lee, "Free vibration characteristics of rectangular plate under rapid thermal loading," in *The* 9^{th} *International Congress on Thermal Stresses, Budapest*, 2011.

[110] S. Zinn and S. L. Semiatin, *Elements of induction heating: Design, control, and applications*. ASM International, 1988.

[111] J. Lesniak and B. Bartel, "An elevated-temperature TSA furnace design," *Experimental Techniques*, vol. 20, no. 2, pp. 10–13, 1996.

Nomenclature

AFRL Air Force Research Laboratory

CCD Charge-Coupled Device

CEAC Combined Environment Acoustic Chamber

CMOS Complimentary Metal-Oxide-Semiconductor

DARPA Defense Advanced Research Projects Agency

DIC Digital Image Correlation

FFT Fast Fourier Transform

FWHM Full-Width at Half Maximum

IR Infrared

LED Light Emitting Diode

NASA National Aeronautics and Space Administration

NASP National Aero-Space Plane

Nd:YAG Neodymium-doped Yttrium Aluminium Garnet

PL-DIC Pulsed Laser Digital Image Correlation

PSD Power Spectral Density

PWT Progressive Wave Tube

SEF Sub-Element Facility

SSC Structural Sciences Center

TSA Thermoelastic Stress Analysis

TTL Transistor-Transistor Logic

UIUC University of Illinois at Urbana-Champaign

USAF United States Air Force

UV Ultra-Violet